Determination of Heterogeneity by High-Resolution Seismic Reservoir Characterization in the Heavy Oil Temblor Reservoir of Coalinga Field, California

Sailendra Nath Mahapatra

Dissertation submitted to the Faculty of the
Virginia Polytechnic Institute and State University
in partial fulfillment of the requirements for the degree of

Doctor of Philosophy
in
Geosciences

Dr. Matthias G. Imhof, Chair
Dr. James Castle, Clemson University
Dr. Martin Chapman, VPI & SU
Dr. Ken Eriksson, VPI & SU

August 12, 2005
Blacksburg, Virginia
USA

Keywords: Steam-affected merged 3D poststack seismic, San Joaquin basin and San Andreas Transforms, Seismostratigraphic and Seismogeomorphic analysis, Seismic attribute and geovolume visualization interpretation, Stacked high-gamma coarsening upward sands, Monarch sands of Monterey Formation

Determination of Heterogeneity by High-Resolution Seismic Reservoir Characterization in the Heavy Oil Temblor Reservoir of Coalinga Field, California

Sailendra N. Mahapatra

(ABSTRACT)

The research focuses on analysis and subsurface imaging of siliciclastics rocks on steam-affected 3D poststack seismic data, merged from different vintages, from the Temblor Formation in the Coalinga heavy oil reservoir in the San Joaquin basin, California. The objective was identification, delineation, and demarcation of reservoir heterogeneities by seismostratigraphic and seismogeomorphic analysis.

The proximity of the San Andreas Transforms greatly controlled basin evolution and caused substantial reservoir heterogeneity by changing the depositional environment from shallow marine to near-shore fluvial. Moreover, two unconformities dissect the reservoir interval.

The seismic dataset exhibits erratic, distorted reflection strengths and amplitudes caused by steam-injection-aided production. A petrophysical analysis based on Gassmann fluid substitution suggests a 27% P-wave velocity decrease in steam-saturated intervals. Seismic to well log ties were problematic and vexing due to the resulting statics, wavelet changes, and line mismatches. Mapping and flattening on a deeper horizon, however, allowed mapping of the internal unconformities and well ties which were crucial for seismostratigraphic sequence identification.

Visualization of seismic attributes brought out stratification patterns and two distinct, laterally and vertically extensive, porous, and interconnected facies tracts interpreted as incised valley fills and tidal-to-subtidal deposits as evidenced by bright, steam related amplitudes.

Seismic attribute analysis, Geobody Visualization and Interpretation, and structure and isochron maps brought out two prominent channel-systems, recut and restacked in the central part of the area. These deposits were identified on seismic data and correlated to high-gamma coarsening-upward sands on logs and cores. The deeper one, shifting towards SSE with depth, lies between the Base Temblor and Buttonbed unconformities both in the southwestern and northwestern parts of the study area and is scattered in the western-central portion. The shallower one originates in southwestern corner below the Top Temblor unconformity shifts towards ESE-SE with depth, and runs nearly parallel to the Top Temblor unconformity. It cuts across the Valv unconformity in central part creating a channel incision, and follows the Buttonbed unconformity towards the north.

The investigation segmented the reservoir into channels, non-channel bearing, and unconformity-bounded subunits which will allow the operator to improve steam injection and optimize placement of oil producing infill wells.

Contents

List of Figures

List of Tables

Dedication

To my wonderful, beloved mother Late Srimati Manorama Mahapatra and father Srijukta Satya Narayan Mahapatra …

… who taught me how to walk, instilled the "can do" attitude in me,
showered their blessings, affection, and constant encouragement …
and for supporting me in the achievement of my every goal …

Acknowledgments

My sincerest appreciation is extended to Matthias Imhof for his valuable guidance and advice. I am thankful to the members of my research advising committee consisting of James Castle, Martin Chapman, and Ken Eriksson for their assistance and valuable comments. Thanks are also due to Cahit Çoruh and Matthew Mikulich for their valuable comments and suggestions.

I would like to thank the Chevron Production Company in Bakersfield, California, for supplying the data sets and allowing me to publish the result of this study. I also thank the Department of Energy for funding this project under contract DE-FC26-00BC15301. I am thankful to Landmark Graphics Corporation for allowing me to use their software modules and for timely support.

My special thanks go to my loving wife Jochhna Rani Mahapatra, our wonderful son Subrat Narayan Mahapatra and daughter Swati Manorama Mahapatra for their love, support, care and putting up with me with the high stress level during the course work and research.

Chapter 1

Introduction

Reservoir characterization and model building are necessary prerequisite steps to develop an oil field (Mahapatra et al., 2003a). Reservoir models are needed to evaluate risks and production scenarios. These models depend on fluid content, composition, and structure of the reservoir. Reservoir characterization is the three-dimensional delineation of a reservoir, its structural framework, volume, heterogeneity, and distributions of rock and fluid properties which allows maximization of production and minimization of costs, for example, by optimizing well locations. Stratigraphic analysis coupled with detection of paleogeomorphic features like paleosol in highstand system tracts (HST), slumps and other mass transport complex features, channel-levee meandering features, etc. play significant roles in reservoir characterization.

Seismic reservoir characterization integrates geologic and seismic data. The resulting reservoir model is based on lithological parameters estimated from well cuttings, core, and wireline logs. Geoscientists utilize the well, seismic, and other relevant data to derive the most realistic model of the reservoir. Between wells, reservoir petrophysics may need to be filled in by use of an appropriate geological model either with interpolation of geologic data or

geostatistics. In either case, the final models of key petrophysical parameters are not perfectly accurate and may differ from the real reservoir. The same set of sparse data may lead to different set of conclusions regarding the depositional processes and / or environment. Take, for example, the case of a braided river system with wells only on the flanks of the system. The conventional seismic interpretation may not help to demarcate the braided feature. From the wells, the most viable interpretation would be conceptualizing a two-channel system, thus excluding the major reservoir facies of the braided system. Even with high-density well data, identification of major sedimentological depositional structures along with any nondepositional features greatly helps the petrophysical delineation of the reservoir. In the absence of a well-defined geological depositional structure, however, the conventional seismic resolution limit of one-fourth of the seismic wavelength (Kallweit, R. S. and Wood, L. C., 1982) may not permit perfect estimation of the reservoir heterogeneities.

With the advanced computing power and portability of workstation software to the desktop, the current state-of-the-art reservoir characterization includes volume visualization and geobody analysis which enable exposure of information normally hidden in the data. This also facilitates creation of new insight into the geophysicst's mind and vision. Interpretation of structural and stratigraphic features of a reservoir using volume visualization and geobody analysis is widely accepted now because of its speed, accuracy, completeness, and efficiency of interpretation.

The objective of the present investigation is to analyze seismic and geologic data of a clastic reservoir to ascertain various seismostratigraphic sequences and geobody elements,

which in turn help to identify, delineate, and demarcate the various reservoir subunits based on their depositional signatures and geological characteristics. Chapter 2 presents a review of regional geology to provide a framework for interpretation and explanation for the observed geological complexities and reservoir heterogeneities. Chapter 3 presents an overview of the Coalinga heavy oil field, the present study area, including production, reservoir characteristics, and architecture details. Chapter 4 describes the present seismic data set analyzed and the effect of steam injection induced production on the data set. Chapter 5 describes the seismostratigraphic analysis to understand the sequence stratigraphy of the reservoir, which helps in defining sequence boundaries and compartmentalization of the reservoir. In Chapter 6, seismic attribute analysis, volume-based visualization and geobody analysis are performed to identify and delineate the seismogeomorphological features which play a major part in compartmentalization of lithofacies in the reservoir. In chapter 7, the characteristics of the high amplitude bodies associated with the identified seismogeomorphologial features are further analyzed to ascertain and demonstrate its petrophysics, geometry, and spatial distribution in the study area which will help in reservoir development and production scenario of the field. Finally, in Chapter 8, the results of the investigation are discussed, summarized, and recommendations on how this investigation may be extended further are emphasized.

Chapter 2

Regional Geology

The first geological observations in the San Joaquin Valley date back to the late 1800's (Shedd, 1932). During the early 1900's, due to the discovery of the oil fields of McKittrick (in 1887), Coalinga (in 1887), and Kern River (in 1901), the geological study of sedimentary rocks in the valley gained momentum, and the knowledge about its geology advanced as the oil exploration activities increased subsequent to these discoveries. The geological research progressed greatly after World War II due to increasing demand for crude oil and free exchange of scientific knowledge across the world (Bartow, 1991).

Hoots et al. (1954) published the first generalized review of the Cenozoic history of the valley, which was further updated stratigraphically by Repenning (1960) and Hackel (1966). Based on analysis of benthic foraminiferal faunas from marine Tertiary rocks from the southern part of the valley, Bandy and Arnal (1969) attempted to quantify the basin subsidence and uplift. Further research on these Tertiary marine sequences brought out an apparent synchronicity of depositional cycles on the eastern and western halfs of the valley although both east and west sides show different types of depositional sequences and facies (Foss, 1972). In the last three decades, the focus of research has been directed towards the

tectonic mechanisms which control various aspects of the basin evolution (Nilsen and Clarke, 1975). Harding (1976) analyzed and linked the structural evolution of the westside folded complex to different phases of the growth of the San Andreas Fault. Other researchers linked the origin of the San Joaquin basin to plate tectonic processes (Blake et al., 1978; Dickinson and Snyder, 1979; and Howell et al., 1980). Recent advances in sequence stratigraphy and global tectonics in the light of plate tectonics play a major role in the continuing revision of the regional stratigraphy. The research and developments based on these concepts have greatly advanced the understanding and identification of the timing of depositional events from widely separated and non-unique lithogroups of the San Joaquin basin (Bartow, 1991).

2.1 Geological Setting

The San Joaquin basin is a forearc basin of complex tectonics due to regional extension caused by strike-slip motion of the San Andreas Fault (Bridges and Castle, 2003). It is located in the southern part of the 700 km long Great Valley of California. It is an asymmetric structural trough with a broad, gently inclined eastern flank and a relatively narrow western flank, the later becoming a steep homocline in the northern part of the valley (Figures 1 and 2). In the southern part, it turns into a belt of folds and faults. The basin trough contains Upper Mesozoic to Cenozoic sediments that reach over 9 km thickness in the west-central part of the valley and at the southern end (Bartow, 1991). Bartow (1991) believes that the basin was a fore-arc basin, which was mostly open to the Pacific Ocean on the west during Late Mesozoic and early Cenozoic periods. The basin was converted into a transform-margin basin

during the Late Cenozoic. The sediments were deposited on a westward tilted basement of Sierra Nevada plutonic, mafic, ultramafic, and metamorphic rocks of Jurassic age (Cady, 1975; Page, 1981). Bailey et al. (1964) proposed that towards the west of the valley, both Mesozoic and Early Tertiary Great Valley sequences along with the underlying ophiolite sequences are juxtaposed with the Franciscan Complex along a the Coast Range thrust (Figure 3).

The San Joaquin basin is separated from the Sacramento basin to the north by the buried Stockton arch and Stockton fault (Figure 3). To the south, the basin is separated from the Maricopa-Tejon subbasin by the buried Bakersfield arch. Bartow (1991) observed that the Cenozoic strata in the San Joaquin basin thicken southeastwards from about 800 m in the north (western part of the Stockton arch) to over 9,000 m in the south (in the Maricopa-Tejon subbasin in the south). He also observed that the Mesozoic and Early Tertiary Great Valley sequence thins southeastward and is absent at the Bakersfield arch. Both arches had no appreciable structural relief but could contribute to this huge sedimentation during the Cenozoic period due to basin tilting phenomena associated with regional thrusting and plate kinematics. The Tertiary depocenters of these basins coincide with the Pleistocene and Holocene depocenters (Buena Vista and Kern Lakes basins to the south and the Tulare Lake basin in the central part; Bartow, 1991).

The San Joaquin Valley is on the southern side of the Great Valley and falls in the western Cordillera of North America. Although it shows discrete geomorphic and structural styles similar to that of the western Cordillera, its geology is inherently variable in

stratigraphy and structural styles of deformation due to various Cenozoic intermittent uplifts and subsidence associated with the evolution of the Valley (Bartow, 1991). The Neogene sediments mostly consist of a thick marine section in the southern part and a thin non-marine section in the northern part of the basin. In addition, from a structural point of view, there exists a complex folded system in the western side of the basin, while the eastern side is less deformed due to differential tectonic process which caused a north-south tilting and a western uplift of the valley.

The basin is of great economic importance due to numerous oil fields (Figure 1). Peters et al. (1994) have even reported oil seepages. A generalized stratigraphic column for the basin shows the stratigraphic position of source rocks and oil field/oil stain distribution (Figure 4). Oil, seeps, and stains are mostly concentrated between Eocene to Middle Miocene Formations with sporadic occurrences in Upper Cretaceous (Oil City) and between Mio-Pliocene to Pleistocene (Cymric oil field, Tulley and Cattle oil stain). Peter et al. (1994) observed that the source rocks were from Cretaceous, Eocene, and Miocene periods. They established that due to geological complexities experienced by the basin, there are wide variations in the organic content of the source rocks and mixed oil quality over the entire basin. The oil from the northern part may be tied to the Eocene Kreyenhagen shales. On the eastern side of the San Andreas Fault, the oil stain might have been generated by the relatively unmature Miocene McDonald shale (the equivalent of the Monterey Formation). On the western side of the San Andreas Fault, the Soda Lake Shale of the Vaqueros Formation might have been the source rock. Peters et al. (1994) suspected that the Moreno Formation might have provided the source rock for the Oil City oil seep.

A brief overview of the regional geological complexities of the San Joaquin Valley, the tectonics, and various controls on sedimentation is presented below to illustrate the tectonic and depositional complexities of the basin.

2.2 Tectonics and Major Controls of Sedimentation

The San Joaquin Valley consists of five different tectonic blocks (Figure 3, Bartow, 1991). These are:

1) Northern Sierran Block (NSB),
2) Southern Sierran Block (SSB),
3) Northern Diablo Homocline (NDH),
4) West-side Fold Belt (WFB), and
5) Combined Maricopa-Tejon subbasin and South-margin deformed belt (M-TS).

The NSB, located between the Stockton fault and the San Joaquin River, lies on the east limb of the valley syncline (Figure 3). It is the least deformed block of the valley with a southwest tilt of 1-2^0 and minor Late Cenozoic normal faults.

The SSB, located between the San Joaquin River and the Bakersfield arch (Figure 3) is similar to the NSB in terms of structural style. However, it is more deformed than the NSB with a southwesterly tilt of 4-6^0 and shows Miocene/Pre-Miocene normal faults heading north to northwest with throws up to 600m.

The NDH, located between the Stockton arch and Panoche Creek, lies on the western limb of the valley and shows locally faulted homoclines with northeast dips. It includes the northeast flank of the northern Diablo Range (Figure 3). This block represents a complex history of Cenozoic deformation caused by reverse faulting with dips ranging from 30 to 50^0. Most of the folding is of Neogene age, a few are of Paleogene age. Evidence of post-Eocene uplift of the Stockton arch is observed from the fact that the Paleogene units truncate at the base of the Valley Springs Formation along the Diablo Homocline. The coarse alluvial fan deposits derived from the Diablo Range mark the beginning of the Neogene uplift of the Diablo Range during the Late Middle to Late Miocene. But the principal Neogene uplift of the Diablo Range began during the Pliocene and Pleistocene and resulted in forming the angular unconformity at the base of Tulare Formation (Bartow, 1985; Raymond, 1969).

The WFB comprises the southwestern side of the valley (Figure 3). It is located between the Panoche Creek on the north and the Elk Hills in the southwestern side. It includes the southern Diablo and the Temblor Ranges. The belt is characterized by Cenozoic faults and folds trending slightly oblique to the San Andreas Fault (NNW-SSE). In the northern part, the folding occurred in the Neogene and its intensity increased southeastward along the belt and southwestward towards the San Andreas Fault (Bartow, 1991).

M-TS covers the region between the Maricopa-Tejon subbasin and the south-margin deformed belt (Figure 3). It is the most deformed part of the basin which experienced a Late

Cenozoic shortening due to thrusting at the south margin and significant Neogene subsidence north of the thrust belt (Bartow, 1991).

Sedimentation in the San Joaquin basin is mainly governed by tectonism, and to a lesser extent, by eustatic sea level changes and allocyclic factors like climate (Bartow, 1991). As a whole, the sedimentary record depicts the complex interplay of all of these factors. Thick sediments in the southern San Joaquin basin indicate the effect of tectonic subsidence. Moreover, the location of the basin along an active continental margin generated prolonged tectonic activity during the Cenozoic. Most of the marine sequences are unconformity bounded and are easy to correlate within the basin. In a few cases, the equivalent non-marine sequence must be correlated based on the position of the bounding surfaces.

Plate movements greatly influenced the tectonics and hence, the evolution of the basin. A subduction zone has prevailed at the western margin of North America during Cenozoic times when the oceanic Kula plate subducted obliquely under the North American plate (Page and Engebretson, 1984). Bartow (1991) proposed that the rapid rate of convergence might have made this subduction zone to be of low angle. The fast convergence rate is also observed by the presence of relatively displaced arc magmatism eastward from the Sierra Nevada into Colorado (Lipman et al., 1972; Cross and Pilger, 1978). This oblique subduction at the central California margin continued until end of the Eocene when the Farallon plate displaced the Kula plate (Page and Engebretson, 1984). A decrease in convergence rates in the Late Eocene-Oligocene periods steepened the subduction zone and the volcanism, associated with the subduction process, migrated southwestward from Idaho and Montana into Nevada (Lipman et al., 1972; Cross and Pilger, 1978).

2.3 San Andreas Transform

The evolution of the San Andreas transform in the Mid-Oligocene period plays a key role in shaping the broad aspects of regional geology and structural provinces.

A triple junction is defined as the location where three tectonic plates are in contact with each other. The boundary between any two of the plates can be either a spreading center (ridge), a transform (fault), or a subduction zone (trench). The Mendocino triple junction (MTJ) and the Rivera triple junction (RTJ) were formed about 30 Ma ago off the coast of northern California because of geometrical consequences of the motions of three tectonic plates, the oceanic Gorda plate, the oceanic Pacific plate and the North America plate (Figure 5, Atwater, 1970; Furlong and Schwartz, 2004). The MTJ created a trench and two fault systems. The Gorda plate subducted under the North America plate to the east along the Cascadian Subduction Zone to make the trench. The right-lateral Mendocino Fault developed at the boundary between the oceanic Pacific plate and the relatively younger oceanic Gorda plate. Another right-lateral transform fault system, famously known as the San Andreas Transform, originated from the collision of the East Pacific rise with the North America plate during subduction (Engebretson et al., 1985). The migration of the MTJ northward along the central California coast coincided with pulses of initial subsidence in the Neogene sedimentary basins near the continental margin and with eruptions at local volcanic centers in the Coast Ranges (Dickinson and Snyder, 1979). The northern end of the San Andreas

Transform terminated at the MTJ. The RTJ moved southeastward and created a ridge-trench-fault system which formed the California Continental Borderland and the Gulf of California.

The transform gradually lengthened as the MTJ and RTJ migrated northwestward and southeastward along the continental margin due to an unstable configuration. The configuration was instable because the prior trench and newly developing transform were not collinear (the trend of the 3 plate boundaries did not intersect at a single point). It induced a series of extensional tectonic events (Dickinson and Snyder, 1979; Ingersoll, 1982). The motion of the pacific plate changed to a northerly direction about 5 Ma ago which yielded generalized compression normal to the San Andreas Transform (Minster and Jordan, 1984, contributing to compressional deformation at the western side of the San Joaquin Valley (Bartow, 1991).

2.4 Other Tectonic Factors

Beside plate tectonics, there are other regional tectonic events which also influenced the evolution of the San Joaquin basin (Bartow, 1991).

A clockwise rotation of the southernmost Sierra Nevada as evident in paleomagnetic data produced large en-echelon folds in the southern Diablo Range related to Late Cretaceous and Early Tertiary right-lateral strike-slip movement on the proto-San Andreas fault (McWilliams and Li, 1985; Harding, 1976). The proto-San Andreas fault is a large-scale shear zone, developed to accommodate the right-lateral motion of the Farallon plate during it's subduction

under the North America plate. Twisting and wrenching along the plate boundary resulted in the formation of a series of ridges and basins along the California coast (Bartow, 1991). Transgression and regression took place in the basins due to this tectonic force which caused the basins to rise and subside periodically. Also, large volumes of sediment from the ridges were deposited in fluctuating depositional environments ranging from deep, offshore marine to shallow, near shore marine, and even erosional surfaces as the basin floor must have risen above the surface of the ocean at different times.

The tectonic effect caused by the accretion of the Tujunga terrane to the North American craton (in the Mojave region) during the late Paleocene might have accelerated the formation of the echelon folding (Harding, 1976; McWilliams and Li, 1985). The uplift of the Stockton arch in the Early Tertiary served as a provenance (source location of sediments) for the Cenozoic sediments (Hoffman, 1964).

Before the actual arrival of the Pacific spreading ridge (East Pacific Rise) near the North American plate subduction boundary, the younger buoyant lithosphere component associated with the ridge was subducted in the southern part of the California during Mid-Oligocene time. This event had an effect on the southernmost San Joaquin basin as it resulted in a regional uplift of southern California and formation of fault-bounded alluvial deposition contributed to the growth of the basin (Nilsen, 1984; Crowel, 1987).

The extensional tectonism in the Basin and Range provinces due to Miocene faulting caused by the westward movement of the Sierra Nevada block had an effect on the evolution

of the San Joaquin basin. The arch-trench system on the plate boundary was developed due to the extensional stress regime in the Oligocene era. The transition from compression to intra-arc extension took place as the subduction angle steepened due to increased overburden hydrostatic pressure in the deep lithosphere. Intra-arc extension was replaced by back-arc extension probably due to a change in direction of subduction and the southwestward migration of the eastward limit of the subduction-associated magmatism. The intra-arc and back-arc extensions were oriented at right angles to the subduction plate boundary and might have contributed to the compression of the San Joaquin basin (Zobak et al., 1981). During Late Miocene, due to the associated Basin and Range left-lateral faulting, the basin shifted westward and created a bend in the San Andreas Fault which caused a change in structural style and varied the rate of sediment deposition in the basin (Bohannon and Howell, 1982).

The Neogene wrench tectonism due to a deep-seated thrusting along the southwestern side of the basin near the San Andreas Fault gave rise to a series of en-echelon folds, which deformed the San Joaquin Miocene deposits into a series of anticlines and synclines. The structural styles and the geometry of the Miocene sedimentary deposits within the San Joaquin basin varied spatially as evidenced in the stratigraphic records (depositional hiatus, provenance and spatial distribution of degree of sediment load within the Temblor formation) near the end of Saucesian time (Harding, 1976; Bridges and Castle, 2003). The depositional facies and structural styles of various hydrocarbon trapping formations in the western side of the San Joaquin basin were governed by this tectonism (Graham, 1985; Beyer, 1995). In stratigraphic records, synsedimentary deformation is reflected in the distribution, facies and sedimentary packaging of strata due to the presence of local unconformities within the

Temblor formation which might have been the effect of the Neogene wrench tectonism (Graham, 1985).

The deep-seated Cenozoic thrusting in the western side of the Sierra block due to northeastward movement of a wedge (an accretionary prism deposit located just below the North American plate at the subduction zone) of the Franciscan complex, between the Great Valley sequence and crystalline basement, initiated the Cenozoic activity in the Coast Range thrust (Wentworth et al., 1984). The Franciscan complex contains mélanges of sedimentary rocks, serpentinite, and blueschist in a sheared matrix and fine greywacke derived from the top of the Farallon plate generated from the escarpment during the subduction process. Whereas, the overlying Great Valley sequence consists of layered sedimentary sequences derived from volcanic sources deposited in the fore-arc region toward east (Hoots et al., 1954; Wentworth et al., 1984; and Wentworth, 1985).

The latest uplift of the Sierra Nevada is believed to have taken place during the Late Miocene period due to thermal thinning of the lithosphere below the Sierra Nevada. The lithosphere thinned as the subduction zone associated with the Mendocino triple junction passed northward (Mavko and Thompson, 1983). The acceleration in the San Andreas Fault slip rate during this period further deformed the already folded Sierra Nevada. The process contributed to the rapid subsidence of the southern San Joaquin basin in the Late Miocene period (to maintain isostacy) and shaped the evolution of the San Joaquin basin as large amount of space was created to accommodate sediments (Dickinson and Snyder, 1979; Davis, 1983). Furthermore, fault-normal compression in the Early Pliocene (5 Ma) generated many

folds and reverse faults parallel to the San Andreas Fault to accommodate the resulting strain (Zobak et al., 1987). Engebretson et al. (1985) opined that this compression might be the cause for the uplift of the Temblor and the Diablo Ranges, which made the oil fields of the basin shallower.

The San Joaquin basin was formed at the end of the Mesozoic on the southern part of an extensive forearc basin associated with the subduction of the Farallon plate under the North American plate. During the Cenozoic, the basin was gradually transformed into the present day hybrid intermontane basin. The geologic processes comprised a gradual restriction of the marine influx to the basin due to uplift of the northern part of the basin in the Late Paleogene period. In the Neogene period, the marine influx towards the westside of the basin was partially cut off due to uplift of the Diablo and the Temblor Ranges (Bartow, 1991; Harding, 1976). Finally, during the Late Neogene and Quaternary, fluvial to lacustrine sediments were deposited in the basin (Marchand, 1977; Marchand and Allwardt, 1981).

2.5 Subsidence history and Paleobathymetry

The Cenozoic subsidence history of the San Joaquin basin in relation to regional tectonics is not well studied (Bartow, 1991), except that it may be inferred from paleobathymetric data and from the present day characteristics of different stratigraphic units such as basinward-thickening trends of various strata. The studies by Dickinson et al. (1987) and Olson et al. (1986) suggest that the rapid subsidence periods may have occurred in Late Paleocene-earliest Eocene, Middle Eocene, Latest Oligocene-Early Miocene, and Middle-Late Miocene. Uplifts

occurred during the Oligocene and between the Early to Middle Miocene (Bartow, 1991). A thorough analysis of these rapid subsidence events may help in formulating the geohistory analysis (quantification of tectonic subsidence or upliftment by generating a total-subsidence curve considering paleobathymetric data, sediment depositional thickness and compaction as function of geological age), which may help in reconstructing the history of the basin evolution at different geological ages. In addition, the subsidence analysis may help in correlating the resultant sea level changes which affect the sedimentation in the basin.

Figures 6(a) to 6(j) depict the succession of the regional paleobathymetry trends from Late Paleocene to Pleistocene in the San Joaquin basin, as compiled from published maps and modifications based on recent sedimentological and stratigraphic data (Bartow, 1991). Bartow (1991) constructed these maps based on palinspastic reconstruction assuming 305 km of the Neogene right-lateral slip of the San Andreas Fault (Graham, 1978) and an unspecified amount of Early Paleogene right slip on the proto-San Andreas Fault (Clark et al., 1984).

2.6 Eustatic Sea-level Changes

The Early Cenozoic sedimentary history of the San Joaquin basin is characterized by extensive basin-wide spread of depositional sequences. During the Late Cenozoic period, localized thin sequences of shorter duration were also deposited. The change in styles of deposition took place during the Oligocene when the convergent continental margin transitioned into a transform margin. Tectonics (related to subduction and proto-San Andreas fault) had a greater influence on the Paleogene basin history than the change in eustatic sea

level (Bartow, 1991). Bartow observed that the regression at the end of the Upper Paleocene-Lower Eocene may be inferred from the global sea level fall as it created a wide-spread unconformity that can be correlated to several areas in Europe, and hence, may be attributed to global eustatic sea level falls rather than tectonism. Based on reviews of structural and sedimentological analyses of the basin outcrops by several researchers, Bartow (1991) opines that all other Pleogene regressions may be the effect of falls in eustatic sea level. During the Neogene, the eustatic sea level effects are less apparent except for a Middle Miocene highstand which resulted in wide spread transgressions in the San Joaquin basin (Graham et al., 1982; Haq et al., 1987).

2.7 Climate

The climate, along with tectonic processes and sea level changes, plays an important role for sediment composition (facies) and deposition. The climate affects the rate and amount of deposition in any basin. In an arid climate, the rate of sedimentation is slow which contributes to deposition of thin stratigraphic units. In a wet climate with larger water discharge into the basin, thicker stratigraphic units are deposited in the basin.

The San Joaquin basin experienced warm global climates in the Late Cretaceous, which changed into a cool glacial climate in the Quaternary. The Eocene experienced the warmest climates due to a low latitudinal temperature and high precipitation (Frakes, 1979). In the Oligocene, glacial conditions prevailed in Antarctica which caused a decrease in sea water temperature and led to a cooler global climate. During Late Oligocene, Miocene, temperatures

warmed although to a lesser degree than during the Eocene (Addicott, 1970). In the Late Pliocene, the Sierra Nevada experienced the effect of the alpine glaciations (Frakes, 1979).

The occurrences of quartz-kaolinitic sandstone, lignite, and laterites in the Eocene reflect the prevailing warm and tropical climate condition (Bartow, 1991). The sedimentation from glaciers in the Sierra Nevada constituted the San Joaquin basin alluvial sediments during the Late Pliocene. The pluvial climate of the Pleistocene contributed to the creation of a series of lakes in the San Joaquin Valley (Bartow, 1991).

The preceding discussion on the role and effect of various geologic processes including the effect of plate movements, that acted to shape the evolution of the San Joaquin basin in the Cenozoic, clearly indicates the structural, sedimentological and depositional complexities that the basin had experienced in the geological past.

Chapter 3

Study Area

The study area lies in the southern part of the Chevron's West Coalinga oil field in California (Figure 7). The areal extent of the study area is about 1 x 3 miles out of the field total of 2 x 14 miles. The present study focuses on identification and delineation of various geologic depositional process features within the Temblor reservoir of the West Coalinga field. 3D poststack seismic data merged from different seismic volumes, which were acquired independently between 1996 and 2000, are used for the analyses to ascertain sequence stratigraphic, paleogeomorphic depositional features and their spatial distribution over the area of study.

3.1 Coalinga Heavy Oil Field

Coalinga is a giant oil field in the San Joaquin valley of California with an extremely complex reservoir stratigraphy. The field has produced over 888 million barrels oil (MBO) of API gravity 20^0 from the clastic Temblor formation (Miocene) since the early 1900's. As of 2002, the balance of oil in-place reserves of the field is 2240 Mbbl out of total initial estimated reserves of 81,801 Mbbl (DOE, 2005). The field is now in its tertiary development stage. The

Coalinga anticline is one of a series of echelon folds that modify the generally homoclinal eastern flank of the Diablo range along the western side of the San Joaquin Basin of California (Figure 8). The reservoir units outcrop a few miles to the north of the reservoir (Bridges and Castle, 2003).

The Coalinga field is divided into East Coalinga and West Coalinga based on the structural setup (Figure 9), which influences production and distribution of producing wells. A northwest-southeast trending anticline (Coalinga nose) separates the two fields. The nose and East Coalinga eastern part cross regional strike and extend about five miles along the southeast plunge of the nose (Clark et al., 2001b). The West Coalinga field parallels the upturned, monoclinal west margin of the basin.

The field is part of the Kreyenhagen-Temblor petroleum system that derives oil from the organic-rich shale of the Middle Eocene Kreyenhagen Formation (shale) as observed from the geochemical data analysis of the Kreyenhagen 74X-21H well (Peters et al., 1994). The reservoir trap is stratigraphic in nature. The reservoir rocks outcrop at the west margin where historical oil seeps and breaches were reported. The tight outcrops and solidified tar mats in the near surface of these outcrops provide the sealing mechanism (cap rocks) of the Temblor reservoirs (Figure 10). The accumulated heavy oil is produced by steam injection which fractionates the high-gravity oil beneath these sealants into low-gravity crude (Clark et al., 2000). At places, shales and calcite-cemented sandstones in the upper part of the Top Temblor (C-sand of Bates, 1985) create an effective top seal in the reservoir (Clark et al., 2001b).

The reservoir rocks are highly heterogeneous due to their proximity to the tectonically disturbed San Andreas transform.

3.2 Reservoir Characteristics

The Temblor Formation sandstone contributes 90 percent of the total oil production as of 2001 (Clark et al., 2001b). The average well depths range from 500 to 4500 feet. As of 2001, the total number of wells exceeded 4000. The reservoir shows an average porosity of 0.34 and permeability ranging from 20 to 4000 millidarcies. The reservoir is about 700 feet thick in the east margin of the field (down dip), but gradually thins towards west as it is truncated by the overlying Etchegoin Formation, which is a Pliocene oil producer. The reservoir rocks crop out along the west margin of the field. The oil seeps on the outcrops which were the pathfinder for the discovery of the field, ceased flowing as the field underwent development. Presently, about 2000 wells are under production by steam injection. About three to four barrels of steam are being pumped into the reservoir for every single barrel of oil recovered. The field requires more steam to be injected to produce oil than most other heavy oil reservoirs in the San Joaquin basin due to its geological complexities (Clark et al., 2001b).

3.3 Production History

The first producing well, known as “Wild Goose”, was drilled in 1887 in the northwestern part of the field near the tar seeps of Oil City. The well penetrated a fractured Cretaceous

section and produced ten barrels of oil per day (BOPD). The "Blue Goose" well in the Oil City shale produced about 1000 BOPD in 1897 (Clark et al., 2001a), but the fractured reservoir declined rapidly and explorationist's attention was drawn to the Temblor sandstone in the Coalinga Nose anticline on the east side of the field and towards the west of Coalinga in the homoclinal limb. The prolific producing well, known as "Silivertip" (10,000 to 20000 BOPD), was drilled in 1909 (Arnold and Anderson, 1910; Kaplow, 1945). Production from the field reached 53,500 BOPD in 1912, but gradually declined to 9,000 BOPD during 1930s. Most of the wells produced a few barrels of heavy oil (10-20^0 API gravity) per day. Extensive drilling activities during World War II increased the production figure to 29,000 BOPD, which declined gradually until Shell Oil Company undertook the steam injection project in 1961 (Clark et al., 2001a). The tertiary recovery phase (production by steam injection; usually follows the water flooding which is known as secondary production phase) started in 1979. With a dramatic increase in the steam injection rate, the crude oil production figure reached 34,000 BOPD in 1991, but the annual production figure kept on fluctuating depending on the steam injection activities (Figure 11). As of 2001, the field was producing about 25,000 BOPD of oil from 2000 wells with a steam injection of 80,000 barrels per day (Clark et al., 2001b). The annual oil production from the field in 2003 is 6.5 Mbbl and the field is ranked ninth amongst California oil fields (DOE, 2005).

3.4 Reservoir Architecture

The reservoir architecture of a field describes both the producing reservoir as well as the non-productive rocks in three dimensions. Two components describe the architecture. The first one deals with the structural and stratigraphic aspects of geological chrono-stratigraphic surfaces and the second component demonstrates the lithofacies distribution between these surfaces. The time-significant surfaces cover sequence stratigraphic elements such as down lap truncations, flooding surfaces and regressive unconformities. These surfaces are better characterized on seismic data than on a geological model because 3D high-resolution seismic provides data without gaps over long scales. The lithofacies distribution results from mapping of rock-facies from well, cores and outcrops. Generally, they are interpolated over the field area based on some geological concepts and modeling. However, forward modeling of well data to interpret seismic data and/or their inversion with the help of well data to ascertain the geological parameters and signatures, along with the use of these geological data, often helps in identifying the litho-stratigraphy of a field with a greater degree of confidence. Properly delineated reservoir architecture helps in planning and execution of field development and production.

The Temblor Formation represents the interplay of shallow marine and non-marine depositional environments. The clastic shallow, unconsolidated reservoir is very heterogeneous in nature, as it is mostly bounded by unconformities. Outcrop and well data analysis identifies the Temblor Formation as an upward deepening depositional succession.

Figure 12 shows the paleoshore line of the Temblor formation in the study area wherein the sea was deeper towards eastern side (Bridges and Castle, 2003). Geological studies of outcrops, cores and gamma ray log (Bridges and Castle, 2003) showed that the reservoir is subdivided into three distinct depositional environments representing a near-shore fluvial dynamic depositional setting intermingled with depositional erosional hiatuses. Figure 13 shows the generalized stratigraphy of the Coalinga area. The Temblor formation (Lower to Middle Miocene) overlies the Kreyenhagen crystalline clastics of the Eocene. The base of the Temblor is formed by an unconformity (Base Temblor) representing a time period of 21 million years of non-deposition and aerial exposure (Bate, 1984; Bartow, 1991). The Base Temblor unconformity is considered equivalent to the bounding surface 1 (BS-1) of Bridges and Castles (2003) classification. This regionally extensive Base unconformity was the result of a low relative regional sea level (lowstand) in the basin due to tectonic uplift (Bridges and Castle, 2003). The top of the Temblor is demarcated by a regional angular conformity (Top Temblor) equivalent to BS-6 of Bridges and Castle (2003). The Santa Margarita Formation (Upper Miocene) overlies the Temblor in the north. To the south, the Etchegoin formation (Pliocene) overlies this unconformity because the Santa Margarita Formation was eroded out. The Top Temblor unconformity represents a period of 5 million years of non-deposition and erosion (Bate, 1984; Bloch and Graham, 1991) caused by the tectonic uplift of the Diablo Range (Harding, 1976; Bate, 1985). Based on litho-stratigraphic correlation and facies tract analysis, a regional unconformity (Button unconformity) demarcates the reservoir facies deposited on top of the Base temblor ( ). This unconformity is equivalent to BS-3 (Bridges and Castle, 2003), a transgressive depositional lag with a base of Oyster bed which separates the shoreline facies “Button Beds” (Bridges and Castle, 2003) from the underlying lowstand

and estuarine facies. The reservoir on top of the Button unconformity is overlain by the Valv unconformity, identified by the presence of a diatomite bed right underneath (BS-5 of Bridges and Castle, 2003). The Valv unconformity was formed as a response to the uplift caused by the beginning of the rapid movement along the San Andreas Fault (Casey and Dickinson, 1976).

The surfaces BS-2 and BS-4 of Bridges and Castle (2003) are based on the facies changes observed in the sedimentological analysis of cores, outcrops, and the presence of barnacle shells. The formation thicknesses bounded by these surfaces are relatively thinner and are not being considered for the present seismic analysis as it is difficult to map these thin sequences on the seismic data.

Current (2001) identified eight lithofacies in the Temblor Formation based on core and outcrop analysis. These are Sand, Burrowed Sand, Laminated Sand, Silt and Clay, Fossiliferous Sand and Clay, Burrowed Clay, Limestone, and Calc-cemented Sediment.

Bridges and Castle (2003) carried out extensive analyses of cores and outcrops around Coalinga field and formulated five facies tracts (Table 1). They attributed the occurrence of these facies tracts to relative rise in sea level caused by basin subsidence during the Temblor deposition and attributed the cause of subsidence to the regional tectonic extension related to strike-slip movement associated with the San Andreas transform. The incised valley fill (IVF) facies tract was deposited on the Base Temblor unconformity on incisions into the Kreyenhagen Shale during the lowstand period. This tract was overlain by an estuarine facies

caused by local subsidence and rapid sedimentation (Figure 14). The basin then experienced deposition of tide- to wave-dominated progradational facies on top of the Buttonbed unconformity, probably due to the uplift of the Diablo Range (Hoots, 1954)) and the associated relative sea level changes on the eastern side of the San Joaquin basin (Bloch, 1991). Diatomite was deposited above the tide to wave facies in brackish to shallow marine environments as a result of relative sea level fall (Bridges and Castle, 2003), which was capped by the Valv unconformity at a later stage. Subtidal deposits that occurred due to a subsequent rise in sea level overlie the diatomite facies tract. The zone is also bioturbated. Finally, the Temblor Formation was capped by the Top Temblor unconformity (BS-6 of Bridges and Castle, 2003) which separates the Temblor formation from the overlying Santa Margarita and Etchegoin formations on a regional scale (Bate, 1984; Bartow, 1991). Table 1 lists the various facies tracts present in the Temblor Formation and their characteristic features.

The four unconformities (Base Temblor, Buttonbed, Valv, and Top Temblor in ascending order) described above play significant roles in the distribution and flow of fluids in the reservoir. The variability associated with the above facies tracts renders the reservoir highly heterogeneous and highly variable in porosity and permeability distribution. Earlier research to delineate the reservoir focused more on borehole or exposed outcrops in the northern part rather than a detailed and integrated seismic approach (Clark et al., 2001b). With the absence of extensive data continuity over the field, the gaps were filled by conceptual modeling which in some cases may introduce biased or inappropriate views (Clark et al., 2001b). The thicknesses between the three facies tracts within the Temblor Formation vary over the field

due to the presence of dynamic paleotopography in the basin caused by varying degrees of tectonic uplift and differential amounts of sedimentation through out the period of deposition and erosion. The seismic characters of these unconformable surfaces are subtle in nature and are easily overlooked in the field area without prior stratigraphic knowledge based on cores and outcrops (Clark et al., 2001b).

In the present study, the continuous 3D seismic data was integrated with the geological data to verify, analyze, and map spatial distribution of these unconformities in the reservoir for a meaningful characterization. In the seismic data, paleogeomorphic and depositional features were sought after which were the preserved resultants (features) of the various tectonic forces that acted on this complex strike-slip reservoir in the geologic past. In addition, the present study helped to ascertain the lithology distribution of these features which will allow further studies on tertiary recovery and enhanced reservoir modeling.

Chapter 4

Seismic Details

As discussed in Chapter 3, during the tertiary recovery phase of the field, about four barrels of steam volume are injected to recover one barrel of crude oil. This may be due to the field's inherent complex stratigraphy which makes it difficult to properly ascertain and delineate the spatial distribution of lithofacies and permeability. Without characterization of reservoir geometry and inter-well connectivity at adequately short scales, a lot of steam is wasted and is not confined to the development block. To gain a better understanding of the complex reservoir stratigraphy and a more accurate delineation of the reservoir, Chevron carried out a number of 3D seismic surveys over the field between 1996 and 2000 (Figure 15). A first 3D seismic survey covering about one square mile over section 36D towards the southern part of the field was obtained in 1996. This survey was designed to be a pilot study for data acquisition and quality control, but it was also intended to serve as a baseline for future time lapsed seismic surveys. A vibroseis source with a frequency range of 10-70 Hz was used for most of the survey. However, in areas with complex topography or access problems, explosion sources were used instead. The frequency range between 25 and 30Hz was deemed the best and declared the desirable range for the upcoming surveys (Clark et al., 2001b). The second survey, covering an eight square mile area with the same acquisition parameters, was carried out in 1997. This survey also overlapped

with the first one over section 36D to study the effect of one year of steam injection into the block. The third survey in 1998 covered an area of two square miles over the north of the field. The subsequent 3D surveys in 1998 mostly covered the area towards the northern half of the field. Two additional 3D seismic surveys were carried out in 2000, covering both northern and southern parts of the field to provide a repeat seismic coverage for time lapse analysis.

The study area covers sections from 36D, 25D, and 24D (Figure 15). The present 3D seismic data set is a merged poststack data cube from all these surveys (Figure 16). The CDP spacing is about 60 feet in both inline and crossline directions. The data set consists of 2,263,483 traces.

4.1 Effect of steam on seismic

The seismic surveys were carried out over the field while steam was being injected intermittently in the reservoir. Thus, the acquired seismic data are affected by the presence of varying proportion of steam in the reservoir. The reservoir rocks exhibit dramatic spatial and temporal changes in pore pressure, temperature, and fluid saturation due to the presence of steam (Ito et al., 1989; Wang and Nur, 1989). The temporal and spatial variations in rock properties cause seismic wavefield distortions throughout the steamed regions of the reservoir. For the same formations, seismic impedance contrasts vary largely because of the presence of trapped steam, which causes misleading seismic reflections and diffractions.

The heated steam also causes variations in reflection amplitudes due to impedance contrasts when steam saturated (hot) sandstone, oil-water saturated (cold) sandstone, or mudstone/shale are juxtaposed. Ecker, et al. (1999) investigated the effect of heated steam on the time-lapse seismic data of 1996 and 1997. They calibrated the seismic data sets with log and production data, and created transforms using rock physics relations and forward modeling to identify the effect of reservoir temperature and steam on the seismic amplitude. Figures 17 show the seismic amplitude variations on top of the reservoir between 1996 and 1997 while steam aided production activity was continuing.

Velocity pull-downs in seismic images associated with the thermal effects and amplitude focusing or attenuation are commonly observed. Lumley, et al. (2001) carried out a detailed study of the effect of steam and temperature based on Coalinga core samples and observed that P-wave velocity (V_P) decreased by about 1% for every 19^0 Fahrenheit increase in reservoir temperature; moreover V_P decreased by 8% with the presence of steam. They observed that by the combined effect of steam and increased temperature, V_P may change as much as 25%. Detection and mapping of these changes may illuminate the present oil distribution and fluid flow pattern over the area. These in turn may indicate the presence and continuity of porous and permeable zones in the reservoir which may allow optimization of the reservoir production strategy.

Variable vertical and lateral steam injection severely affects the seismic interpretation. Velocity variability resulting from steam injection makes time-depth conversion difficult, as precise well ties between wells and seismic data are seldom possible. The wireline logs are

recorded at different times during the development of the field with different generations of well logging technology and varying calibration of logging equipment. Also, the well logs recorded during and after the intermittent steam injection are affected by the presence of steam in the formation as steam trapped in the formation may affect the resistivity, porosity and interval velocity response of the reservoir rocks (Butler and Knight, 1995). The seismic data are also recorded at different times having differential effects of steam. Thus, the ties between data and well logs become problematic and vexing. The identification of sequence stratigraphic elements like offlap, onlap, and truncation analyses on seismic data becomes perplexing due to the discontinuous nature of the reflector pattern and the associated dipping events. The problem is further complicated when the reservoir is comparatively thin, for example, in the Temblor formation.

To study the effect of steam on the velocity V_P and reflection coefficient values between fluid/gas and steam saturated sand and clay, an analysis was carried based on reported experimental and analytical values of bulk modulus, shear modulus, density, V_P, and S-wave velocity (V_S) of dry rocks, frame matrix, and water/oil/gas/steam saturated rocks (Mavko et al., 1998). The Gassmann's fluid substitution method (Gassmann, 1951; Mavko, et al., 1998; Wang, 2001; Han and Batzle, 2004) was used to compute the moduli of oil/gas/steam saturated rocks relative to water saturated ones (Table 2). A porosity of 0.36 was assumed as observed for the portions of the Coalinga Temblor reservoir. The bulk moduli of saturated rocks and that of fluid (gas and steam) were extrapolated to actual reservoir pressure and temperature condition using the relations reported by Mavko, et al. (1998). Table 2 shows that V_P for steam saturated sand may decrease by 27% compared the one for oil saturated sand.

This finding is consistent with the result of Lumey, et al. (2001) on the reservoir rocks. The largest reflection coefficient is observed for clay over steam/gas saturated layers.

4.2 Effect of merged data set

The seismic data is merged from four different 3D seismic surveys carried out between 1996 and 2000 with overlapping areas. Each data set was acquired after injection of varying amounts of steam into the reservoir and with varying sources (vibroseis or dynamite). Signal-to-noise levels vary between surveys. Moreover, the static corrections applied to each of the 3D data sets during prestack processing may be different and inconsistent between surveys. There may be also some differences in location of inlines and crosslines between surveys.

The oil production along with steam injection affects the interval velocity of the reservoir rocks. After oil production, the depleted reservoir is saturated with a mixture of light hydrocarbon gases, steam, carbon dioxide and monoxides, nitrogen and sulfur gases. These zones may behave like an air-saturated lithology which affects the velocities, amplitudes, and thus, reflections.

The reflectors are very discontinuous in the merged data set (Figures 23a, 24, and 26b). These discontinuities may be due to either the geological complexities associated with multistoried, stacked, and restacked channels with their changing depositional directions as identified in subsequent chapters, or the effect of steam and oil depletion. The reflection and

amplitude strength over the area is profoundly erratic and discontinuous in places which may be attributed to the effect of steam injection activities during successive seismic data acquisition between 1996 and 2000. The reflectors in the central part of the study area between the upper 36D and lower 25D sections are already more discontinuous by geology, which renders interpretation very challenging and time consuming as reflector mapping was difficult and loop closing contradicts geological expectations in some places. The problem gets more pronounced where reflectors merge, for example, the merging of the Buttonbed and the Valv unconformities in the western part of the area on the boundary of sections 25D and 36D (Figures 24 and 26b). The data set falsely suggests a heavily faulted environment. The significant static break due to a decrease of the interval velocity near the top of section 25D may be attributed to an excessive amount of steam that was placed into this section (William Kempner, 2003, personal communication), which caused a differential delay in time arrivals. The steam effect is further evidenced by the fact that all the reflectors above the reservoir look fairly stable, but inside the reservoir, there is a shift of as much as 100 ms for certain reflectors which gives the false impression of a faulted area (Figures 23a, 24, and 26b). A time shift of 100 ms would indicate a reservoir steam thickness of 164m (Table 2), which seems to be in the higher side considering the average reservoir thickness (260m). At the boundary between sections 24D and 25D, there is a significant time shift and frequency change due to the steam effect. A similar change is observed between sections 25D and 36D. It is also observe that there are reflector misties between inlines and crosslines at these boundaries which become more pronounced toward the western edge of the area (Inlines 95 to 70).

To solve some of the above difficulties associated with the merged data set, a novel technique (Mahapatra et al., 2003b) was developed which will be discussed in Chapter 5.

Chapter 5

Seismostratigraphic Interpretation

Density and sonic wireline logs of twenty-seven wells were correlated (Figure 18). The reservoir rocks show vertical variations in degree of sediment compaction trends. Shifting of the shale base lines (the line of average wireline log parameter for shale/sand lithologies) is observed with respect to each unconformity bounded formation due to differences in the degree of compaction of shales and sands caused by varying overburden thicknesses and time period of nondeposition. The neutron porosity logs were examined where the exact picking of the unconformity was doubtful on density and sonic logs as variations in compaction factor also affect the porosity values. Four unconformable surfaces (Base Temblor, Buttonbed, Valv, and Top Temblor), based on the shale base trend line shifting, were identified (Figures 19 and 20). Based on wireline log correlation, the depth picks were interpolated to generate structure contour maps on top and bottom of the Temblor and isopach map for the entire Temblor Formation (Figure 21). The generic strike of the Temblor formation seems to be along the NNE-SSW direction. The top of Temblor is observed to be shallowest towards the northwestern corner of the area and is deepest towards SE in the seismic coverage area. The highest structural relief on the Base Temblor unconformity seems to be towards the southwestern corner which seems to be deepening towards NE in the seismic coverage area. The thickness of the Temblor formation is increasing downdip

towards east. The direction of sediment deposition seems to be slightly changing over the field ranging from NW-SE to SW-NE during the Temblor deposition.

The time equivalents of these unconformities were posted onto the poststack 3D seismic data. While trying to identify and map these surfaces on the seismic data, severe misties and reflector discontinuities on the seismic sections were observed because the 3D data set was actually merged from different surveys acquired at different times in a geologically complex area with multiple phases of steam injection. Mapping these unconformity reflectors was problematic especially in the central part of the area (Figure 22). Reprocessing the data was deemed too time consuming and beyond the scope of the present investigation. Instead, a novel technique was developed to aid the interpretation (Mahapatra et al., 2003b). A deeper, relatively continuous reflector within the Kreyenhagen formation was mapped. It is envisaged that geologically older formation like the Kreyenhagen might be a more compact and comparatively layered deposit with good reflector continuity over the area. This mapped reflector was then flattened. As the two-way time for the deeper layer is made constant by flattening, the misties in the overburden are reduced considerably on this flattened volume and the continuity of the four unconformities within the reservoir is improved (Figures 23a and 23b). The flattened volume with appropriately time-shifted wireline data allows identification and interpretation of the unconformities in the originally discontinuous seismic volume. There remains a reflector mismatch, however, when following reflectors from the north to the south, or vice versa which may be an effect of the steam injection or data merge.

After applying the flattening technique, the fourth-order unconformities within the Temblor formation were mapped on the seismic data with the help of the posted well log picks. It was confirmed that the reservoir is compartmentalized into three major vertical stratigraphic sequences (Figure 24). In the western part of the study area, the Buttonbed and Valv surfaces appear to be merging which implies that a portion of the Buttonbed unconformity has been eroded by the overlying Valv unconformity (Figures 24 and 26b).

Confidence maps depicting the degree of reliability of seismic loop tying the reflectors in the Temblor formation were generated based on a weighted combination of time-shift, amplitude value and wavelet width (Figure. 25; Mahapatra et al., 2005). The confidence map of the Base Temblor shows poor reflector continuities indicating a pattern resembling channel like discontinuity feature. The confidence map on the Buttonbed unconformity may be due to this paleotopography. However, discontinuities of the Valv are observed towards the west instead which suggested the existence of geological discontinuities on the Valv. The confidence map on the Top Temblor indicates a minor difficulty towards the northern part of the area which may be due to the presence of weak reflectors, caused for example by a lesser change in velocity contrast as demonstrated on the apparent polarity attribute volume (Figures 47 and 48).

Seismogeological sections were prepared along and across the study area (Figures 26a and 26b). The two-way time thickness of the Temblor formation is between 240-260 ms (130-150, 30-40 and 35-40 ms, respectively, for the formation confined between the Base Temblor and the Buttonbed, between the Buttonbed and the Valv, and between the Valv and the Top Temblor). The reflectors dip eastwards while the time-thicknesses are observed to be maximal towards the

northern part of the area, decreasing towards the southern part. On seismic data, onlaps and reflector truncations are observed against the unconformities (Figures 27 and 28), which allow their identification as sequence boundaries. The zones between Valv, Buttonbed, and Basal Temblor surfaces contain a multitude of channel-like shaped cuts (Figure 24 and 28). In the lower central part of the study area, these channels appear to be recut and restacked which is more prominently observed in the dip direction (Figure 28).

Structure contour and isochron maps were prepared for unconformities and unconformities bounded facies tracts within the Temblor Formation (Figures 29 to 37). The generic dip direction within the Temblor formation observed to be along E-SE direction. The thicknesses of the unconformities bounded zones between the Top Temblor, Valv, and for the entire Temblor are increasing downdip towards east and are at maximum in the northeastern corner of the area. However, in case of the zone between the Base Temblor and Buttonbed unconformities, the thickness increases downdip with the maximum isochron observed in the eastern central part of the area. The probable cause may be due to lithology variation within the channel-like features because sand is less compactable than clay which decreases the P-wave velocity.

The seismostratigraphic analysis helped to compartmentalize the unconformity-bounded reservoirs based on the wireline log analysis and mapping of unconformable reflectors on the seismic data. The identification of various sequence stratigraphic elements (offlap, etc.) greatly helped in mapping the unconformities at places where the reflections are distorted. It also helped in confirming the correctness of the reflector mapping and the presence of these higher-order unconformities within the reservoir. The analysis of reflector trends and unconformable

sequences enabled to ascertain the geological picture of the reservoir rocks such as the thicknesses, strikes, and variations in the dip direction for these sequences.

Chapter 6

Seismogeomorphic Interpretation

6.1 Seismic Attributes

Seismic attributes are useful to help the qualitative interpretation of the seismic data. Seismic attributes are derived from basic seismic measurements. The attributes are useful to ascertain structure, lithofacies, and reservoir parameters of a field as attribute properties can vary significantly with variations in lithology, geometry, and structural patterns of deposition for various lithofacies in an area. The basic poststack attributes may be grouped into the following classification (Brown, 1996).

Time-derived:	provide structural information.
Amplitude-derived:	provide stratigraphic and reservoir information.
Frequency-derived:	provide additional stratigraphic and reservoir information.

Poststack attributes can be extracted along one horizon, summed up over a window or formation, or point wise for the entire volume. The values within a window may be taken as a whole representing gross attribute measurement or at selected time intervals within it. Hybrid

attributes are generated by the combination of time, amplitude, and frequency information (Tanner, et al., 1994). Many seismic attributes have been invented and calculated using a variety of methodologies, such as complex trace analysis, Fourier analysis, correlation measures, wavelet analysis, principal components analysis, and empirical methods (Barnes, 2001). The use of various color schemes and illumination techniques for data display render attributes more accessible to the interpreter, especially with the development of interactive workstations with visualization software.

Coherence and Continuity:

The attributes measure the degree of similarity (continuity) or dissimilarity between seismic traces by using a variety of mathematical approaches similar to correlation (Marfurt et al., 1998). Coherency is often studied on time or horizon slices. The attribute highlights discontinuities which may be the result of faulting or sediment-deposition features including channels, levees, etc. because faults and channels are clearly outlined (Bahorich and Farmer, 1995). This attribute is free from interpreter bias as it is computed for entire data volumes instead along interpreted horizons, although acquisition and processing artifacts may still influence the attribute. It differs from normal time slices in that the structural features are visible irrespective of the time slice orientation (strike or dip). The resolution of the discontinuity is better as the coherency attributes undergo repeated simultaneous cross correlation calculation between the adjacent seismic traces. It helps in computing related attributes such as dip and azimuth of the correlation (Brown, 1996). Figure 38 shows major discontinuities in regular time slices. Figure 39 shows a coherency map

extracted from the seismic data flattened at the top Temblor. The figure outlines discontinuities with channel shape and depicts the lateral extent of these features.

Instantaneous attribute:

Instantaneous attributes quantify wavelet shape at any sample point in a concise manner. Instantaneous attributes are computed sample by sample, and show instantaneous variations of various parameters. Instantaneous attributes such as trace envelope, its derivatives, frequency, and phase may be determined from complex trace analyses (Taner et al., 1979). The instantaneous attributes of amplitude, phase, and frequency at the peak of the trace envelope (known as wavelet attributes) provide a way of representing the size and shape of a reflection. For example, instantaneous frequency at the peak of the envelope is equal to the mean frequency of the wavelet amplitude spectrum (Taner, 2001).

The instantaneous amplitude gives a measure of reflection strength (magnitude) and often serves as a lithology identifier. The instantaneous phase gives the polarity and symmetry characteristics of the wavelet as the phase angle changes with change in lithology which is a good indicator of lateral continuity. The instantaneous frequency is the time derivative of phase (Barnes, 1991; Cohen, 1995). The instantaneous frequency attribute responds to both wave propagation effects and depositional characteristics and may be used as discriminator (Taner, 2001). It is a possible indicator of hydrocarbons and fracture zones indicated by low frequency anomalies. Often higher frequencies indicate sharp interfaces such as exhibited by thinly laminated shales. Lower frequencies are indicative of more massive bedding geometry,

e.g., sand-prone lithologies (Taner, 2001). Taner observed that in case of a thin bed "*instantaneous frequencies jump or exhibit a negative sign. These sign reversals are caused by closely arriving wavelets. Therefore, the time derivative of the phase function will contain the indicators for thin beds, in the form of large variations of instantaneous frequency. Its smooth variation will relate to bedding characteristics*." Thus, the instantaneous attributes are excellent visual aids for interpretation. However, noise and multiples significantly affect the instantaneous attributes. Precaution should be taken to remove any variation in basic wavelet shape during processing that is not attributable to the subsurface geology. These attributes do not lend themselves to direct interpretation, except for isolated gas sands where they can be the direct indicator (White, 1991). These attributes may be logically, statistically, and mathematically combined in any fashion to form hybrid attributes. Relationships between the attributes are observed either by multi linear regression or by neural network analysis (Taner, 2001). These hybrid attributes may lead to a conclusive interpretation. Lynch and Lines (2004) describe that a display of various combinations of instantaneous attributes along with proper coloring, contrast, and display planes may help in ascertaining three-dimensional structure and may greatly help interpretation.

The instantaneous attributes are computed from the complex trace. A seismic trace can be expressed as the complex function,

$u(t) = x(t) + ih(t)$, where $x(t)$ is the real observed seismic trace

The imaginary part $x(t)$ of the complex signal is called the quadrature and is formed by Hilbert transformation (Figure 40).

The vector length of the real and complex conjugate amplitude values at an instant in time results in the instantaneous amplitude *r(t)*. Instantaneous phase *f(t)* is assessed by the angular deviation of this vector from the real axis. Instantaneous frequency is the rate of change of instantaneous phase as a function of time. The instantaneous attributes of frequency and phase are amplitude independent and are often severely affected by noise, which sometimes renders them uninterpretable (Taner, 2001).

Instantaneous Amplitude:

It is a measurement of the complex trace amplitude which may be visualized as the envelope of the seismic trace. It is defined as the total energy of the seismic trace and is independent of phase. Instantaneous amplitude attribute is also known as reflection strength attribute. The maximum reflection strength corresponds to the combined envelope of both peak and troughs in the real seismic. The reflection strength values are always "greater than" or "equal to" zero (Partyka, 2000). It is the square root of the trace energy and hence, may show where the maximum energy occurs. Taner et al. (1979) define reflection strength e(t) as:

$$e(t) = [\, x^2(t) + h^2(t) \,]^{1/2}$$

High reflection strength may be associated with major lithologic changes as well as oil and gas accumulations. Subtle lithological changes which may be inconspicuous in the seismic data may be delineated with the help of this attribute (Lynch and Lines, 2004). High reflection strength is often associated with gas filled pores. Reflection strength variations may

correspond to changes in acoustic rock properties and bed thickness and may also be used to distinguish massive reflectors from thin-bed composites (Partyka, 2000). In an unconformity, the energy strength will vary as lithology along the unconformable surface changes. Figure 41 presents a regular time slice within the reservoir depicting the reservoir facies tracts distribution. In the figure, the high amplitudes shows sinuous feature which moves shift SE with depth.

Instantaneous Phase:

It defines the angle between a rotating vector (formed by the real and imaginary components of the trace) and the real axis, measured as a function of time (Taner et al., 1979). The attribute is also known as arctan (α).

$$\alpha = h(t)/x(t)$$

Its values range from -180^0 to $+180^0$. It shows the lateral continuity of events as the phase angle changes with change in bedding continuity. It helps in detecting pinchouts, channels, fans, and internal geometries like different layer stackings. The most likely place to find good reservoir zones will be in sedimentological structures and depositional features such as incised valley fill channels of lowstand sand deposit which corresponds to high energy deposits with good sorting and good porosity. Thus, the attribute may help in characterizing the porosity cube. Moreover, the wireline porosity information may be tied back to these features to aid interpretation. Figure 42 reveals sedimentary layering patterns and identification of sequence boundaries based on reflector onlapping. Change in instantaneous phase of reflectors indicates

the bedding continuity.

Instantaneous frequency:

It is derived as the rate of change of the instantaneous phase as a function of time (Barnes, 1991; Cohen, 1995). It may jump or show a negative sign due to wavelet interference in thin beds (Taner, 2001). It may reveal pinch outs and the edges of hydrocarbon-water interfaces. Furthermore, it may provide information about the frequency signature of events, the effects of absorption and fracturing, thin-bed tuning due to wavelet interferences, and depositional thickness (Taner, 2001).

Often thick zones show lower frequencies due to high frequency attenuation, and thin layer exhibits higher frequencies. Low frequency shadows may be associated with the reflectors below gas sands, condensate, oil reservoirs, and steam. The shadows occur beneath zones with high attenuation, for example gas sands. The high frequency portion of the power spectrum of a seismic wavelet is attenuated more than the lower portion when the wavelet passes through this zone. The reflections coming from beneath this attenuative zone thus combine a greater portion of low frequencies because high frequencies were attenuated by the overlying zone (Barnes, 1993a). However, the shadow effect is only confined to the directly underlying zone as over depth, the time average effect may neutralize the spatial frequency differences. Figure 43 shows low frequency zone over high amplitude sand probably due to the trapped steam leakage in the overlying zone. The lower frequency shadow is seen above high amplitude sand which shows high frequency. The injected steam into these sand might have been leaked to overlying formation.

Instantaneous Bandwidth and Instantaneous Dominant Frequency:

Instantaneous bandwidth and instantaneous dominant frequency can be used as complex trace attributes (Taner and Sheriff, 1977; Taner et al., 1979). Instantaneous bandwidth is the absolute value of the rate of change of the instantaneous amplitude divided by the instantaneous amplitude (Barnes, 1993b). Variation in the instantaneous bandwidth suggests sharper amplitude changes related to changes in lithology, while zero instantaneous bandwidth represents uniform lithology. Figure 44 depicts the instantaneous bandwidth indication of lithology variation in a regular time slice in the Temblor. A zero instantaneous bandwidth (red color) indicates the spatial distribution of uniform lithologies. Although the exact lithology type may not be predictable on this figure, it gives an idea about where the lithofacies are uniform in the reservoir. By comparing this attribute with other attribute like instantaneous amplitude, the lithology type associated with these bandwidths may be ascertained.

Instantaneous dominant frequency is the square root of the sum of the squares of the instantaneous frequency and instantaneous bandwidth and is always positive (Barnes, 1993b). These attributes may help in interpreting gas zones in a seismic record (Barnes, 1993b) as they highlight a low frequency zones beneath a highly attenuated zone such as gas sand. Figure 45 shows a time slice exhibiting a low frequency shadow zone beneath the high amplitude sands which probably been steamed.

Response attributes:

Response attributes exhibit a blocky appearance when plotted because one value is obtained for each energy envelope lobe and is returned as a constant for the entire time interval of the envelope lobe from trough-to-trough. Response attributes for frequency, amplitude, phase and energy may be derived from the values at the envelope peak. In the presence of noise, these attributes are easier to interpret than the corresponding instantaneous ones.

Response frequency is the value of instantaneous frequency at the peak of the amplitude envelope and is a measure of the dominant frequency of the waveform contained within the envelope (Bodine, 1984). It is useful for comparison of frequency variations from energy lobe to energy lobe. This attribute may be useful for identifying shadow zones beneath gas accumulations and may be used as a porosity/permeability indicator because the lateral/vertical continuity of the shadow zone can be broadly delineated. The response phase is the dominant phase of the waveform, and useful in measuring phase variations from energy lobe to energy lobe. The response length attribute is the half the time interval of the energy envelope from energy trough to trough. It is independent of phase and amplitude (Bodine, 1984). Figure 46 shows the lateral continuity of lower frequencies on a time slice (456 ms) of response frequency. In the figure, a time slice at 456 ms of instantaneous dominant frequencies is presented for comparison. The response frequency attributes broadly delineate the lower instantaneous dominant frequencies as it only considers one representative frequency per lobe.

Apparent polarity:

Apparent polarity is the polarity of the real trace at the amplitude envelope peak weighted with the reflection strength. Polarity refers to the sign of reflection coefficient at the interface. For a normal incidence on an interface, reflection coefficient is related to densities and velocities of upper and lower mediums.

$$\mathbf{R = (\rho_2 V_2 - \rho_1 V_1) / (\rho_2 V_2 + \rho_1 V_1)}$$

where ρ_2 and ρ_1 are the densities of the lower and upper media, and V2 and V_1 are the corresponding velocities. The product of density and velocity is also called acoustic impedance.

Sheriff (1984) assigns a positive polarity to a seismic wave shape when the acoustic impedance of the lower medium is greater than that of the upper one (positive reflection coefficient). A negative polarity occurs when the acoustic impedance of the lower medium is lesser than that of the upper medium (negative reflection coefficient). Thus, the polarity at an interface is either +1 or -1 depending upon the impedance contrasts.

Levin (1986) first published the application of polarity reversal in seismic exploration. The apparent polarity is related to the variation in acoustic impedances at the interface boundary, hence its sign may tell about the elastic properties of the subsurface surrounding the interface. It may be a hydrocarbon indicator for an oil and gas zone underlying a hard trap rock where a polarity reversal (-1) is observed (Keys, 1989). Figures 47 and 48 clearly bring

out the apparent polarity contrast of the Temblor formation from Pre-Temblor and Kreyenhagen formations.

Perigram:

This attribute is obtained by subtracting a running average amplitude value from each data value in an amplitude envelope (reflection strength). The process converts the strictly positive reflection strength data into negative to positive alternating data. The resultant display makes the energy maxima more obvious in a seismic section (Gelchinsky et al., 1985). This attribute provides a broader distribution of amplitude values (ranging from negative to positive values) which may allow more precise isolation of interesting features. Like reflection strength, the perigram may provide useful information on lithology but because the perigram data contain both positive and negative values, more color contrast ranges can be assigned to the data range, which helps in interpretation. Figure 49 presents a flattened time slices showing the high amplitude sand bodies distribution within the Temblor. The high values show the discontinuities resembling sinuous channel like features and gradually shifts SE in deeper levels.

The Coalinga reservoir is clastic in nature and highly heterogeneous due to deposition of various lithofacies in different geological time periods when the basin experienced a succession of paleoenvironments ranging from incised fill to subtidal (Bridges and Castle, 2003). Localized unconformities delineate the reservoir into different petrophysical zones where reservoir properties are believed to differ. Volumes of instantaneous attribute such as instantaneous amplitude and perigram are chosen to delineate the reservoir in terms of

reflectivity as it gives information about the spatial distribution of the varied lithologies, both vertically and laterally. The instantaneous frequency, instantaneous bandwidth, dominant frequency, and response frequency isolate abrupt changes to characterize reflection zones, bedding, and lithology variation, while marking the unconformities and highlighting steam. Instantaneous phase delineates and map the unconformities as it is a good indicator of lateral discontinuities. Moreover, it is independent of seismic amplitude strength, which helps to analyze both weak and strong reflectors. It helps in mapping the unconformities in low seismic amplitude zones. In addition, geometrical attributes such as coherency were utilized to ascertain the degree of similarity between adjacent traces to check for the presence of any conspicuous depositional and structural features, for example, discontinuities such as channels and fault in the data set, which help during volume visualization and interpretation.

6.2 Geovolume Visualization and Interpretation

Seismic resolution depends on seismic wavelength. The vertical seismic resolution limit is on the order of one-fourth of the seismic wavelength. The seismic wavelength is directly proportional to velocity and inversely proportional to frequency as wavelength is the ratio between velocity and frequency (Kallweit, R. S. and Wood, L. C., 1982). In the subsurface, velocity gradually increases with depth while the frequency decreases, which increases wavelength and thus, reduces the seismic resolution for deeper horizons (Brown, 1996). The lateral resolution is related to the fresnel zone which is dependent on velocity, frequency, and the time and depth (Yilmaz, 1987). The seismic data set exhibits an estimated vertical resolution of 20m and a lateral resolution of 167m (9 CDP spacings) based on velocity (2000m/s), frequency (25 Hz), and time (0.7 s) for the Temblor reservoir.

Within the past few years, advanced computing power enable to stretch the resolution limit with the help of the new technology 'Geovolume Visualization and Interpretation (GVI)'. These techniques help to demarcate and delineate the reservoir into subunits based on seismic signature and connectivity. Various statistical techniques and stochastic modeling of reservoir rocks conditioned with well log and seismic data can subsequently be applied to stretch the resolution limit in the data to the maximum possible. The technology and philosophy of GVI differs dramatically from conventional line-based interpretation and includes new interpretation strategies and methodologies, such as 3D visualization using contrasting color scheme to distinguish various amplitudes, selective discarding the

extraneous amplitudes, and motion. It allows 3-D seismic interpreters to rapidly analyze enormous data volumes by tapping the mind's eye and by incorporating seismic attributes much earlier into the interpretation process. Kidd (1999) categorizes two basic types of visualization:

- Map-based (surface visualization)
- Volume-based (volume visualization)

Surface visualization results from mapping individual horizons and structural/sedimentological features, and then reinterpreting them collectively in 3D space as a 3D model. It is the logical product of conventional interpretation.

Volume visualization assumes that the seismic reflectivity of the subsurface represents a 3D model of the subsurface's structural, stratigraphic, and amplitude features (Kidd, 1999). The process starts with volume visualization and is followed by volume interpretation. Volume visualization is a method of seismic interpretation in which the geophysicist directly evaluates the seismic reflectivity of the subsurface in three dimensions by applying various levels of transparency to the data to quickly interpret and evaluate complex structural, stratigraphic, and amplitude features.

The four main techniques of GVI are recognition, color, motion, and isolation (Sheffield et al., 2000). Recognition of any interesting and anomalous feature helps to distinguish characteristics of features to be delineated. This is followed by assignment of proper color and

transparency schemes to represent different attribute ranges which enhance those recognized characteristics for visualization and geobody mapping (Meyer et al., 2001). Using an appropriate color scheme which clearly separates various attribute ranges with contrasting colors, the resultant image is a direct representation of the seismic attribute distribution (Kidd, 1999). Depth cueing, a process where more distant objects are rendered with a lower intensity than nearer ones, is helpful for color viewing. It selectively blends image colors with the background color which improves the perception of depth and shape for 3D objects. Motion allows observation how the seismic data are related in space and time. Moving an observer's viewpoint with respect to an interpreted horizon (distance and orientation) helps its interpretation. Projection, a process by which 3D objects are graphically displayed according to their spatial relationship on a two-dimensional plane as a surface, often help in the visualization and interpretation process (Foley, et al., 1990). Isolation, the ability to separate events of interest from others, is the last key feature of GVI. This is achieved by rendering non interesting objects transparent and creating a transitional transparency scheme for marginally important values which helps in illuminating the stratigraphic and geomorphic architecture within the reservoir (Harvey et al., 2000).

Landmark's *Earthcube* was used to render various instantaneous attribute volumes with a properly designed opacity scheme wherein the extraneous seismic attribute values are rendered transparent for visualization analysis. Figure 50 shows the architectural setting of Temblor reflectors in color for the entire study area. The basal plane portion of Figure 50 is shown with more zooming (spatial magnification) than the walls and diagonals for a better three-dimensional display. Multiple channel stack patterns are observed in both inline and

crossline at the same location (Figure 51) which implies that the channel is laterally extensive throughout the reservoir. With the help of the chosen opaqueness and color scheme for a selected range of attribute values, Figure 52 illustrates the overall stratification pattern of the reservoir (Mahapatra et al., 2004). By applying both a different set of opacity parameters and color scheme, the bed disposition in the reservoir is further analyzed. Figure 53 depicts these stratal dispositions with oblique slices in different directions. The spatial distribution of the three unconformable surfaces of the reservoir is shown in Figure 54. Figures 52, 53, and 54 clearly extract and display geological information, like bedding plane architecture, showing layers of different amplitudes (lithologies) and unconformity surface from the seismic data set which would not have been observable on traditional seismic sections.

Looking at the reservoir in a NE-view, two prominent channel-like systems (Ch-1 and Ch-2) are observed in Figure 55, Ch-2 on the right (eastern) side of the figure and Ch-1 in the left (western) part of the reservoir (Mahapatra et al., 2004). The right channel Ch-2 seems to be both laterally and vertically extensive with a gradual shift towards ESE-SE. The left channel Ch-1 originates at a deeper level than Ch-2, and shifts towards SSE with depth. It does not appear to extend deeper in the volume. However in the present NE-view, a portion of Ch-1 is observed towards lower left side. Figures 56 and 57 show cubes of instantaneous amplitude (reflection strength) which depict the lithofacies distribution pattern of the reservoir. Figure 58 shows the chosen transparency scheme versus amplitudes for the display in Figure 57. Note that these attribute volumes depict two distinct distributions of seismo-lithofacies within the field based on elevated values of the reflection strength attribute. The more prominent and vertically more extensive one is at the top. The lithology associated with

the channel deposits (yellow bodies in Figures 55, 56, and 57) are likely sands as evidenced by the bright reflection strength indicating hydrocarbons and/or steam. Their extent suggests connected porosity with larger permeability.

The top group of seismic facies is observed to contain the zones C and B of the reservoir (Figure 24 and 56) implying different facies characteristics than the underlying strata. The formations of the top seismic lithofacies group may be attributed to the presence of the Buttonbed and Valv unconformities (Figure 57). The bottom group (lower part of zone A in Figure 24) represents the incised valley fill deposition over the Base Temblor unconformity. The absence of any prominent seismic facies between 550-650 ms in Figure 57 (towards the southern part), sandwiched between the top and bottom groups, seems to represent the estuarine deposits with less or no significant reservoir. The absence of prominent estuarine reservoir rocks in the Coalinga area is evidenced on outcrop, core, and wireline log analysis performed by Bridges and Castle (2003). They observed that the estuarine deposit is mainly composed of intercalations of claystone, siltstone, and fine grained sandstone which do not constitute significant reservoir rocks.

Careful GVI helped in segmenting the study area into channel and non-channel bearing volumes. Further, the entire volume was subdivided into subunits based on the position of these three unconformities in the Temblor Formation.

These high amplitude sand bodies were further analyzed on wireline logs to confirm its lithology and on seismic volumes to demonstrate its spatial distribution over the study area which will be discussed in the following chapter.

Chapter 7

Characteristics of High Amplitude Sands

To ascertain the lithology of these bodies, the wireline logs in the study area were examined. These high reflection strengths (instantaneous amplitudes) are collocated with a high-gamma sand as observed in a trace slice of the Figure 55 (Figures 59) with gamma counts going up to 220 API units and with a compensated neutron porosity of 0.35 to 0.44. On an instantaneous amplitude section in the dip direction (Figure 60; Mahapatra, et al., 2005), these sands are clearly observed. The high-gamma sand occurs on the top of a sand sequence with a gradational contact. On wireline logs, the average thickness of these high-gamma sands is about 160 feet. Occasionally, few hard streaks and calcareous sands are observed in the bottom of this sand. Three upward coarsening high-gamma stacks are observed in the wireline logs based on their upward decrease of gamma counts in the sand matrix (Figure 61). Occurrence of high-gamma sand below diatomite (below Buttonbed) is also observed in cores of the Temblor (Piver, 2004; Bridges and Castle, 2003). The high-gamma count in the sands may be due to the matrix presence of phosphate (Piver, 2004; Bridges and Castle, 2003), glauconite, heavy minerals, and biotite in analogy to the Monterey Formation of Pru Fee reservoir of Midway-Sunset field in southern part of the San Joaquin basin (Schamel, 1999). The heavy oil reservoir of the Pru Fee field is in the Upper Miocene Monarch sand of the

Monterey Formation (Gregory, 1996). The reservoir rocks of the Pru Fee are high-gamma sands with good porosity (Schamel, 1999).

The time slices of instantaneous amplitude, perigram, coherency, instantaneous dominant frequency, response frequency, and instantaneous bandwidth suggest the presence of two channels in the reservoir. The instantaneous amplitude (reflection strength) slices (Figure 55) show high amplitudes against these channel shapes. As discussed earlier, these high amplitudes correspond to sands (Figure 60). The perigram slice also shows the presence of high values against these bodies. The flattened instantaneous amplitude volume shows sinuous features (Figure 62) and these features along with the earlier observations from various seismic attributes support the presence of channel in the reservoir. The reflector continuity confidence maps (Figure 25) show the presence of discontinuities on top of the Base Temblor, Buttonbed, Valv and Top Temblor surfaces which may be due to the statics caused by these sands. The isochron maps between these unconformable surfaces (Figures 33 to 37) show thickening lobes in the southeastern side of the area where many seismic attributes are discontinuous.

Figure 55 demonstrated objects or branches with channel shape. The oblique slices through the reflection strength cubes (Figure 55) and vertical slices (Figures 59 and 60) depict the presence and spatial distribution of two channel-shape geometries. The time slices through the flattened instantaneous amplitude attribute volume show two distinct channels (Figure 62). Figure 63 of regular time slices in the Temblor Formation show the lateral and vertical extents of the high-amplitude sands in the reservoir. The channel on the left side (Ch-2) is shifting

towards ESE-SE with increasing depth as observed earlier on Figure 55. Also, the bottom channel Ch-1 is shifting towards SSE with depth as observed earlier on Figure 55. Ch-2 originating from the southwestern corner of the area below the Top Temblor gradually shifts ESE-SE with depth, runs nearly parallel to the Top Temblor unconformity up to central part of the area, cuts across the Valv unconformity, creates a channel-like incision, and follows the Buttonbed unconformity (Figure 64). At the Buttonbed surface, multiple high-amplitude layers are observed in Figures 28, 26b, 51, and 63 suggesting recut and stacked deposits. Ch-1 lies between the Base Temblor and the Buttonbed. It is prominently present both in the southwestern and northwestern parts but conspicuously scattered or absent in the western-central part.

It is interesting to note that the area with difficulties for mapping the seismic reflectors (Figure 22) and mismatches of the lines and traces located between the northern and southern parts of the study area corresponds to the subsurface location of the shallower Ch-2 sand bodies (Figure 65). The difficulties and mismatches observed by the author and others may be caused by statics resulting from these sand bodies partially filled with steam.

The high-gamma bodies show stacked coarsening upward sequences (Figure 61). The depositional environment contributing to stacked coarsening upward sequences may be stacked delta front lobes, prodelta fans, submarine fans, prograding shoreline facies, or stacked shoreline facies, etc. The geometries and extensions of these sands (lying near parallel to the Base Temblor, the Top Temblor, and the paleoshore line during the Temblor) may be suggestive of littoral type deposits. The incision of Ch-2 in the central part of the area may be due to a change

in wave action, a submarine channel, or may be a runoff channel. Further researches in the regional scale may confirm the depositional environment for these sands.

The log motif nature of the high-gamma sands appears nearly similar to the high-gamma producing sands of the Monterey Formation of Pru Fee heavy oil reservoir of Midway-Sunset field in southern part of the San Joaquin basin. The Monarch sand of the Monterey Formation is stratigraphically equivalent to the Santa Margarita Formation (Schamel, 2002) and in the Coalinga field, the Santa Margarita Formation overlies the Temblor Formation towards the north of the Coalinga area (Bridges and Castle, 2003; Clark, et al., 2001a). Bridges and Castle (2003) observed that the diatomite tract between BS4 and BS5 (on the top of Buttonbed) might be stratigraphically equivalent to a portion of the Monterey Formation.

Nilsen (1996) identified the Monarch sands as a deep submarine channel or proximal fan deposit. Webb (1978) described the Monarch sand as a coarsening upward sequence generated by a prograding fan. The high gamma Monarch sands within the Monterey Formation of Pru Fee field are described as a progradational turbidite sequence based on a detailed core analysis of the well Pru 101 which was cored entirely, and outcrop analysis (Schamel, 1999). The wireline log shows high-gamma values against the diatomaceous mudstone and pebbly sands of the Monarch sands. The overall lithological characteristics of the Monarch sands are related to proximal turbidites (Schamel, 1999). Schamel interprets the sand sequence as progradational turbidite sequences based on geological guidelines for turbidite identification (Walker, 1981). Schamel, et al. (2002) described the sand as a steep-faced fan delta prograding onto a shallow marine shelf

with periodic remobilization of debris flows which generated turbidity currents and flowed downslope to deposit the Monarch sands.

Isolated highstand shelf sands of turbiditic origin are reported in different geological setting, such as, in the Miocene-Lower Pliocene, Great Bahama Bank (Betzler, et al., 1999) and in the Cretaceous Western Interior, Book Cliffs, Utah (Pattison, 2005). Turbidites were reported as shelf deposits in the Miocene deltaic cycles exposed along the Jerudong Anticline, Brunei Darussalam (Back, et al., 2001). They suggested that the shelf turbidite might have formed in the delta front as a result of a relative fall of sea level. The delta front over steepens, fails, and generates shallow-water slumps. Mobilized sediments (slumps and turbidites) accumulate within the prodelta succession.

The stacked high-gamma sand deposit of the Temblor may be the result of successive periods of high energy depositional cycles with storms and waves. Bridges and Castle (2003) observed that the subtidal environment of the Temblor (between the Buttonbed and Valv) might be due to a complex combination of storm, wave, and tidal processes. In between the Buttonbed and Valv, a coarsening upward sequence in a prograding environment was reported by Bridges and Castle (2003). They observed that the basin was deeper, wave processes were stronger in the southern part of the Coalinga area (the present study area), and the diatomite was not present. Reworked sediments consisting of interclasts, broken shells, glauconite, and phosphate grains are observed in the tide- to wave-dominated sequences in the Temblor were reported below the Buttonbed suggesting a high energy environment (Bridges and Castle, 2003). In view of the above analogy to the Monarch Sand of the Monterey Formation and high energy regimes

prevailing intermittently within the Temblor Formation, occurrences of proximal fans or prograding shoreline turbiditic deposits within the Temblor may be a possibility. However, the differential tectonic effect experienced by both the present area and the Pru Fee reservoir (towards the south of the San Joaquin basin) might have played a significant role in influencing the depositional environments. In addition, there is no direct sedimentological evidence (core analysis) is reported in the deeper southern part of the Coalinga (present study area) area to substantiate the exact depositional environment for these sand bodies.

A detailed regional seismic and geological analysis should be performed to confirm the origin and regional geometry of the distribution of these high-amplitude sands within the Temblor of Coalinga.

Chapter 8

Discussion

Reservoir characterization and model building are necessary steps to develop an oil field (Mahapatra et al., 2003a). It combines stratigraphic analyses with the detection of paleogeomorphic features, and integrates geologic and seismic data. Identification of major sedimentological depositional structures along with nondepositional features greatly helps the petrophysical delineation of the reservoir. The lateral continuity of different reservoir units is better characterized on seismic data than on well data because 3D high-resolution seismic data provide information without gaps over long scales. The resulting reservoir model is based on lithological parameters estimated from well cuttings, core, and wireline logs. The lithologic and petrophysical gaps between the wells are filled by interpolation or geostatistics. In either case, the final realizations of key petrophysical parameters are not always accurate and may differ from the real reservoir.

The objective of the present investigation was to analyze 3D seismic data of the highly heterogeneous clastic Coalinga reservoir to map various seismostratigraphic sequences and geobody elements, which in turn help to identify, delineate, and demarcate the various reservoir subunits based on their depositional signatures and geological characteristics.

The reservoir in the Temblor Formation represents the interplay of shallow marine and non-marine depositional environments (Bate, 1984; Bate, 1985; Clark et al., 2001b). The clastic shallow, unconsolidated reservoir is very heterogeneous in nature, as it is mostly bounded by unconformities and subdivided into three distinct depositional environments representing a near-shore fluvial dynamic depositional setting interspersed by with depositional erosional hiatuses. The four unconformities (Base Temblor, Buttonbed, Valv, and Top Temblor in ascending order) within the reservoir play significant roles in the distribution and flow of fluids in the reservoir (Clark et al., 2001b). The Base Temblor unconformity separates the underlying Kreyenhagen shales from the Temblor and represents an incised valley-estuarine fill-up setting. The overlying Buttonbed unconformity represents the transition to tide and wave dominated shoreline facies, which in turn is capped by the Valv unconformity representing a sub-tidal dominated facies. The Top Temblor unconformity separates the Temblor from the overlying Santa Margarita formation (Bridges and Castle, 2003). The thicknesses between the three facies tracts within the Temblor Formation vary over the field due to the presence of dynamic paleotopography of the basin caused by varying degrees of tectonic uplift and differential amounts of sedimentation throughout the period of deposition and erosion (Bartow, 1991). All but the bounding surfaces BS-2 and BS-4 of Bridges and Castle (2003) can be mapped on seismic data, while BS-2 and BS-4 can only be identified on wireline logs and outcrops.

The seismic characters of these unconformable surfaces are subtle in nature and are easily overlooked in the field area without prior stratigraphic knowledge based on cores and

outcrops (Clark et al., 2001b). Integration of continuous 3D seismic data with the geological data was carried out to verify, analyze, and map the spatial distribution of these unconformities in the reservoir for a meaningful reservoir characterization. In the present analysis, paleogeomorphic and depositional features on the seismic data were sought for. These features are the preserved resultants of the various tectonic forces that acted on this complex strike-slip reservoir in the geologic past.

The 3D seismic data are a merged poststack volume from different seismic datasets, acquired between 1996 and 2000. The seismic surveys were carried out over the field while steam was being injected intermittently and the reservoir was depleting due to simultaneous production (Clark et al., 2001b), which affected the velocities, amplitudes, and reflections. Analysis on core sample suggested a decrease in P-wave velocity (V_P) by about 1% for every 19^0 Fahrenheit increase in reservoir temperature, by 8% with the presence of steam, and by 25% by the combined effect of steam and increased temperature (Lumley, et al., 2001). The presence of varying proportion of steam in the reservoir causes seismic wave distortions and velocity pull down effects in different blocks of the reservoir. An analysis was performed to estimate the effect of steam on the P-wave velocity (V_P) and on the reflection coefficient values between fluid, gas, and steam saturated sand and clay. The estimates are based on reported experimental and analytical values of elastic moduli, density, V_P, or S-wave velocity (V_S) (Gassmann, 1951; Mavko, et al., 1998; Wang, 2001; Han and Batzle, 2004). The analysis estimate that V_P for steam saturated sand may decrease by 27% compared to oil saturated sand (Table 2). This theoretical finding is consistent with the result of Lumey, et al. (2001) on the reservoir rocks. The largest reflection coefficient is observed for clay over

steam/gas saturated layers. Amplitude variability resulting from steam injection (Ecker, et al., 1999) makes time-depth correlation difficult and the ties between data and well logs become problematic and vexing (Mahapatra et al., 2003b). The identification of sequence stratigraphic elements like offlap, onlap, and truncation analyses on seismic data becomes perplexing due to the discontinuous nature of the reflector pattern and the associated dipping events. Finally, the merging of seismic data acquired at different times causes misties between inlines and crosslines, and yields reflector discontinuities resembling faults. Each dataset was acquired after injection of varying amounts of steam into the reservoir, with varying sources, signal-to-noise levels, and independent static corrections. Significant static breaks were observed due to a decrease of the interval velocity which may be due to an excessive amount of steam that was placed into this section (William Kempner, 2003, personal communication). In addition, there is a significant static time shift and frequency change observed at the boundary between sections 24D and 25D due to steam effect. A similar change is also observed between sections 25D and 36D.

For seismostratigraphic analysis of the reservoir, density and sonic wireline logs were correlated. Four unconformable surfaces (Base Temblor, Buttonbed, Valv, and Top Temblor) within the Temblor reservoir were identified based on the shale base trend line shifting. While trying to map these surfaces on the seismic data, severe misties and reflector discontinuities on the seismic sections were observed due to data merge and steam effects (Mahapatra et al., 2003b). The reflectors in the central part of the study area are more discontinuous in nature due either the presence of inherent reservoir heterogeneities, and/or steam effects. Many problems were encountered in closing reflector loops as forced closing of loops at some places contradicts

geological expectations. Confidence maps of reliability of seismic loop tying the reflectors shows poor reflector continuities in the Base Temblor, Buttonbed, and Valv unconformities due to presence of channel like discontinuities.

A deeper, relatively continuous reflector within the Kreyenhagen formation was mapped and flattened (Mahapatra et al., 2003b). As the two-way time for the deeper layer is made constant by flattening, the misties in the overburden are reduced considerably on this flattened volume and the continuity of the four unconformities within the reservoir is improved (Figures 23a and 23b). The flattened volume with appropriately time-shifted wireline data allowed better identification and interpretation of the unconformities in the originally discontinuous seismic volume. Sequence stratigraphic elements such as offlap, onlap, and reflector truncation were identified on seismic data which allowed mapping of unconformities. High-order sequence boundaries were identified, and it was confirmed that the reservoir is compartmentalized into three major vertical chronostratigraphic sequences (Mahapatra et al., 2004). The analysis of reflector trends and chronostratigraphic sequences enabled to ascertain geological features such as the strike and variation of depositional direction of the reservoir rocks. The strike of the Temblor formation is observed to be NNE-SSW. The highest structural relief is towards the western part of the study area. The zone between the Buttonbed and Basal Temblor surfaces contains a multitude of channel cuts. In the lower central part of the study area, these channels appear to be recut and restacked. The thicknesses of the unconformity bounded zones between the Top Temblor, Valv, and for the entire Temblor formation are increasing downdip towards east and are at maximum in the northeastern corner of the area, except between the Base Temblor and Buttonbed unconformities where the maximum thickness is observed in the eastern central part of the area

probably due to the presence of less compactable sands in the channel like features decreases the P-wave velocity.

Instantaneous and volume based seismic attributes were utilized to study the clastic reservoir. These attributes identified discontinuities within the reservoir and helped mapping of the reflectors in the stratigraphic analysis as well as in the seismogeomorphic interpretation and sand-body delineation. Geovolume Visualization and Interpretation (GVI) techniques (Sheffield and Tatum, 2000; Kidd, 1999) were applied on the seismic data set to demarcate and delineate the reservoir into subunits based on stratigraphic and geomorphic architectures. The GVI analyses revealed two prominent channel systems (Ch-1 and Ch-2) within the reservoir which are recut and restacked at places (Mahapatra et al., 2004). The channel Ch-2 seems to be both laterally and vertically extensive with a gradual shift towards ESE-SE. The channel Ch-1 originates at a deeper level than Ch-2 in the northwestern part of the area, and gradually shifts towards SSE and does not appear to extend deeper into the volume. A number of sedimentological features like bed stratification and lithofacies distribution patterns are clearly observed by GVI. It is interesting to note that these attribute volumes show two distinctive distributions of reservoir rocks over the field based on higher values of the reflection strength attribute. The top group of seismic facies has different lithofacies characteristics than the underlying section as it is populated with large reflection strengths. The occurrence of the top group seismic lithofacies (zones B and C in Figure 24) may be attributed to the presence of the Buttonbed and Valv unconformities. The bottom group coincides the incised valley fill deposition over the Base Temblor unconformity. The major lithofacies associated with the channel deposits may be porous sands evidenced by the bright reflection strength indicating

hydrocarbons and/or steam. Their extent suggests connected porosity with larger permeability. The area between the top and bottom clusters devoid with reflection strength may represent the estuarine deposits which lack reservoir facies. The absence of prominent estuarine reservoir rocks in the Coalinga area is evidenced on outcrop, core, and wireline log analysis performed by Bridges and Castle (2003). They observed that the estuarine deposit is mainly composed of intercalations of claystone, siltstone, and fine grained sandstone which do not constitute significant reservoir rocks.

The high instantaneous amplitudes are collocated with high-gamma sand observed in the wireline logs. The high-gamma sands occur at the top of the sand sequence with a gradational contact. The high-gamma sand is about 160 feet thick with good porosity (.35 to .44). Three upward coarsening high-gamma stacks are observed within the sand. The occurrence of high-gamma sand below diatomite (below Buttonbed) is also observed in cores (Bridges and Castle, 2003) and in the Monarch sands of Pru Fee reservoir in the Monterey formation in the southern San Joaquin basin. The high-gamma count in the sands may be due to the matrix presence of phosphate (Piver, 2004; Bridges and Castle, 2003), glauconite, heavy minerals, and biotite in analogy to the Monterey Formation (Schamel, 1999).

The seismic attribute analyses clearly demonstrate the presence of two discontinuities similar to channel shape. The seismogeomorphological analysis also depicts two channel features. The flattened instantaneous amplitude slices confirm the presence of sinuous features which corroborate to the observations by seismic attribute analysis where in channel shape discontinuities were observed. The reflector continuity confidence map shows discontinuities

which may be due to both the channel configuration and statics associated with the sands and their pore fill in channels. The isochron maps shows thickening lobes towards the eastern side where these channels located.

The two channels, Ch-1 and Ch-2 were further delineated with the help of instantaneous amplitude time slices. The deeper channel Ch-1, lying in between the Base Temblor and the Buttonbed, is present both in the southwestern and northwestern parts but is scattered or absent in the western-central part. It shifts towards SSE with depth. The shallower channel Ch-2 originating from the southwestern corner of the area below the Top Temblor gradually shifts ESE-SE with depth, runs nearly parallel to it up to the central part of the area where it cuts across the Valv unconformity, creates a channel incision with multiple high amplitude layering, and follows the Buttonbed unconformity up to the northern end of the area.

The difficulties faced by the author and others in mapping seismic reflectors mapping and mismatches of the lines and traces in the central part of the study area are attributed to the statics generated by the shallower sand Ch-2 running nearly north-south beneath the Top Temblor (Figure 65).

The depositional environment of these stacked high-gamma sand bodies seems to be prograding shoreline facies, delta front lobes, submarine facies, or stacked proximal turbidites with high volumes of sediment supply but little accommodation space as a result of successive high energy depositional cycles caused by storms and waves. A prograding shoreline environment with upward coarsening was reported by Bridges and Castle (2003). They reported

sediment reworking below the Buttonbed suggestive of a high energy environment and that the southern area (study area) experienced stronger wave process relative to tidal process than the northern area. Bridges and Castle (2003) reported brackish water and very shallow marine depositional setting for the diatomite facies tract above the Buttonbed based on analysis of the burrow patterns in claystone beds and occurrence of foraminifer (Quinqueloculina sp.). They also observed that the diatomite was absent towards the southern part (study area) which may imply deeper water in the study area. The subtidal environment (between the Valv and the Top Temblor unconformities) also experienced effects of storms and wave processes (Bridges and Castle, 2003). The geometries and extensions of these sands (lying near parallel to the Base Temblor, the Top Temblor, and the paleoshoreline during the Temblor) may suggest littoral type deposits. The incision of Ch-2 in the central part of the area may be due to a change in wave action, a submarine channel, or may be a runoff channel.

The stacked high-gamma sequence of the Temblor is similar to the heavy oil producing high-gamma Monarch sands in the Monterey formation of the Pru Fee reservoir on wireline logs. Schamel (2002) reported three high-gamma oil bearing sand stacks. The stratigraphic setup of the Upper Miocene Monarch high-gamma sands is similar to the Temblor of northern Coalinga as both are partially overlain by the Santa Margarita formation. Bridges and Castle (2003) observed that the diatomite tract on top of the Buttonbed might be stratigraphically equivalent to a portion of the Monterey formation.

Schamel (2002) described the high-gamma sequence of the Pru Fee in the Monarch sands as prograding turbidite sequences based on cores and outcrop analyses. The overall lithological

characteristics of the Monarch sands are related to proximal turbidites (Schamel, 1999). Nilsen (1996) identified the Monarch sands as a deep submarine channel or proximal fan deposit. The coarsening upward sequence of the Monarch sands was also attributed to a prograding fan (Webb, 1978). Instances of turbiditic origin are also reported in highstand regime (Pattison, 2005; Betzler, et al., 1999). Turbidites with shelf origin were reported in the Miocene deltaic cycles along Jerudong Anticline, Brunei Darussalam (Back, et al., 2001). A prograding proximal turbiditic, delta front lobes or prograding shoreline facies origin of the high-gamma sands in the study area may be inferred based on the stronger wave action, deeper water, and analogy to the Monarch sands. However, the depositional environment of the high-gamma sequences of both the present study area and that of the Pru Fee reservoir in the Monarch sands in the southern part of the San Joaquin basin might have been differentially influenced by tectonics. In addition, there is no direct sedimentological evidence available for the present analysis to ascertain the appropriate depositional environment for these sand bodies in the study area.

A detailed regional analysis of the San Joaquin basin by integrating all available seismic lines, well data, and outcrop analysis should be performed to improve the understanding of the stratigraphic relationship, environment of deposition, and distribution of these sand bodies.

The present investigation helped in segmenting the study area into channel and non-channel bearing volumes. Furthermore, the entire reservoir volume was also subdivided into subunits based on the position of these unconformities in the Temblor Formation. These subunits could be used for further stochastic modeling of the reservoir to improve the steam injection and placement of infill wells for optimizing the current tertiary crude oil production cycle. In

addition, seismic attribute to petrophysical parameter transforms based on multivariate regression or neural networks would be aided by this segmentation because a different transform could be defined for each unit. Further investigation into the physical and mathematical relationships between seismic attributes and wireline log parameters would clarify identification of seismic facies, channel forms, and lithology. Lastly, the merged data sets caused severe problems including misties, discontinuities, and changing wavelets. These problems would at least be reduced partially by reprocessing all data together in a consistent manner, although the effects of production and steam injection on the seismic data acquired in different years will remain an inherent problem.

References

Addicott, W. O., 1970, Tertiary paleoclimatic trends in the San Joaquin basin, California: U. S. Geological Survey Professional Paper 644-D, 19 p.

Arnold, R., and Anderson, R., 1910, Geology and Oil Resources of the Coalinga District: U. S. Geological Survey Bulletin 398, 354 p.

Atwater T., 1970, Implications for plate tectonics for the Cenozoic tectonic evolution of western North America: Geological Society of American Bulletin, 81, pp. 3513–3535

Back Stefan, Morley Christopher K., Simmons Michael D., and Lambiase Joseph J., 2001, Depositional environment and sequence stratigraphy of Miocene Deltaic Cycles exposed along The Jerudong Anticline, Brunei Darussalam, Journal of Sedimentary Research, v. 71, No. 6, pp. 913-921.

Bahorich, M., and Farmer, S., 1995, The coherency cube: The Leading Edge, v. 14, pp. 1053-1058.

Bailey, E. H., Irwin, W. P., and Jones, D. L., 1964, Franciscan and related rocks, and their significance in the geology of western California: California Division of Mines and Geology Bulletin 183, 177 p.

Bandy, O. L., and Arnal, R. E., 1969, Middle Tertiary basin development, San Joaquin Valley, California: Geological Society of America Bulletin, v. 80, pp. 783-819.

Barnes, A. E., 2001, Seismic attributes in your facies, CSEG Recorder, pp. 41-47.

Barnes, A. E., 1991, Instantaneous frequency and amplitude at the envelope peak of a constant-phase wavelet: Geophysics, 56, pp.1058-1060.

Barnes, A. E., 1993a, When the concepts of spectral frequency and instantaneous frequency converge, The Leading Edge, 12**,** no. 10, 1020-1023.

Barnes, A. E., 1993b, Instantaneous spectral bandwidth and dominant frequency with application to seismic reflection data: Geophysics, 58, pp. 419-428.

Bartow, J. A., 1991, The Cenozoic evolution of the San Joaquin Valley, California, U. S. Geological Professional Paper 1501, pp. 1-40.

Bartow, J. A., 1985, Map and cross sections showing Tertiary stratigraphy and structure of the northern San Joaquin Valley, California: U. S. Geological Survey Miscellaneous Field Studies Map MF-1761, scale 1:250,000.

Bate, Matthew Adam, 1985, Depositional sequence of Temblor and Big Blue formations, Coalinga anticline, California *in* Graham, S. A., ed., Geology of the Temblor Formation, Western San Joaquin Basin, California: Society of Economic Paleontologists and Mineralogists, Pacific Section-American Association of Petroleum Geologists, pp. 69-86.

Bate, Matthew, Adam, 1984, Temblor and Big Blue formations: interpretation of depositional environment sequence on Coalinga anticline, Fresno County, California, Master Thesis, Stanford University.

Betzler Christian , Reijmer, John J. G., Bernetà, Karin, Eberlià, Gregor P., and Anselmetti, Flavio S., 1999, Sedimentary patterns and geometries of the Bahamian outer carbonate ramp (Miocene-Lower Pliocene, Great Bahama Bank), Sedimentology, 46, pp. 1127-1143.

Beyer, L. A., 1995, Web Page URL: http://certnetra.cr.usgs.gov/1995OGData/Region2/PROV10.pdf

Blake, M. C. et al. 1978, Neogene basin formation in relation to plate-tectonic evolution of the San Andreas fault system, California: American Association of Petroleum Geologists Bulletin, v. 62, pp. 344-372.

Bloch, R. G., 1991, Studies of the stratigraphy and structure of the San Joaquin basin, California, Ph. D. dissertation, Stanford University, Palo Alto, California.

Bloch, R. G., Graham, S. A., 1991, West Coast Regional Cross Section, American Association of Petroleum Geologists, Tulsa, Oklahoma, 3 sheets.

Bodine, J.H., 1984, Waveform analysis with seismic attributes. Oil & Gas Journal, 84, 24, pp. 59-63.

Bohannon, R. G., and Howell, D. G., 1982, Kinematic evolution of the junction of the San Andreas, Garlock, and Big Pine faults, California: Geology, v. 10, pp. 358-363.

Bridges, Robert, A., 2002, Local and regional tectonic control on sedimentology and stratigraphy in a strike-slip basin: Miocene Temblor Formation of the Coalinga area, California, U.S.A., Masters Thesis, Clemson University.

Bridges, Robert, A., and Castle, James, W., 2003, Local and regional tectonic control on sedimentology and stratigraphy in a strike-slip basin: Miocene Temblor formation of the Coalinga area, California, U.S.A., Sedimentary Geology, 158, pp. 271-297.

Brown, A. R., 1996, Interpretation of Three-Dimensional Seismic Data Tulsa, The American Association of Petroleum Geologists Memoir 42.

Bulloch, E. Terra, et al, 2001, Examination of a turbidite system using 3-D visualization and multiple seismic attributes, Albacora Field, deepwater brazil, expanded abstract, Ann. International Mtg., SEG, Texas.

Butler, D. B. and Knight, R. J., 1995, The effect of steam quality on the electrical behavior of steam-flooded sands: A laboratory study, Geophysics, v. 60, no. 4, pp. 998-1006.

Cady, J. W., 1975, Magnetic and gravity anomalies in the Great Valley and western Sierra Nevada metamorphic belt, California: Geological Society of America Special Paper 168, 56 p.

Casey, T. A. L., Dickinson, W. R., 1976, Sedimentary serpentinite of the Miocene Big Blue Formation near Cantua Creek, California, *in* Fritsche, A. E., Best, H. T., and Wornardt, W. W., eds., The Neogene Symposium, Society of Economic Paleontologists and Mineralogists, Pacific Section, San Francisco, pp. 65-74.

Clark, M. S., Wildman, N. A., and Blount, W. J., 2001a, Temblor Field Trip, San Joaquin Business Unit, Coalinga Field, Chevron western basins Group, pp. 1-30.

Clark, M. S., Klonsky, L. F., and Tucker, K. E., 2001b, Geological study and multiple 3-D surveys give clues to complex reservoir architecture of giant Coalinga oil field, San Joaquin Valley, California, The Leading Edge, v. 20, issue 7, pp. 744-751.

Clark, M. S., Tucker, K. E., and Kempner, W., 2000, Sequence stratigraphy and trapping mechanisms, Miocene Temblor Formation, Coalinga Field, California, (abstract for both oral and poster presentations): American Association of Petroleum Geologist Bulletin 84, p. 863.

Clark, J. C., Brabb, E. E., Greene, H. G., and Ross, D. C., 1984, Geology of Point Reyes Peninsula and implications for San Gregorio fault history, *in* Crouch, J. K., and Bachman, S. B., eds., Tectonics and sedimentation along the California margin: Society of Economic Paleontologists and Mineralogists, Pacific Section, Annual Meeting, 1984, San Diego, California, pp. 67-86.

Cross, T. A., and Pilger, R. H., Jr., 1978, Constraints on absolute motion and plate interaction: American Journal of Sciences, v. 278, pp. 865-902.

Crowell, J. C., 1987, Late Cenozoic basins of onshore southern California: complexity is the hallmark of their tectonic history, *in* Ernst, W. G., and Ingersoll, R. V., eds., Cenozoic basin development of coastal California (Rubey volume 6): Englewood Cliffs, N. J., Prentice Hall, pp. 207-241.

Coffeen, J. A., 1990, Seismic on screen, an introduction to interactive interpretation, PennWell, Oklahoma.

Cohen, L. 1995, Time-Frequency Analysis: Prentice-Hall Signal Processing Series

Current, C. L., 2001, Characterization of geologic controls on permeability and their incorporation into a three dimensional geologic model of the Temblor Formation, Coalinga, California: M. S. thesis, Clemson University, Clemson.

Davis, T. L., 1983, Late Cenozoic structure and tectonic history of the western "Big Bend" of the San Andreas fault and adjacent San Emigdio Mountains: Santa Barbara, University of California, Ph. D. thesis, 580 p.

Dickinson, W. R., Ingersoll, R. V., and Graham, S. A., 1979, Paleogene sediment dispersal and paleotectonics in northern California: Geological Society of America Bulletin, pt. 2, v. 90, pp. 1458-1528.

DOE report, 2005, Basin oriented strategies for CO_2 enhanced oil recovery: California, prepared by Advance Resources International, Inc., p. 60. URL:http://www.fe.doe.gov/programs/oilgas/publications/eor_co2/California_CO2-EOR_Report_web.pdf

Ecker, C., Lumley, D., Tura, A., Kempner, W., and Klonsky, L., 1999, Estimating Separate Steam Thickness and Temperature maps from 4D seismic data: An Example from San Joaquin Valley, California, Expanded abstract, 69th SEG Ann. Intl. Convention, Houston, Texas, USA.

Engebretson, D. C., Cox, Allan, and Gordon, R. G., 1985, Relative motions between oceanic and continental plates in the Pacific basin: Geological Society of America Special Paper 206, 59 p.

Foley, J., Van Dam, A., Feiner, S., and Hughes, J.,1990. Computer Graphics Principles and Practice: Addison-Wesley, 2 edition.

Foss, C. D., 1972, A preliminary sketch of the San Joaquin Valley stratigraphic framework, *in* Rennie, E. W., ed., Geology and oilfields-west side central San Joaquin Valley: American Association of Petroleum Geologists-Society of Economic Paleontologists and Mineralogists-Society of Exploration Geophysicists, Pacific Sections, 1972 Guidebook, pp. 40-50.

Frakes, L. A., 1979, Climates throughout geologic time: Amsterdam, Elsevier, 310 p.

Furlong, K. P. and Schwartz, Y. S., 2004, Influence of the Mendocino Triple Junction on the tectonics of coastal California: Annual Review Earth Planetary Sciences, 32, pp. 403–433.

Gassmann, F., 1951, U¨ ber die elastizita¨ t poro¨ ser medien:Vierteljahrsschrift der Naturforschenden Gesellschaft in Zurich, 96, pp. 1–23.

Gelchinsky, B., Landa, E., and Shtivelman, V., 1985, Algorithms of phase and group correlation: Geophysics, v. 50, pp. 596-608.

Graham, S. A. and Dickinson, W. R., 1978, Evidence for 115 kilometers of right slip on the San Gregorio-Hosgri fault trend: Science, v. 199, pp. 179-181.

Graham, S. A. Williams, L. A., Bate, M. A., and Weber, L. S., 1982, Stratigraphic and depositional framework of the Monterey Formation and associated coarse clastics of the central San Joaquin basin, in Williams, L. A., and Graham, S. A., eds., Monterey Formation and associated coarse clastics rocks, central San Joaquin basin, California: Society of Economic Paleontologists and Mineralogists, Pacific Section, Fall 1982 Field Trip Coalinga, Calif., Guidebook, pp. 3-16.

Graham, S. A., ed., 1985, in Geology of the Temblor Formation, western San Joaquin Basin, California: Society of Economic Paleontologists and Mineralogists, Pacific Section, v. 44, p. 202.

Gregory, G. J., 1996, Geology of the Midway-Sunset oil field, in T. H. Nilsen, A. S. Wylie Jr., and G. J. Gregory, eds., Geology of the Midway-Sunset oil field, AAPG Field Trip Guidebook, pp. 55-88.

Hackel, Otto, 1966, Summary of the geology of the Great Valley, *in* Bailey, E. H., ed., Geology of Northern California: California Division of Mines and Geology Bulletin 190, pp. 217-238.

Han De-hua and Batzle Michael, L., 2004, Gassmann's equation and fluid-saturation effects on seismic velocities, Geophysics, v. 69, No. 2, pp. 398-405.

Haq, B. U., Hardenbol, J., and Vail, P. R., 1987, The new chronostratigraphic basis of Cenozoic and Mesozoic sea level cycles, *in* Ross, C. A., and Haman, D., eds., Timing and depositional history eustatic sequences: constraints on seismic stratigraphy: Cushman Foundation for Foraminiferal Research, Special Publication 24, pp. 7-13.

Harding, T. P., 1976, Tectonic significance and hydrocarbon trapping consequences of sequential folding synchronous with San Andreas faulting, San Joaquin Valley, California: American Association of Petroleum Geologists Bulletin, v. 60, pp. 356-378.

Harvey, E. A. L., et al, 2000, Techniques for volume interpretation of seismic attributes, 68th Ann. Internat. Mtg. Expanded abstract, SEG Calgary.

Hoffman, R. D., 1964, Geology of the northern San Joaquin: San Joaquin Geological Society Selected Papers, v. 2, pp. 30-45.

Hoots, H. W., Bear, T. L., and Bear, T. L., and Kleinpell, W. D., 1954, Geological summary of the San Joaquin Valley, California, *in* Jahns, R. H., ed., Geology of the southern California: California Division of Mines and Geology Bulletin 170, pp. 113-129.

Howell, D. G., Crouch, K. K., Greene, H. G., McCulloch, D. S., and Vedder, J. G., 1980, Basin development along the late Mesozoic and Cenozoic California margin: a plate tectonic margin of subduction, oblique subduction, and transform tectonics, *in* Ballance, P. F., and Reading H. G., eds., Sedimentation in oblique-slip mobile zones: International Association of Sedimentologists Special Publication 4, pp. 43-62.

Ingersoll, R. V., 1979, Evolution of the Late Cretaceous forearc basin, northern and central California: Geological Society of America Bulletin, pt. 1, v. 90, pp. 813-826.

Ito, H., Devilbiss, J., and Nur, A., 1989, Compressional and shear-waves in saturated rock during water-steam transition *in* Nur, A., and Wang, Z., eds., Seismic and acoustic velocities in reservoir rocks, Society of Exploration Geophysicists, 183-187.

Kallweit, R. S. and Wood, L. C., 1982, The limits of resolution of zero-phase wavelets: Geophysics, 47, pp. 1035-1046.

Kaplow, E. J., 1945, Coalinga Oil Field: California Oil Fields, Summary of Operations, California Division of Oil and Gas, v. 31, no. 2, pp. 5-22.

Keys, Robert G., 1989, Short note – Polarity reversals in reflections from layered media, Geophysics, v. 54, no. 7, pp. 900-905.

Kidd, D. Gerald, 1999, Fundamentals of 3-D seismic volume visualization, The Leading Edge, v. 18, pp. 702-712.

Levin, F. K., 1986, When reflection coefficients are zero, Geophysics, v. 51, pp. 736-741.

Liner, Christopher, L., 1997, On the history and culture of geophysics, and science in general: The Leading Edge, v. 16, Issue 1, p. 61

Lipman, P. W., Prostka, H., J., and Christiansen, R. L., 1972, Cenozoic volcanism and plate-tectonic evolution of the western United States. I. Early and middle Cenozoic: Philosophical Transactions of the Royal Society of London, Series A, v. 271, pp. 217-248.

Lumley, D. E., Tura, A., Kempner, W., Klonsky, L., F., and Ecker, C., 2001, 4D Seismic Monitoring of steam injection at Coalinga field, California,: Abstract, Geological Society of America, Cordilleran Section – 97th Annual Meeting, and Pacific Section, AAPG, Session No. 45, Geophysical Application and Interpretation (Sponsored by the Society of Exploration Geophysicists), Universal City, California, April 11.

Lynch, Steven and Lines, L., 2004, Combined attribute display: Expanded abstract, SEG 74th Ann. Intl. Convention, Denver, Colorado, USA.

Mahapatra, Sailendra N., Imhof, Matthias, G., and Kempner, W., 2003a, Deterministic High-Resolution Seismic Reservoir Characterization: Abstract, AAPG Annual Meeting 2003: Energy - Our Monumental Task Technical Program, Salt Lake City, Utah, USA.

Mahapatra, Sailendra N., Imhof, Matthias, G., and Kempner, W., 2003b, Poststack interpretive static correction: Expanded abstract, 73rd SEG Ann. Intl. Convention, Dallas, Texas, USA.

Mahapatra, Sailendra N., Imhof, Matthias, G., and Kempner, W., 2004, Seismostratigraphic and seismogeomorphic reservoir characterization in Coalinga field: Expanded abstract, SEG 74th Ann. Intl. Convention, Denver, Colorado, USA.

Mahapatra, Sailendra N., Imhof, Matthias, G., and Kempner, W., 2005, Integrated reservoir heterogeneity delineation of Coalinga field: Expanded abstract, SEG 75th Ann. Intl. Convention, Houston, Texas, USA (in press).

McWilliams, Michael, and Li, Yianping, 1985, Oroclinal bending of the southern Sierra Nevada batholith: Science, v. 230, pp. 172-175.

Marchand, D. E., 1977, The Cenozoic history of the San Joaquin Valley and adjacent Sierra Nevada as inferred from the geology and soils of the eastern San Joaquin Valley, *in* Singer, M. J., ed., Soil development, geomorphology and Cenozoic history of the northeastern San Joaquin Valley and adjacent areas, California: American Society of Agronomy, Geological Society of America, Soil Sciences Society of America, Joint field section 1977, Guidebook, Davis, University of California Press, pp. 39-50.

Marchand, D. E., and Allwardt, Allan, 1981, Late Cenozoic stratigraphic units, northeastern San Joaquin Valley, California: U. S. Geological Survey Bulletin 1470, 70 p.

Marfurt, Kurt, J., Kirlin, R., Lynn, Farmer, Steven, L., and Bahorich, Michael, S., 1998, 3-D seismic attributes using a semblance-based coherency algorithm, Geophysics, 63, pp. 1150-1165.

Mavko, B. B., and Thompson, G. A., 1983, Crustal and upper mantle structure of the northern and central Sierra Nevada: Journal of Geophysical Research, v. 88, no. B7, pp. 5874-5892.

Mavko Gary, Mukherji Tapan, and Dvorkin, 1998, The Rock Physics Handbook: Tolls for Seismic Analysis in Porous Media, Cambridge University Press, p. 329.

Minster, J. B., and Jordan, T. H., 1984, Vector constraints on Quaternary deformation of the western United States east and west of the San Andreas fault, *in* Crouch, J. K., and Bachman, S. B., eds., Tectonics and sedimentation along the California margin: Society of Economic Paleontologists and Mineralogists, Pacific Section, Annual Meeting, 1984, San Diego, California, pp. 1-16.

Meyer, E. Douglas, Harvey, L. Elizabeth et al., 2001, Use of seismic attributes in 3-D geovolume interpretation, The Leading Edge, Issue 12, pp. 1377-1380 and 1400.

Nilsen, T. H., 1996, Regional geology of the southwest San Joaquin Basin, California, in T. H. Nilsen, A. S. Wylie, Jr., and G. J. Gregory, eds., Geology of the Midway-Sunset Oil Fields: AAPG Field Trip Guidebook, pp. 7-38.

Nilsen, T. H., 1984, Oligocene tectonics and sedimentation, California, Sedimentary Geology, v. 37, pp. 305-336.

Nilsen, T. H., and Clarke, S. H. Jr., 1975, Sedimentation and tectonics in the early Tertiary continental borderland of central California: U. S. Geological Survey Professional Paper 925, 64 p.

Olsen, H. C., Miller, G. E., and Bartow, J. A., 1986, Stratigraphy, paleoenvironment and depositional setting of Tertiary sediments, southeastern San Joaquin basin, in Structure and stratigraphy of the east side San Joaquin Valley: American Association of Petroleum Geologists, Pacific Section, Southeast San Joaquin Valley Field Trip, April 18-19, 1986, Guidebook, pp. 18-56.

Page, B. M., 1981, The southern Coast Ranges, *in* Ernst, W. G., ed., The geotectonic development of California (Rubey volume 1): Englewood Cliffs, N. J., Prentice-hall, pp. 329-417.

Page, B. M., and Engebretson, D. C., 1984, Correlation between the geologic record and the computed plate motions of central California, Tectonics, v. 3, pp. 133-155.

Partyka, G., 2000, Seismic attribute sensitivity to energy, bandwidth, phase, and thickness, 70th Ann. Internat. Mtg: Society of Exploration Geophysists, 2405-2408.

Pattison, Simon, A. J., 2005, Isolated highstand shelf sandstone body of turbiditic origin, lower Kenilworth Member, Cretaceous Western Interior, Book Cliffs, Utah, USA, Sedimentary Geology, 177, pp. 131-144

Peters, K. E., Pytte, M. H., Elam, T. D., and Sundararaman, P., 1994, Identification of Petroleum Systems Adjacent to the San Andreas Fault, California, USA, *in* Magoon, L. B., and Dow, W. g., eds., The Petroleum system-from source to trap: American Association of Petroleum Geologists Memoir 60, pp. 423-436.

Piver, Jaimes L., 2004, Integration of geologic models and seismic data to characterize interwell heterogeneity of the Miocene Temblor formation, Coalinga, California. Master's thesis, Clemson University.

Raymond, L. a., 1969, The stratigraphic and structural geology of the northern Lone Tree Creek and southern Tracy quadrangles: San Jose, California, San Jose State College, M. S. thesis, p. 143.

Repenning, C. A., 1960, Geologic summary of the central Valley of California with reference to the disposal of liquid radioactive waste: U. S. geological Survey Trace Element Investigation report 769, 69 p.

Schamel Steven, Deo Milind, and Deets Mike, 2002, Reactivation of an idle lease to increase heavy oil recovery through application of conventional system drive technology in a low dip slope and basin reservoir in the Midway-Sunset Field, San Joaquin Basin, California, DOE Class III Oil Technology Demonstration, Final Report, p. 146

Schamel Steven, 1999, Reactivation of an idle lease to increase heavy oil recovery through application of conventional system drive technology in a low dip slope and basin reservoir in the Midway-Sunset Field, San Joaquin Basin, California, DOE Class III Oil Technology Demonstration, Annual Report, p. 53

Shedd, Solon, 1932, Bibliography of the geology and mineral resources of California to December 31, 1930: California Division of Mines Bulletin 104, p. 376

Sheffield, M., Tatum, et al, 2000, Geovolume visualization interpretation: A lexicon of basic techniques, The Leading Edge, v. 19, Issue 5, p. 518-522

Sheriff, Robert E., 1984, Encyclopedic Dictionary of Exploration Geophysics, 2nd ed.: Society of Exploration Geophysicists Publication.

Taner M. T., 2001, Seismic attributes, CSEG Recorder, pp. 48-56.

Taner, M. T., Schuelke, James S., O'Doherty, Ronen and Baysal, Edip, 1994, Seismic attributes revisited, 64th Annual Internat. Mtg., Soc. Expl. Geophys., Expanded Abstracts, 1104-1106.

Taner, M. T. Koehler, F., and Sheriff, R., E., 1979, Complex seismic trace analysis, Geophysics, 44, pp. 1041-1063

Taner, M. T. and Sheriff, R. E., 1977, Application of amplitude, frequency and other attributes to stratigraphic and hydrocarbon determination, in C. E. Payton, ed., Seismic Stratigraphy: Applications to Hydrocarbon Exploration. AAPG Memoir 26, pp. 301-327.

Walker, R. G., 1981, Turbidites and associated coarse clastic deposits, in Walker, R. g., ed., Facies Models, Geosciences Canada Reprint Series 1, pp. 91-104

Wang Zhijing (Zee), 2001, Y2K Tutorial: Fundamentals of seismic rock physics, Geophysics, v. 66, No. 2, pp. 398-412.

Wang, Z., and Nur, A., 1989, Effect of temperature on wave velocities in sandstones and sands with heavy hydrocarbons *in* Nur, A., and Wang, Z., eds., Seismic and acoustic velocities in reservoir rocks, Society of Exploration Geophysicist, 188-194.

Webb, M. G., 1978, Monarch sandstone: reservoir description in support of a steam flood, Section 26C, Midway Sunset Field, California, Journal of Canadian Petroleum Technology, pp. 31-40.

Wentworth, C. M., 1985, Central California deep crustal study: U. S. Geological Survey Open-File Report 86-31, pp. 98- 102.

Wentworth, C. M., Blake, M. C., Jr., Jones, D. L., Walter, A. W., and Zoback, M. D., 1984, Tectonic wedging associated with emplacement of the Franciscan assemblage, California Coast Ranges, *in* Blake, M. C., ed., Franciscan geology of northern California: Los Angeles, Society of Economic paleontologists and Mineralogists, Pacific Section,, pp. 163-173.

White, E. Roy, 1992, Properties of instantaneous seismic attributes, Geophysics: The Leading Edge of Exploration, July 1991, pp. 26-32.

Yilmaz, Ozdogan, 1987, Seismic data processing: Society of Exploration Geophysics Investigations in Geophysics, v.2, 526 p.

Zobak, M. L., Anderson, R. E., and Thompson, G. A., 1981, Cenozoic evolution of the state of stress and styles of tectonism of the Basin and Range provinces of the Western United States: Philosophical Transaction of the Royal Society of London, Series A, v. 300, no. 1454, pp. 407-434.

Zobak, M. D., Zobak, M. L., Mount, V. S., Suppe, J., Eaton, J. P., Healy, J. H. et al., 1987, New evidence on the state of stress of the San Andreas fault system: Science, v. 238, pp. 1105-1111.

Figures

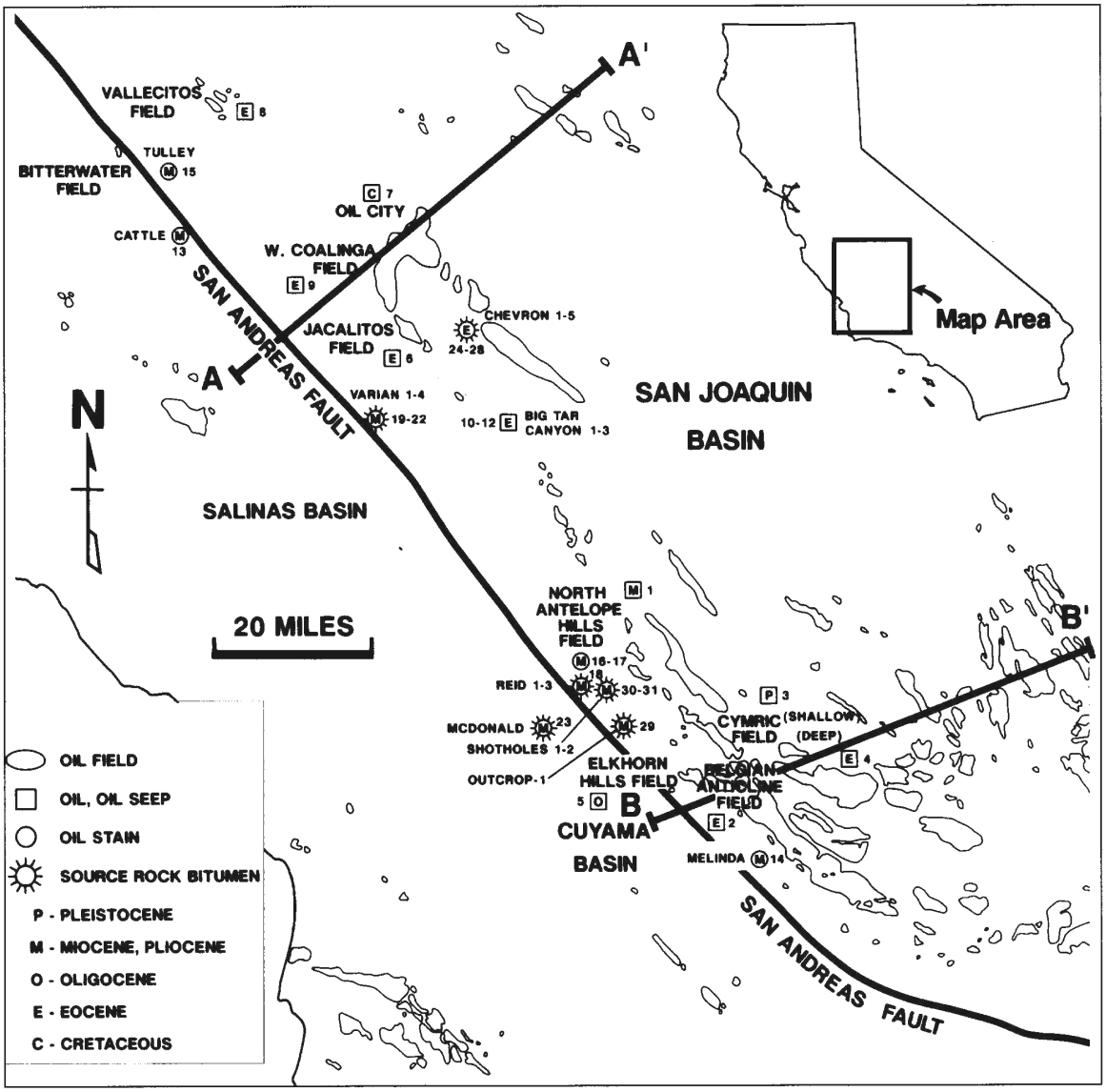

Figure 1. Map showing the oil fields, locations of oil seep, oil stain, and source rocks with their geological ages around the San Andreas fault and the San Joaquin basin. Location of the cross sections A-A' and B-B' in Figure 2 are shown. (after Peters et al., 1994), the symbol "SUN" denotes sample point.

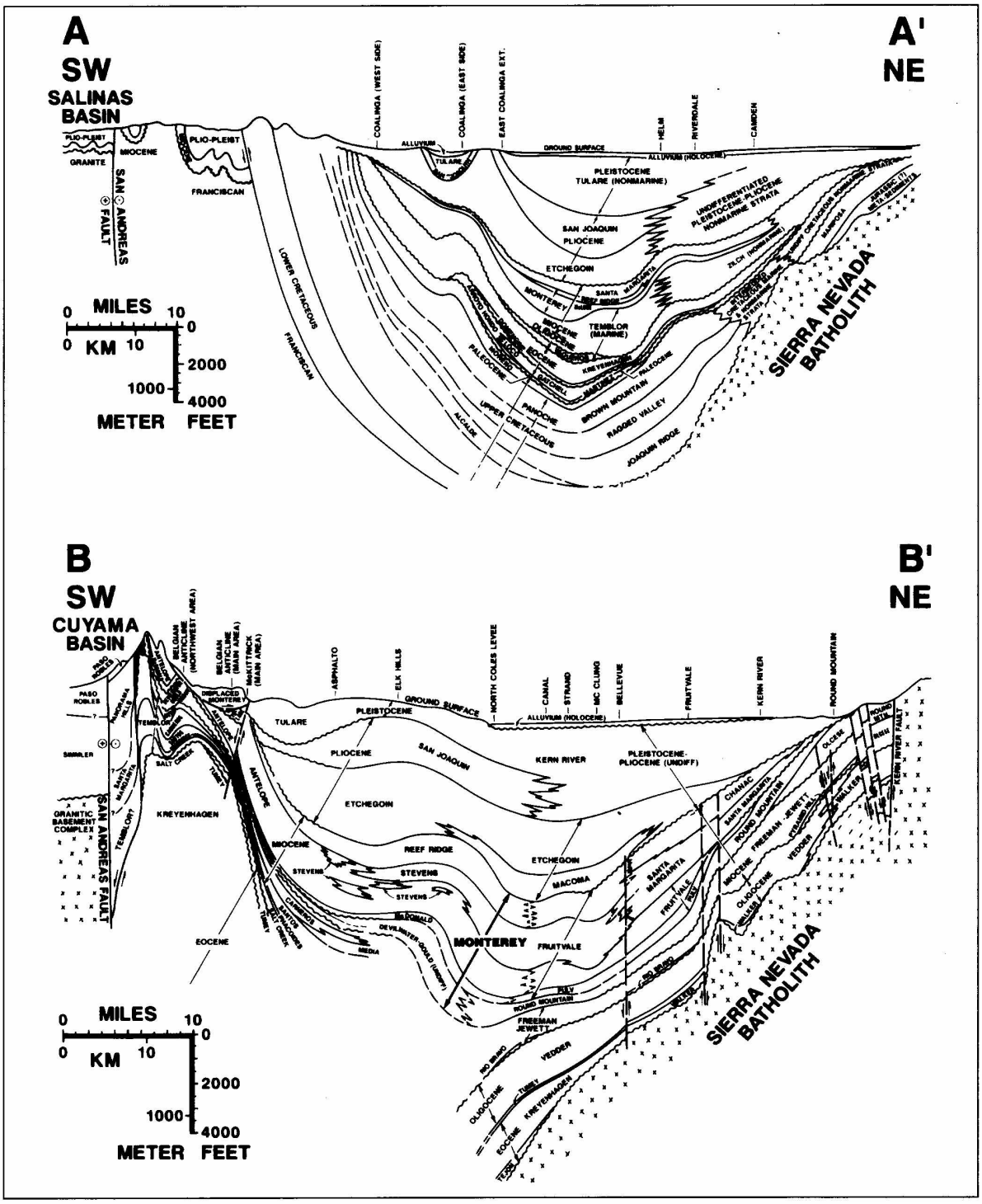

Figure 2. Cross section A-A' and B-B' showing the stratigraphic units and the structural relationships of the sedimentary rocks in the San Joaquin basin and on both sides of the San Andreas Fault.

(after Peters, et al., 1994)

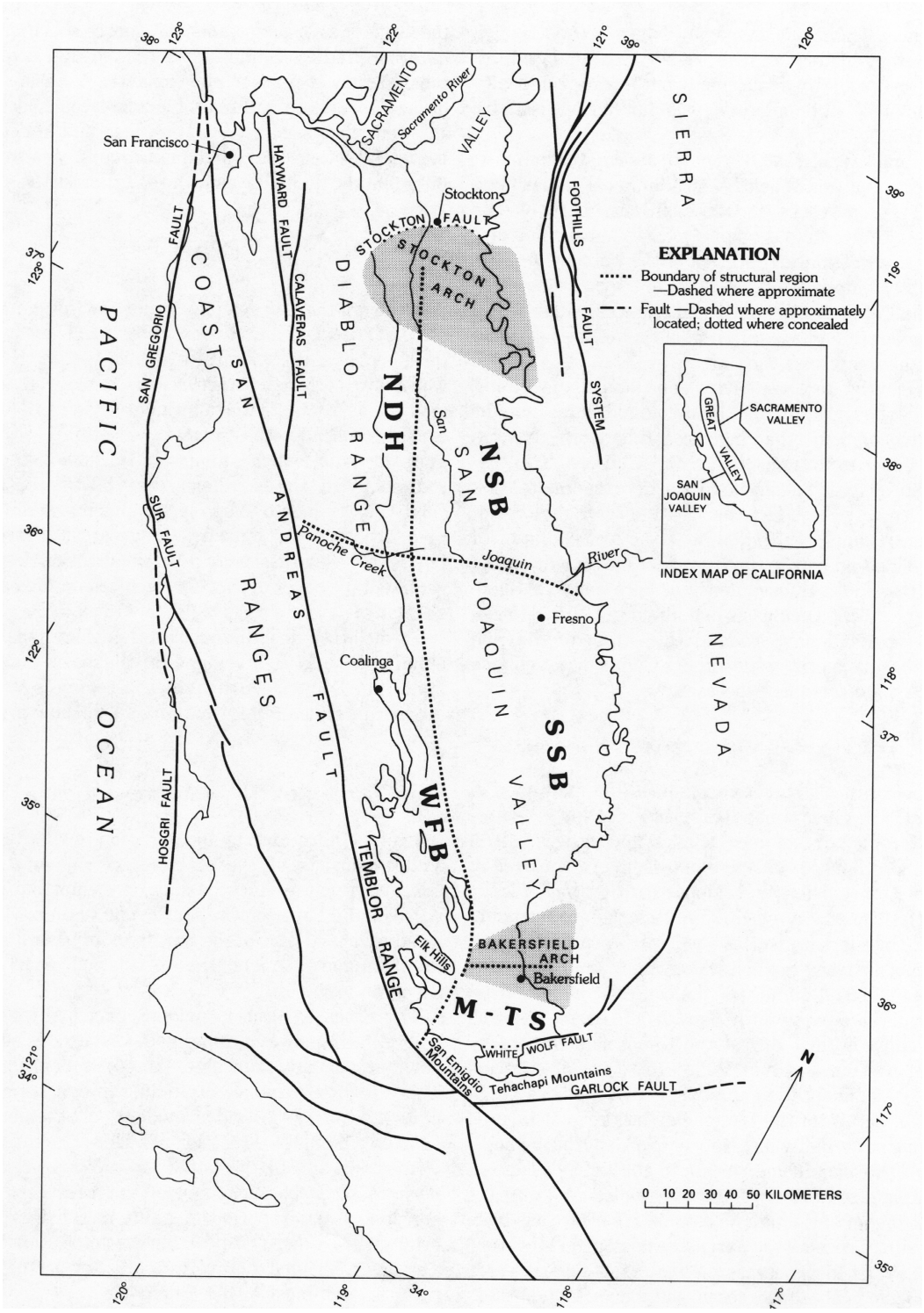

Figure 3. Index map of central California showing the five structural regions of the San Joaquin Valley in relation to principal geographic and structural features. NSB, northern Sierran block; SSB, southern Sierran block; NDH, northern Diablo homocline; WFB, westside fold belt; M-TS, Maricopa-Tejon subbasin and south-margin deformed belt.

(after Bartow, 1991)

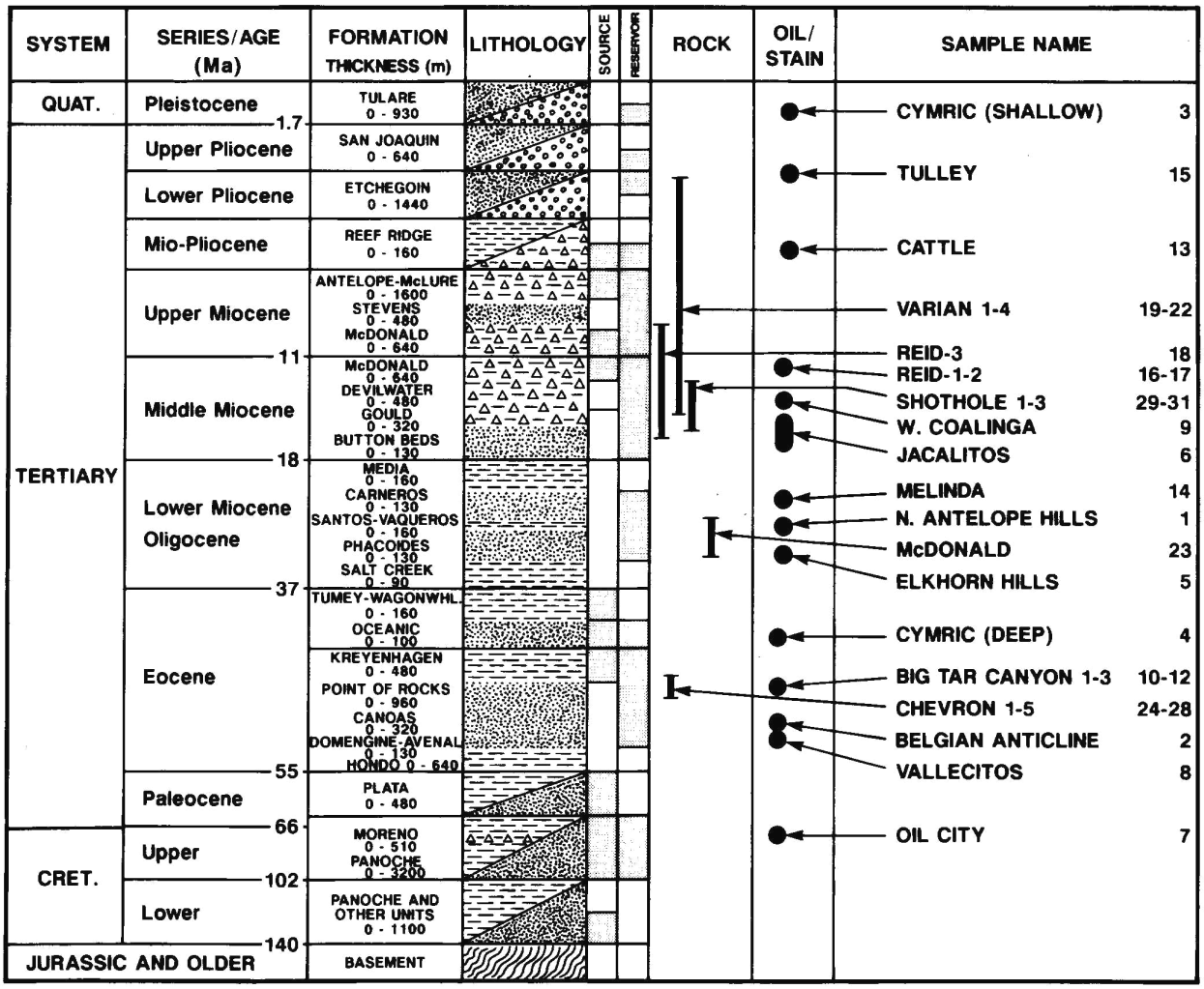

Figure 4. A generalized stratigraphic column for the San Joaquin basin. The figure also shows the occurrences of oil fields, oil seeps/stain and source rocks against the stratigraphic horizons. The numbers in the extreme right column point to the locations in Figure 1.

(after Peters, et al., 1994)

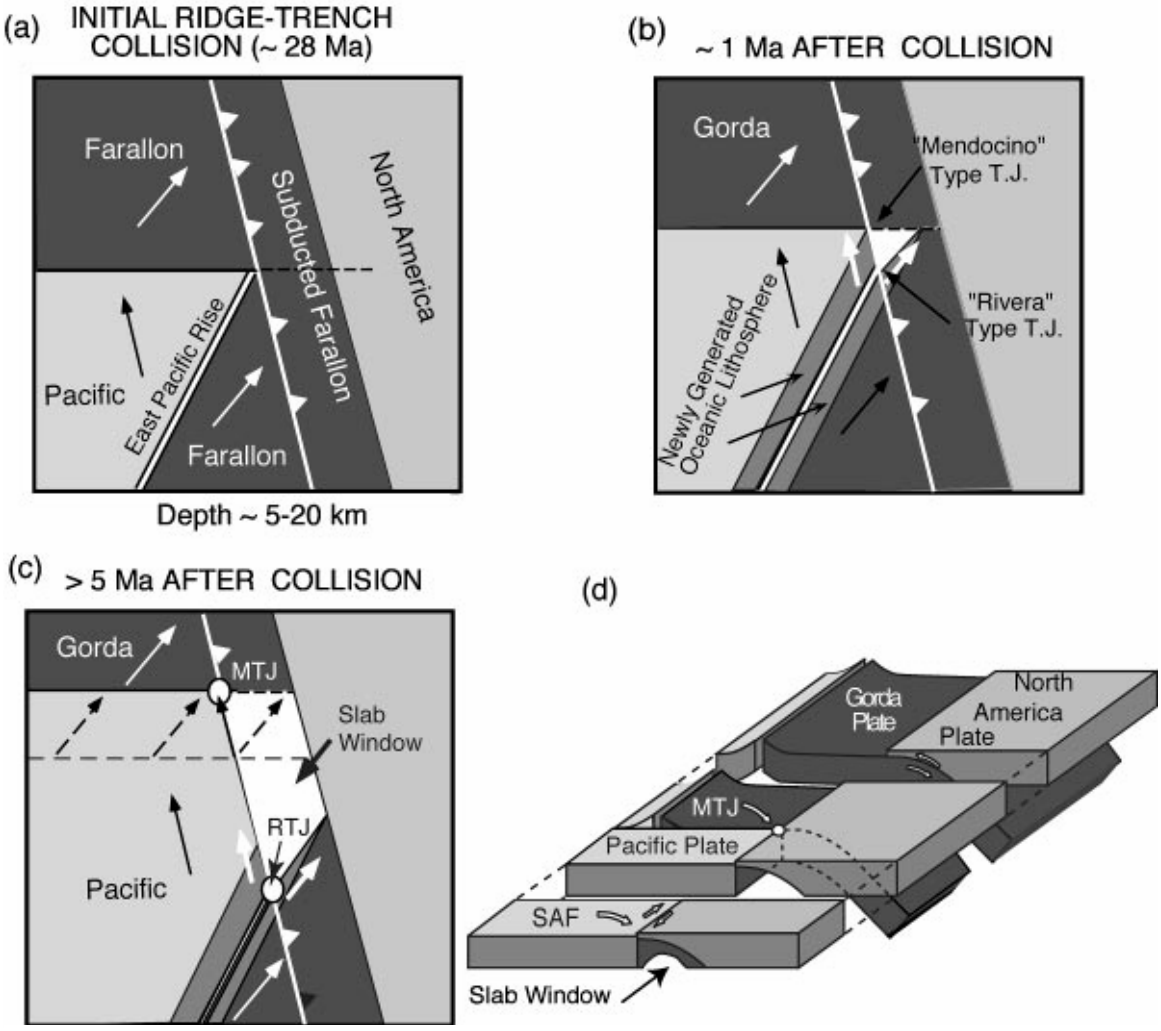

Figure 5. Schematic view of the plate tectonic evolution that led to the formation of the MTJ and the resulting slab window. (*a*) Initial plate configuration just prior to triple junction formation. Arrows indicate directions of movements of Pacific (PAC) and Farallon (FAR) plates with respect to North America (NOAM). (*b*) Plate configuration immediately after the formation of the MTJ and the associated RTJ. Short white arrows indicate motion of newly formed oceanic lithosphere with respect to NOAM. (*c*) Plate configuration after the triple junctions have stabilized and separated. Dashed line and dashed arrows indicate the path of the Mendocino Fracture Zone through time and the development of a sharp northern edge to the slab window. Solid arrow along plate boundary indicates MTJ motion. (*d*) Three-dimensional sketch of the development of the slab window in the vicinity of the MTJ. The initial shape of the slab window should mimic the geometry of the previously subducted Gorda slab.

(After Furlong and Schwartz, 2004)

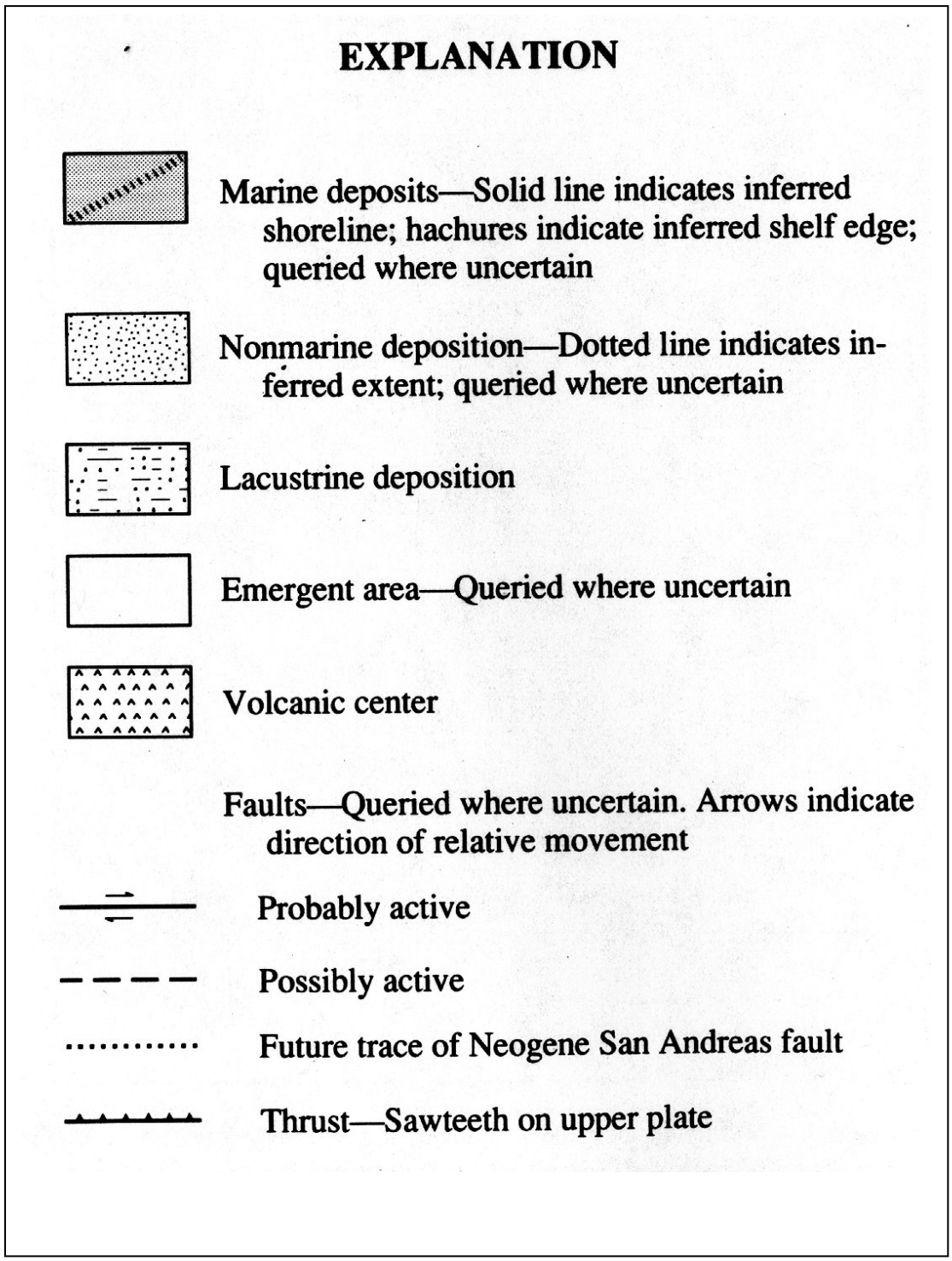

Figure 6(a). Legend and explanation for figures 6(b) through 6(j).

(compiled by Bartow, 1991)

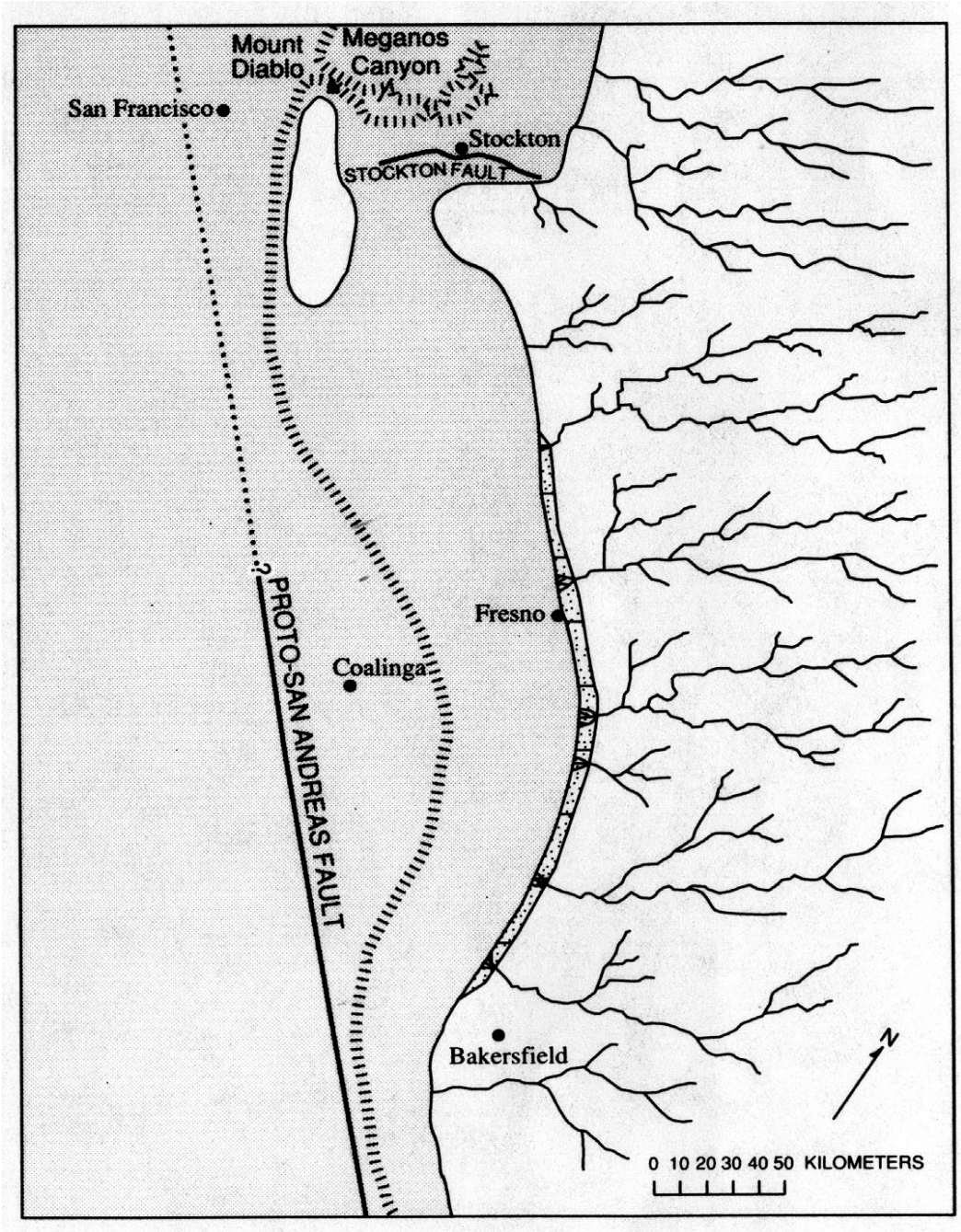

Figure 6(b). Late Paleocene (about 59 Ma) paleogeography of the San Joaquin basin area.

(compiled by Bartow, 1991)

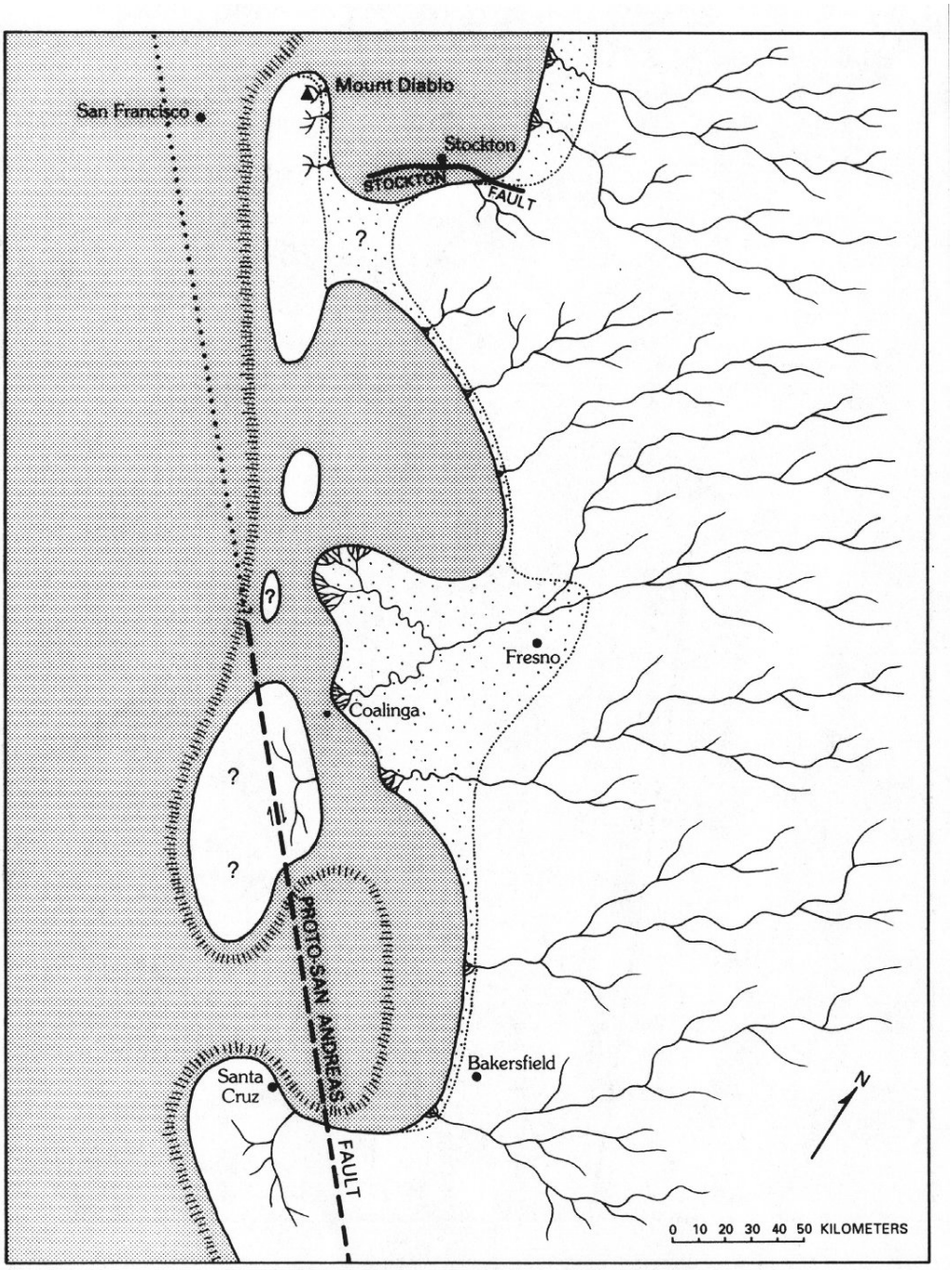

Figure 6(c). Early to middle Eocene (about 52 Ma) paleogeography of the San Joaquin basin area.

(compiled by Bartow, 1991)

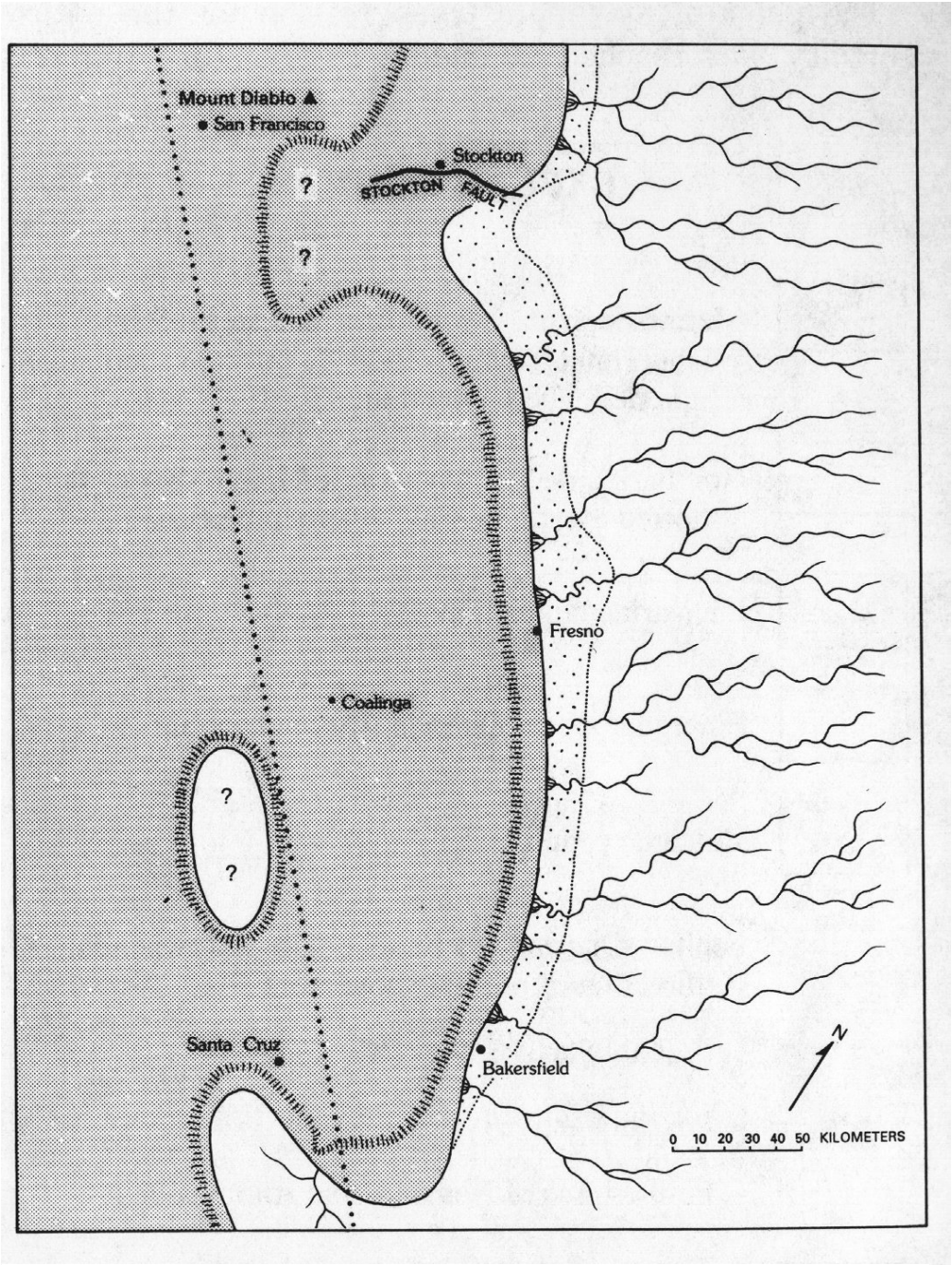

Figure 6(d). Middle Eocene (about 44-45 Ma) paleogeography of the San Joaquin basin area.

(compiled by Bartow, 1991)

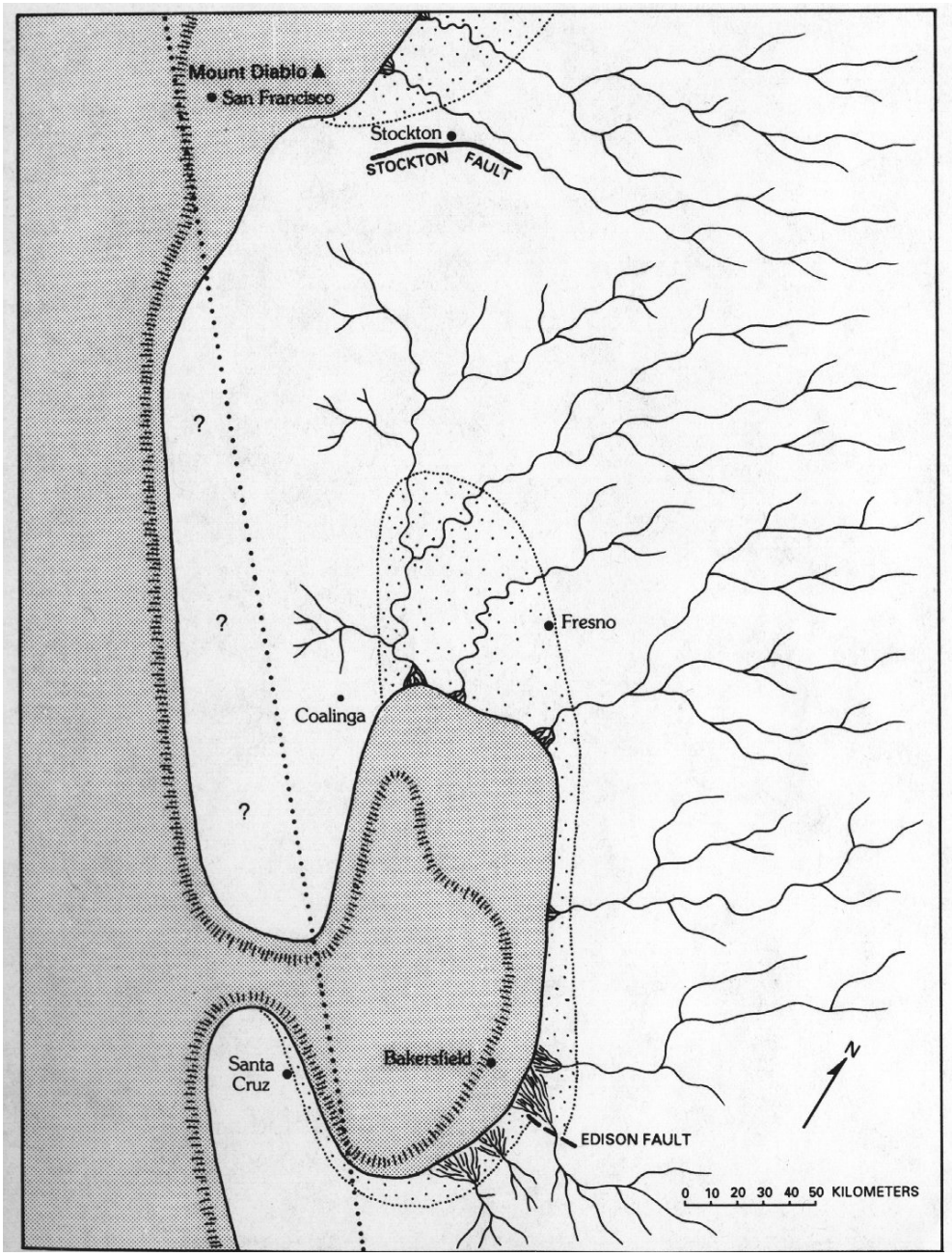

Figure 6(e). Oligocene (about 30 Ma) paleogeography of the San Joaquin basin area.

(compiled by Bartow, 1991)

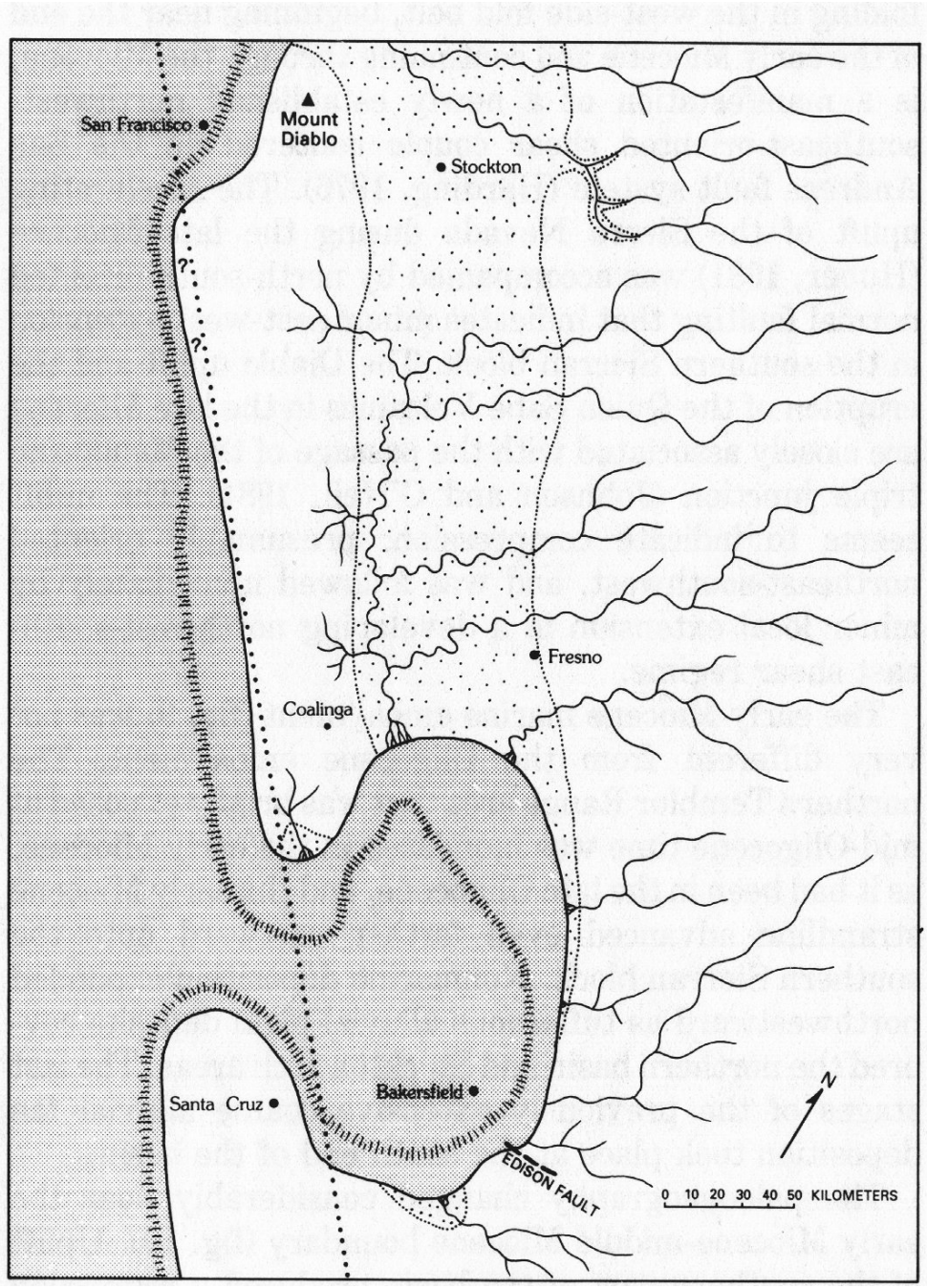

Figure 6(f). Early Miocene (about 20-21 Ma) paleogegraphy of the San Joaquin basin area.

(compiled by Bartow, 1991)

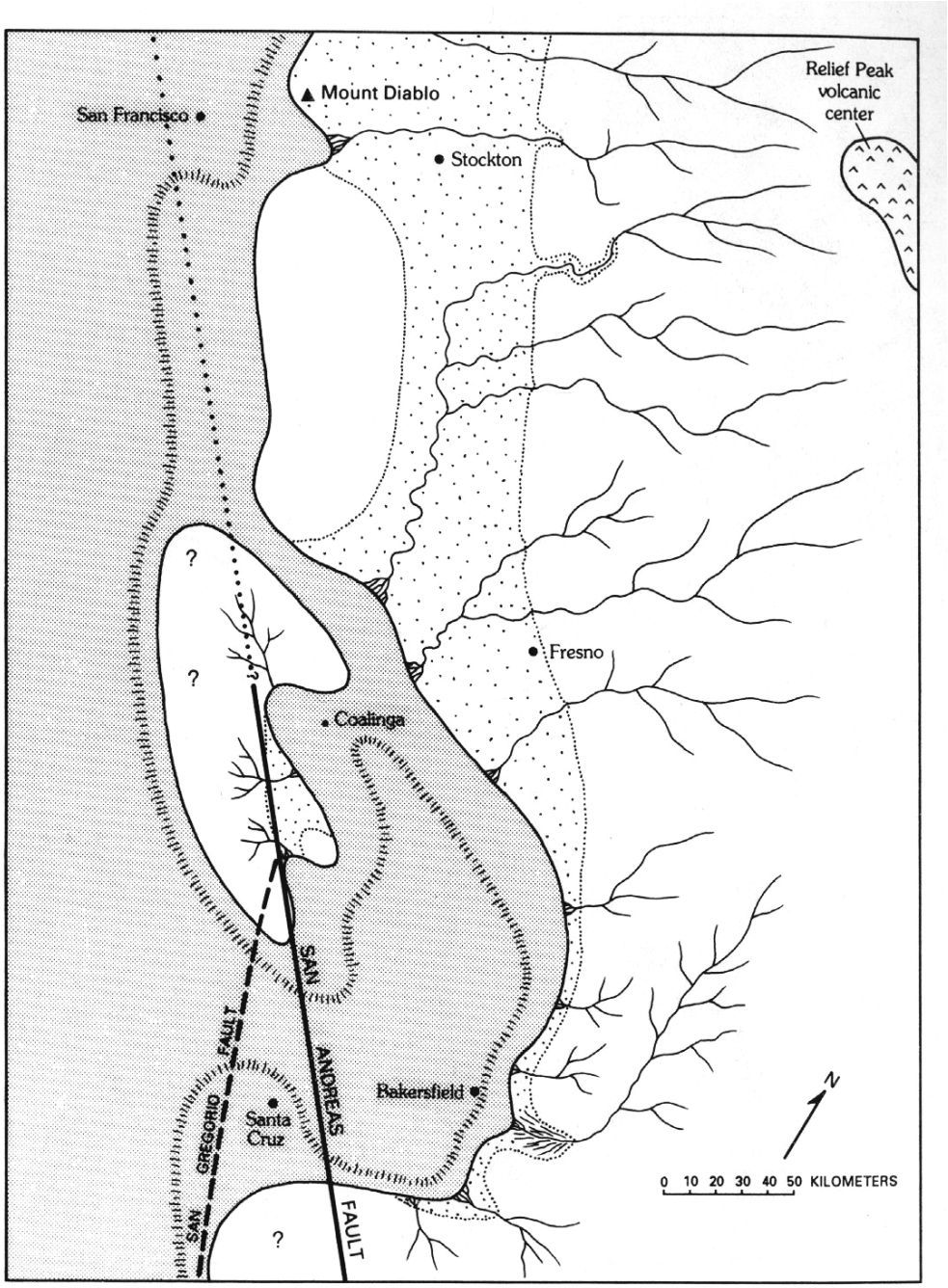

Figure 6(g). Middle Miocene (about 16 Ma) paleogeography of the San Joaquin basin area.

(compiled by Bartow, 1991)

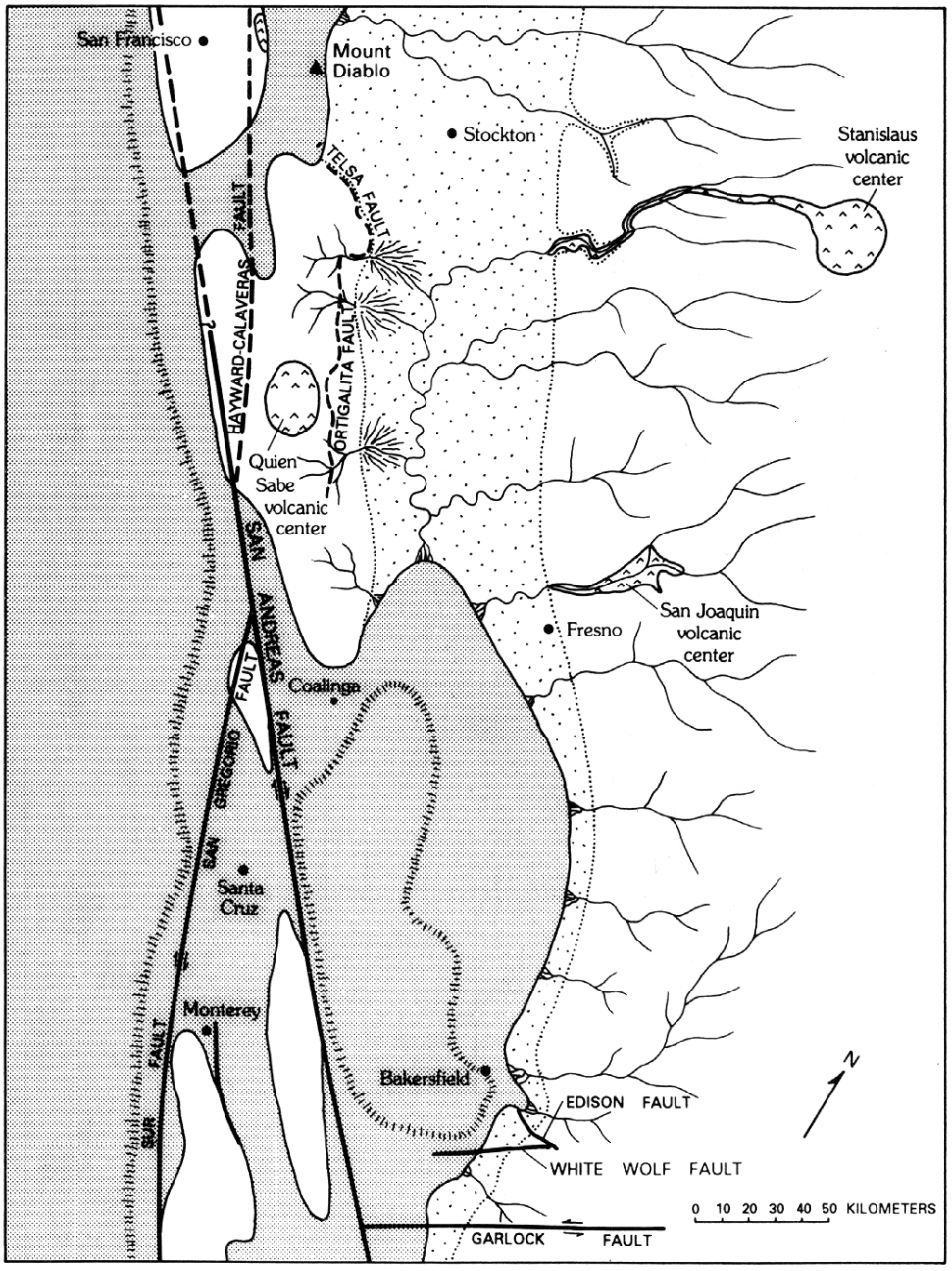

Figure 6(h). Late Miocene (about 9-10 Ma) paleogeography of the San Joaquin area, Santa Cruz position shifted NNW because of strike-slip movement of the San Andreas Fault.

(compiled by Bartow, 1991)

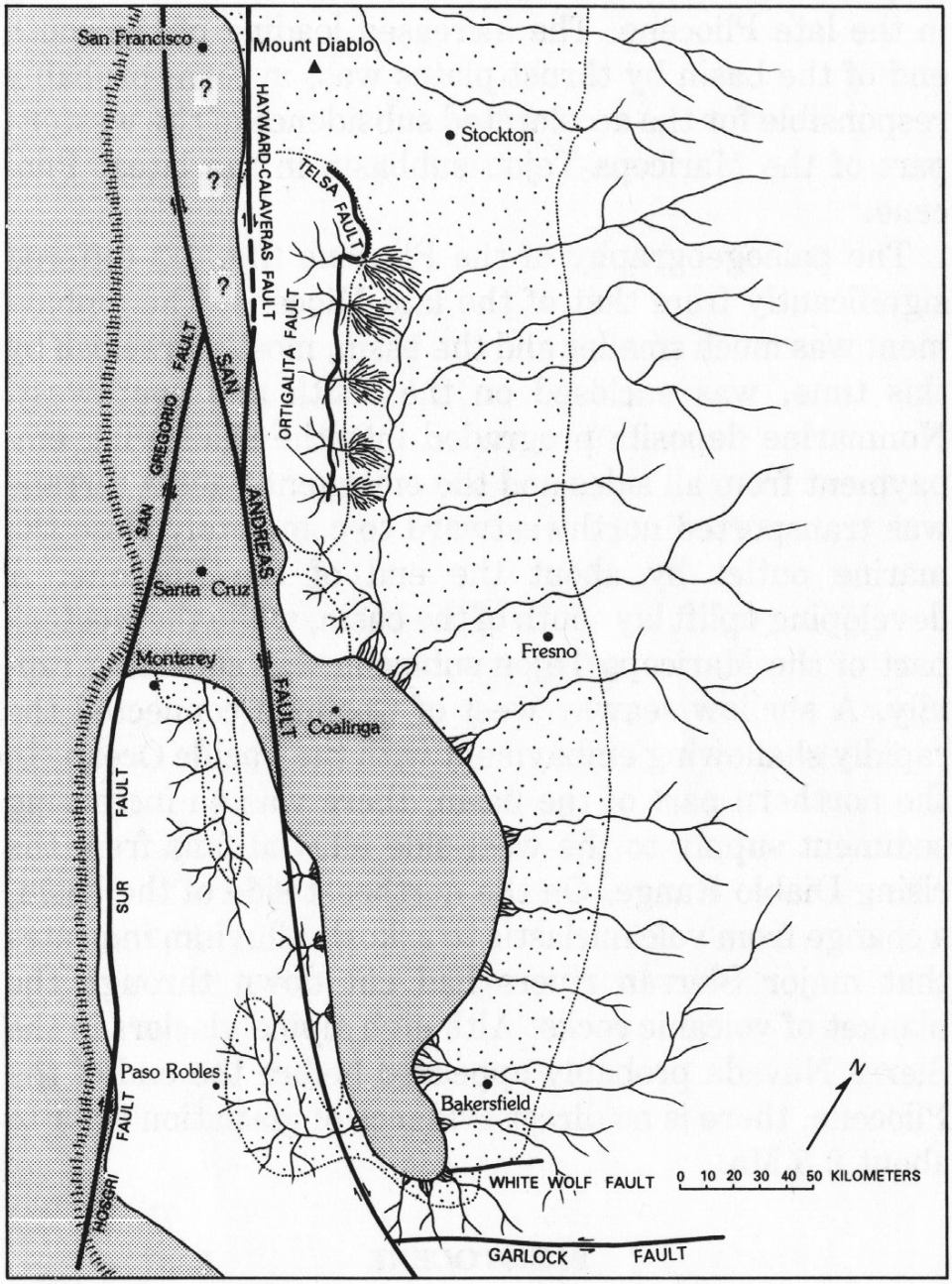

Figure 6(i). Pliocene (about 3-4 Ma) paleogeography of the San Joaquin basin area, the relative positions of towns are changed due to strike-slip movement of the San Andreas Fault and associated faults.

(compiled by Bartow, 1991)

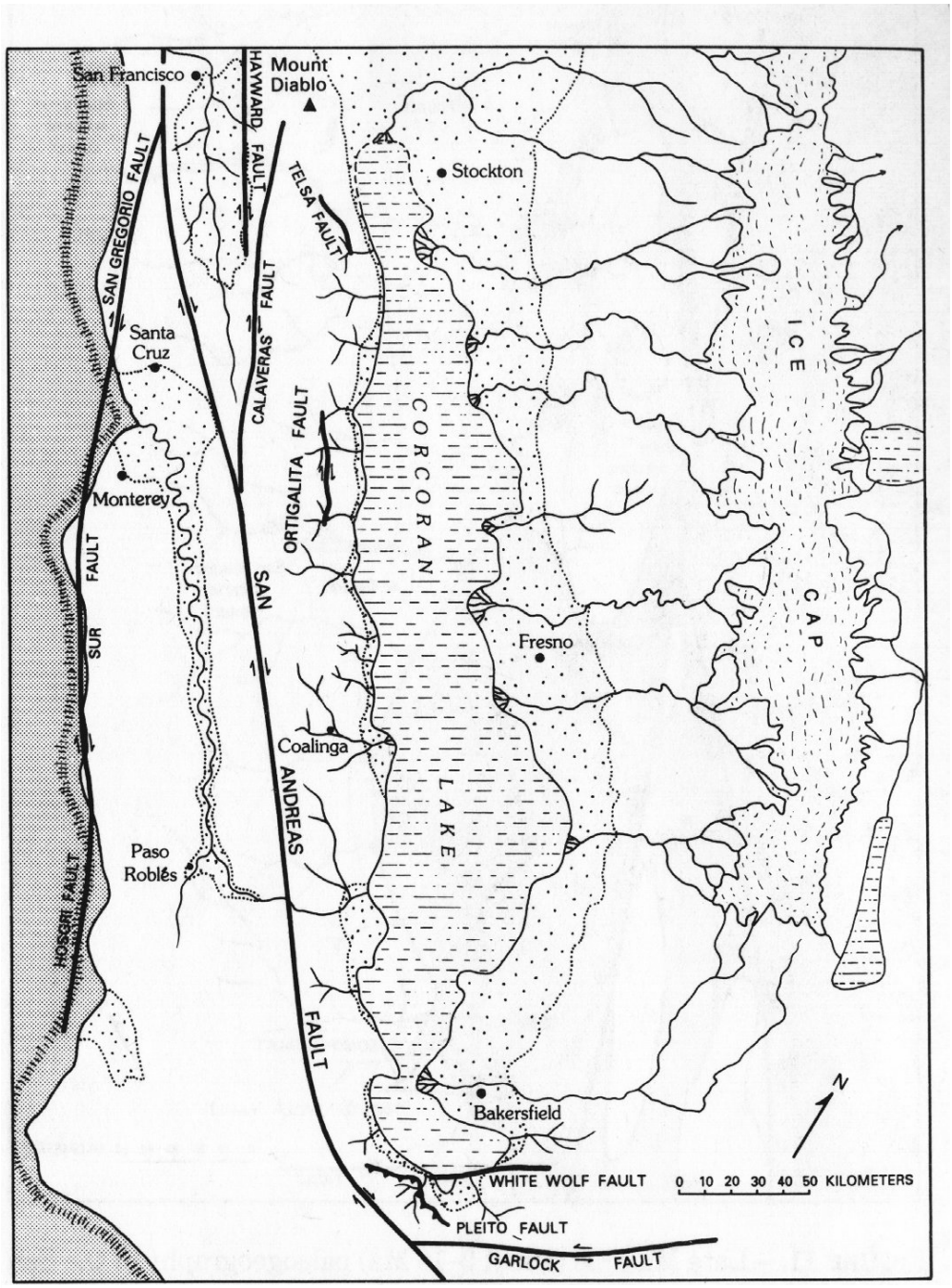

Figure 6(j). Pleistocene (about 0.6-0.7 Ma) paleogeography of the San Joaquin basin area.

(compiled by Bartow, 1991)

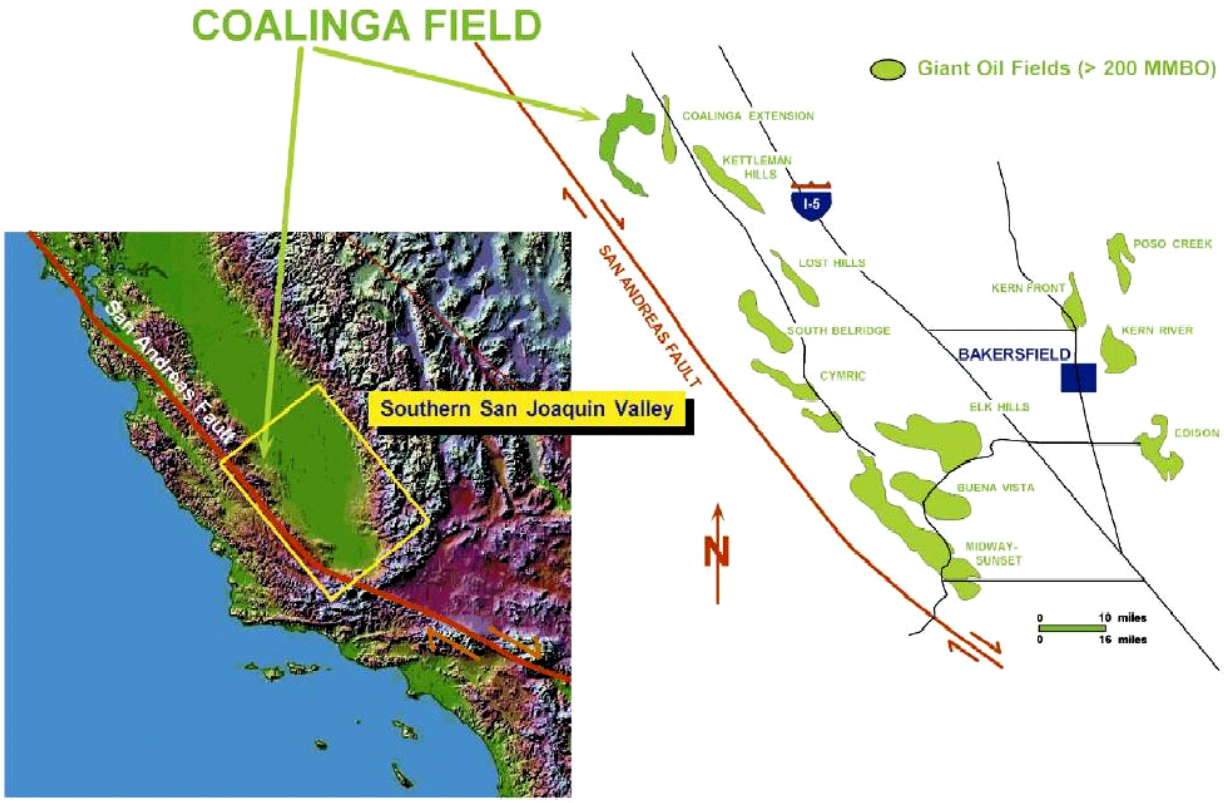

Figure 7. Location map showing proximity of the Coalinga field to the San Andreas Fault on the west side of the San Joaquin Valley.

(after Clark et al., 2001b)

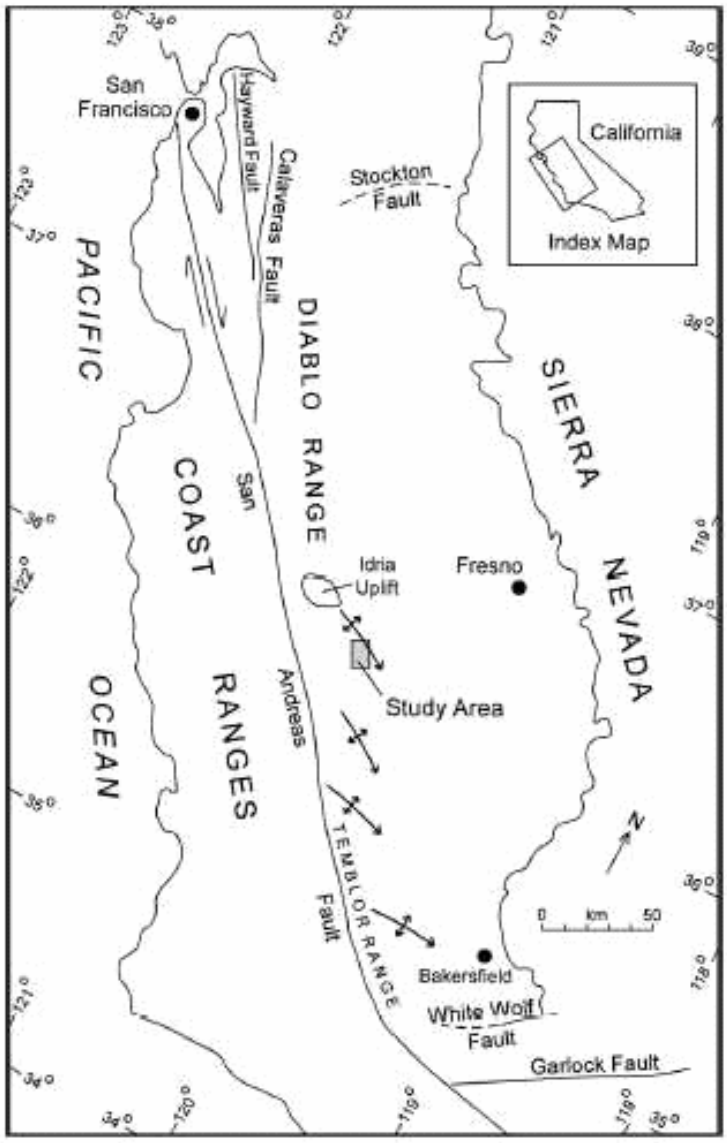

Figure 8. Regional location map. Faults are dashed where location is approximate.

(after Bridges and Castle, 2003)

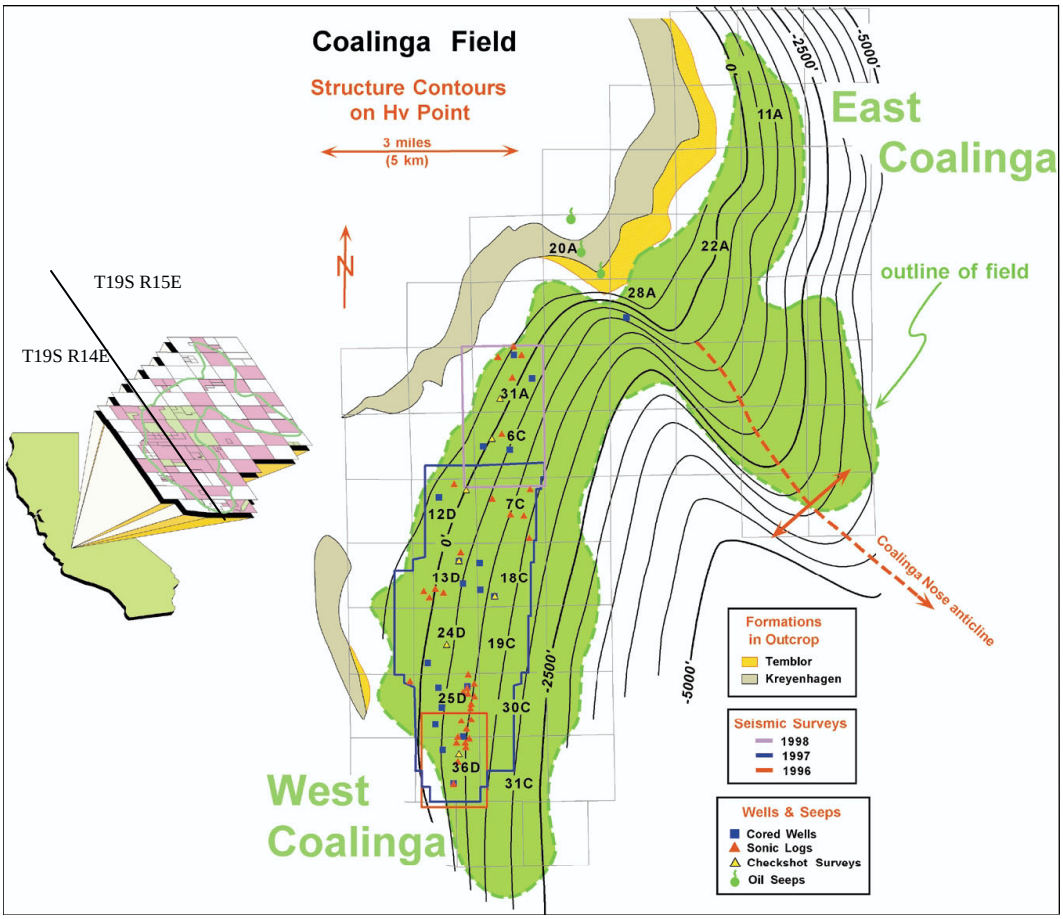

Figure 9. Division of Coalinga Field into West Coalinga and East Coalinga areas. The Coalinga Nose anticline represents the East Coalinga part of the field, and the monoclinal flank represents the West Coalinga field (after Clark et al., 2001b). The reference coordinates (Townships and Ranges) are shown on the index map.

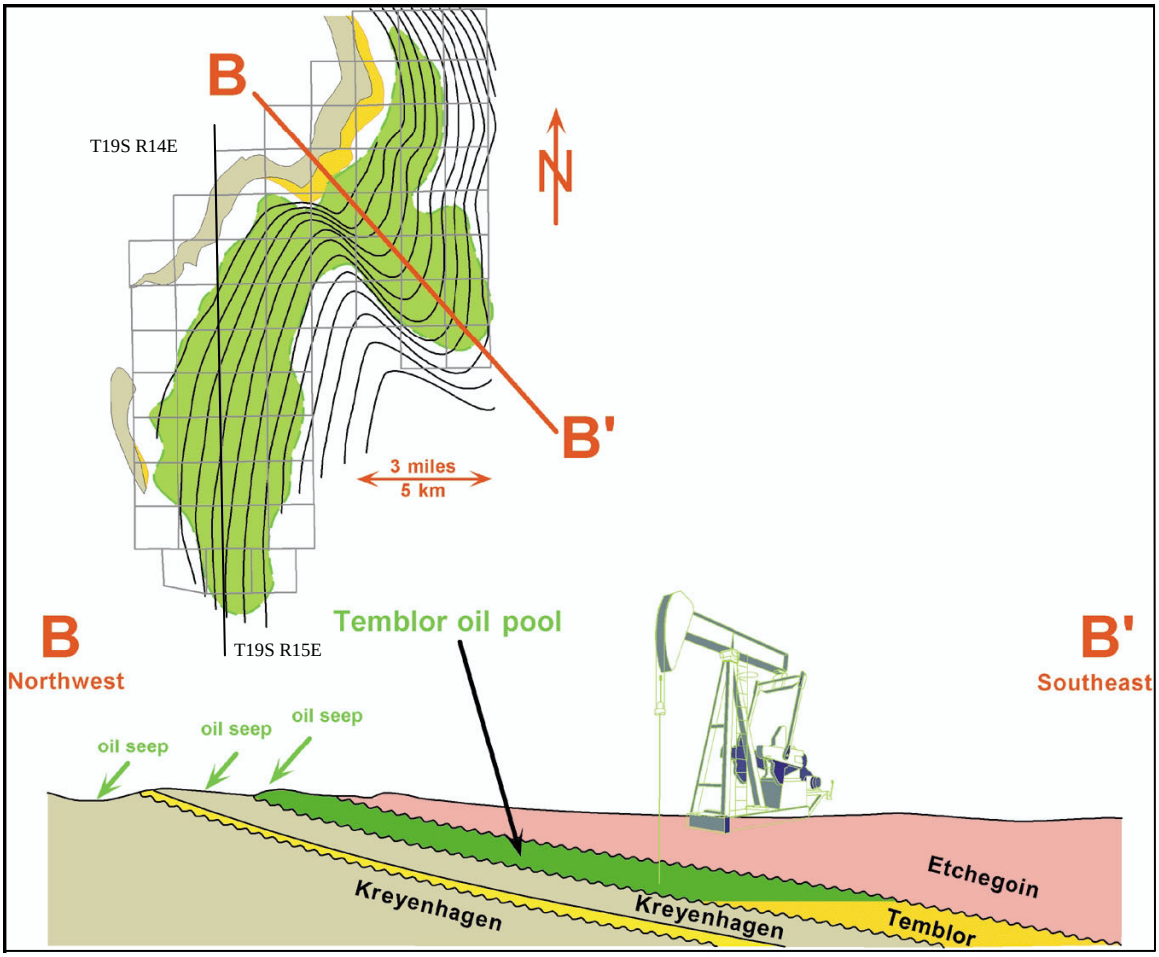

Figure 10. Cross section B-B[1] showing absence of an updip seal at Coalinga, where the Temblor reservoir is breached at the surface. Oil accumulates behind near-surface, tight rocks, and tar seals to create a giant field (after Clark, et al., 2001b). The reference coordinates (Townships and Ranges) are shown in top.

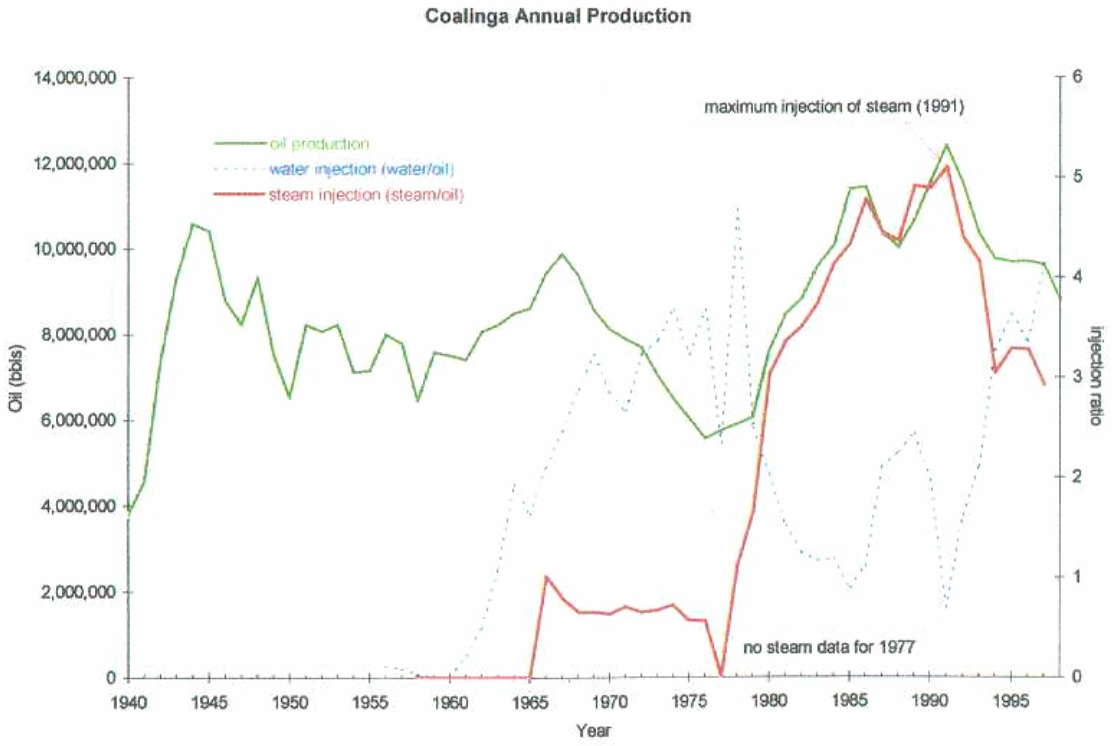

Figure 11. Shows annual oil production from 1940 to 1998. The green, blue, and red color graphs show the oil, water and steam injection over the years.

(after Clark et al., 2001a)

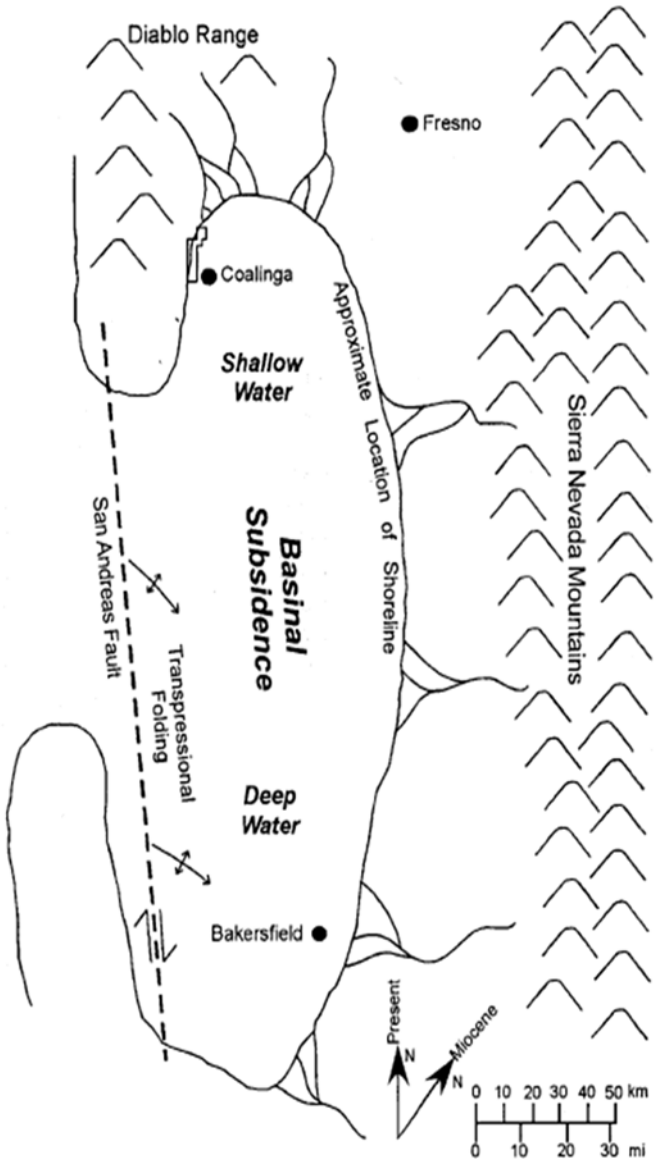

Figure 12. Paleogeography of the San Joaquin basin during deposition of the Temblor Formation.

(after Bridges and Castle, 2003)

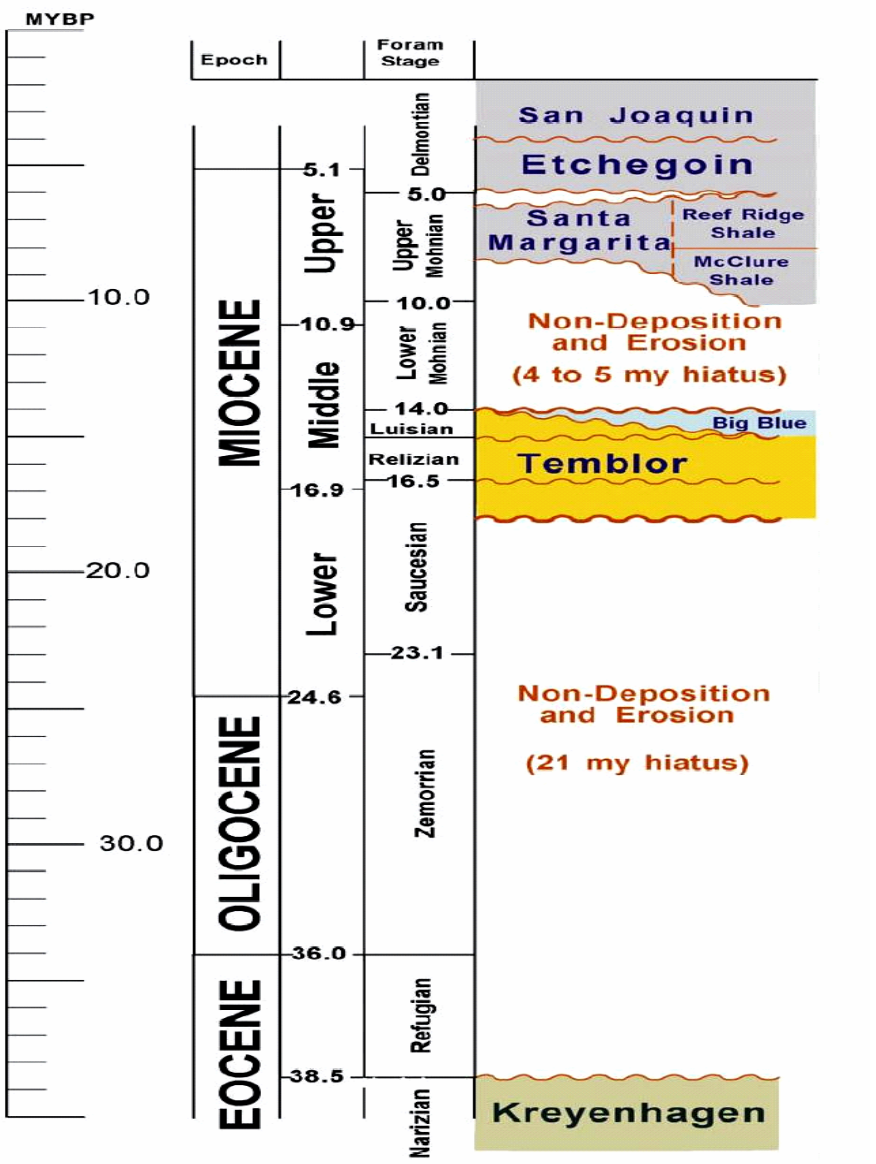

Figure 13. Stratigraphic section showing age relation and the magnitude of unconformities bounding the Temblor interval.

(Clark et. al., 2001a)

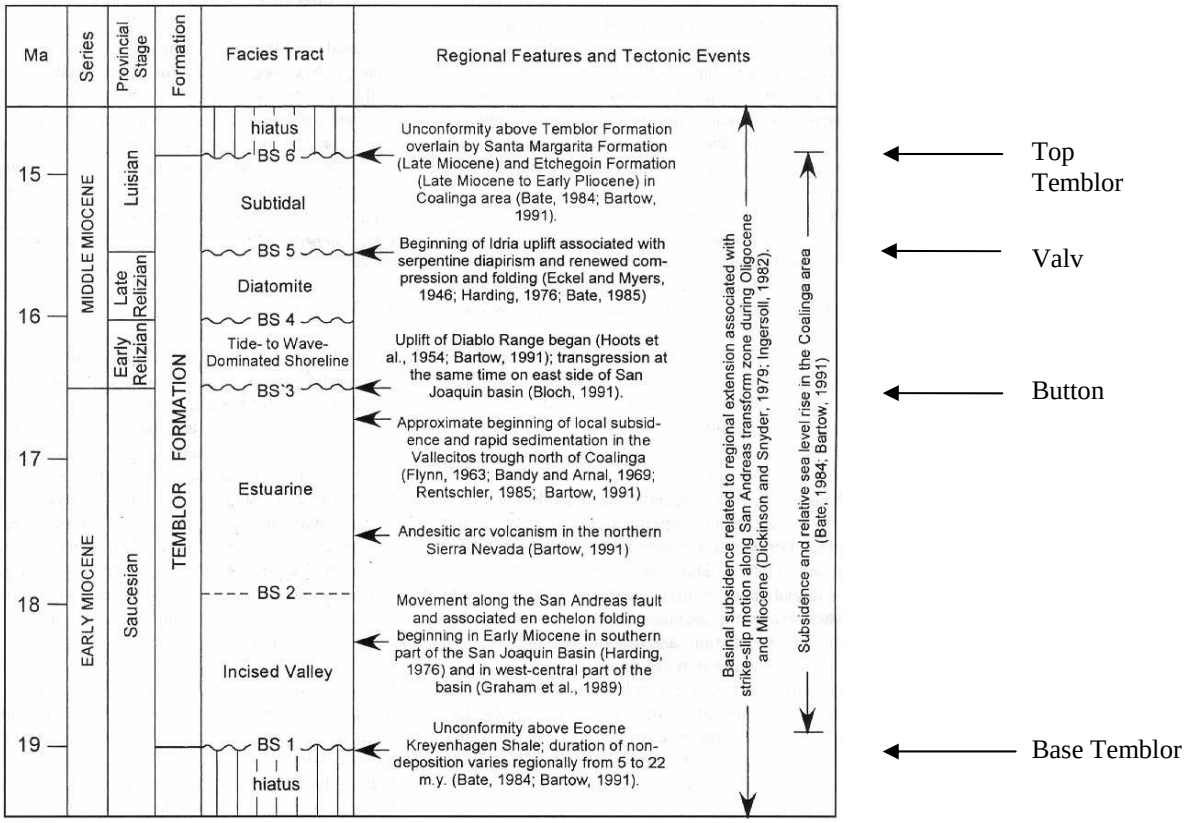

Figure 14. Origin of Temblor Formation facies tracts and bounding surfaces related to regional features and tectonic events from Bridges and Castle (2003). The equivalent positions of the four unconformities mapped with seismic resolution is shown in the extreme right.

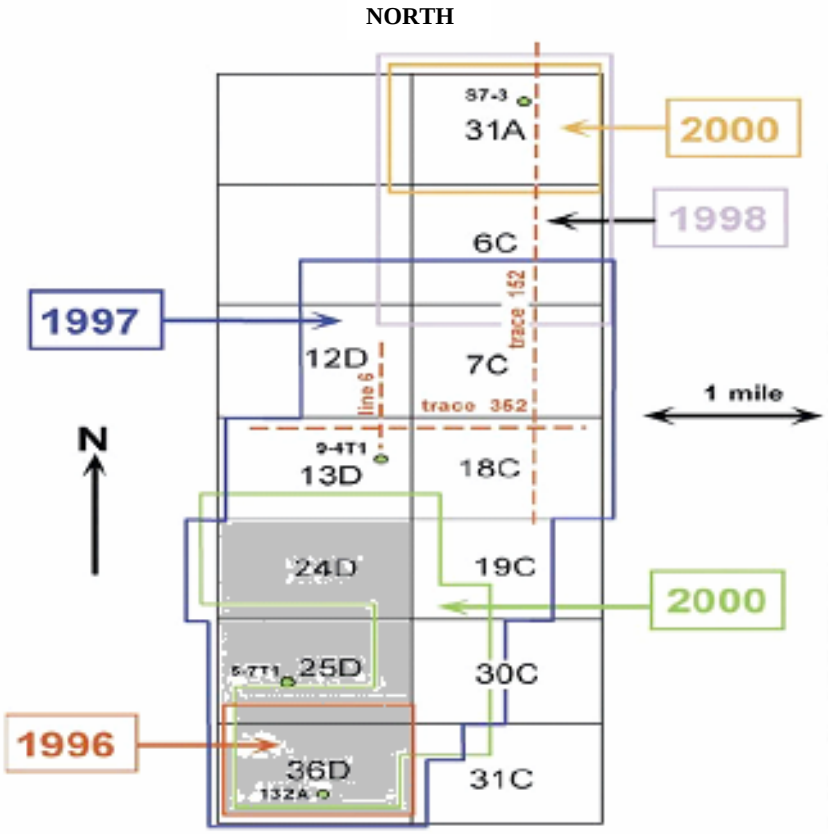

Figure 15. The locations of 3-D seismic surveys, and overlapping of successive 3-D surveys to provide 4-D coverage, in West Coalinga Field, from Peters, et al., 1994; Clark et al., 2000. The study area is shown as the shaded area in block 36D, 25D, and 24D and lies within the Domengine Ranch 7.5' quadrangle. The Temblor Formation out crops at about 1 Km. from the block 31A towards NE (Bridges and Castle, 2003).

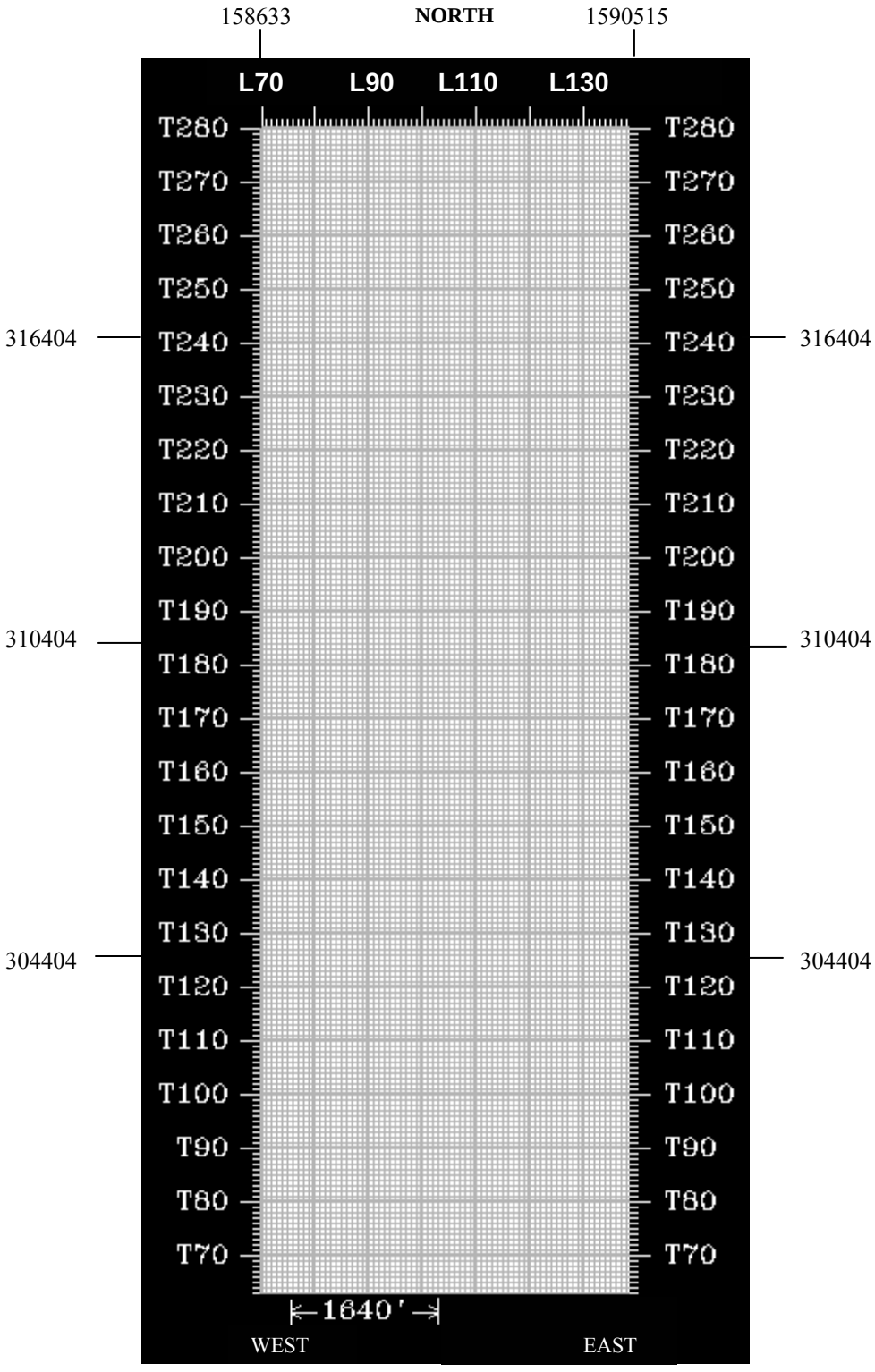

Figure 16. Location of lines (L) and traces (T) of the merged 3D seismic data set over the study area.

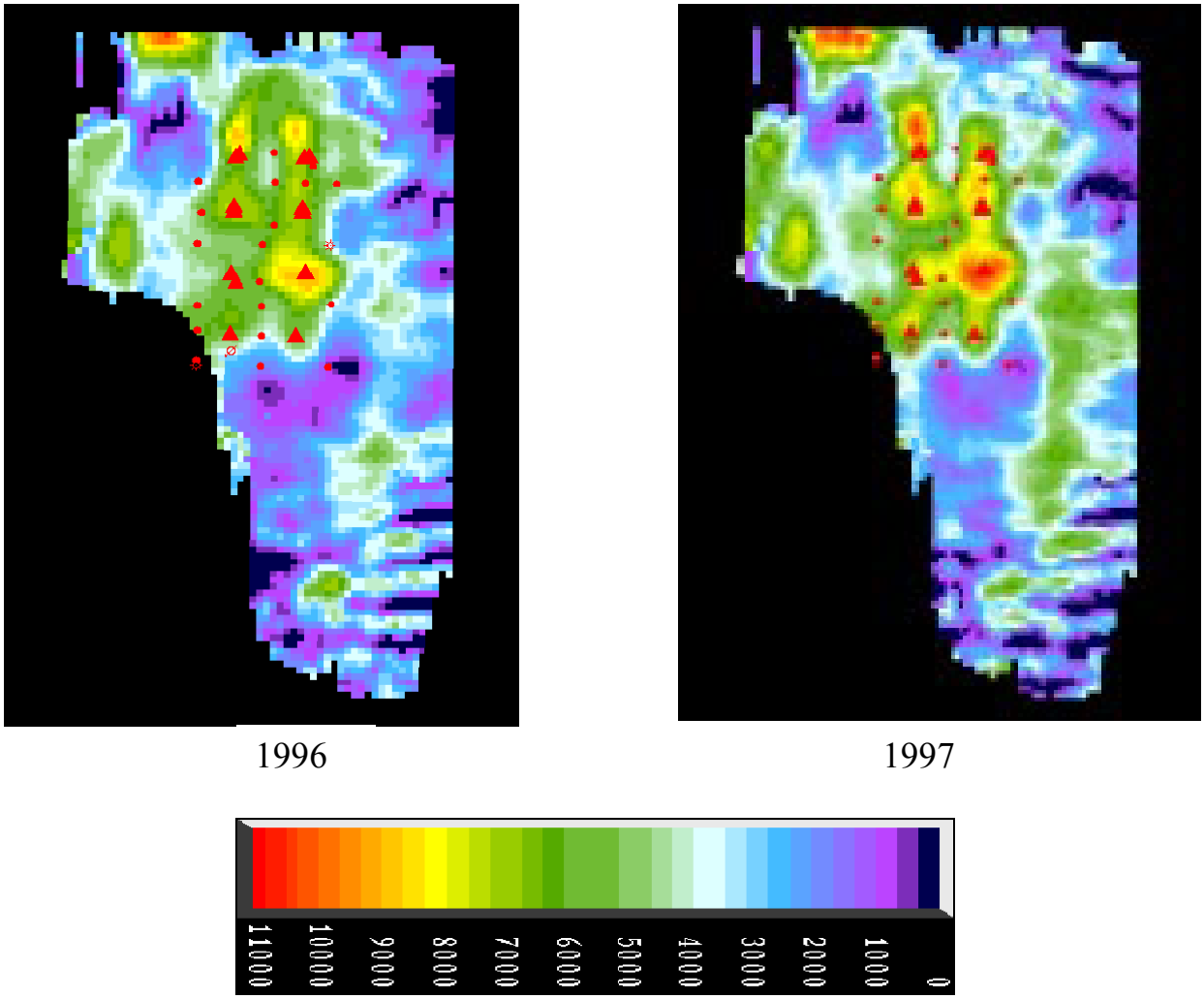

Figure 17. Amplitude picks from the top reservoir from the ’96 (left) and ’97 (right) seismic surveys. The triangles represent steam injectors, while the circles represent local pattern producer wells.

(after Ecker et al., 1999)

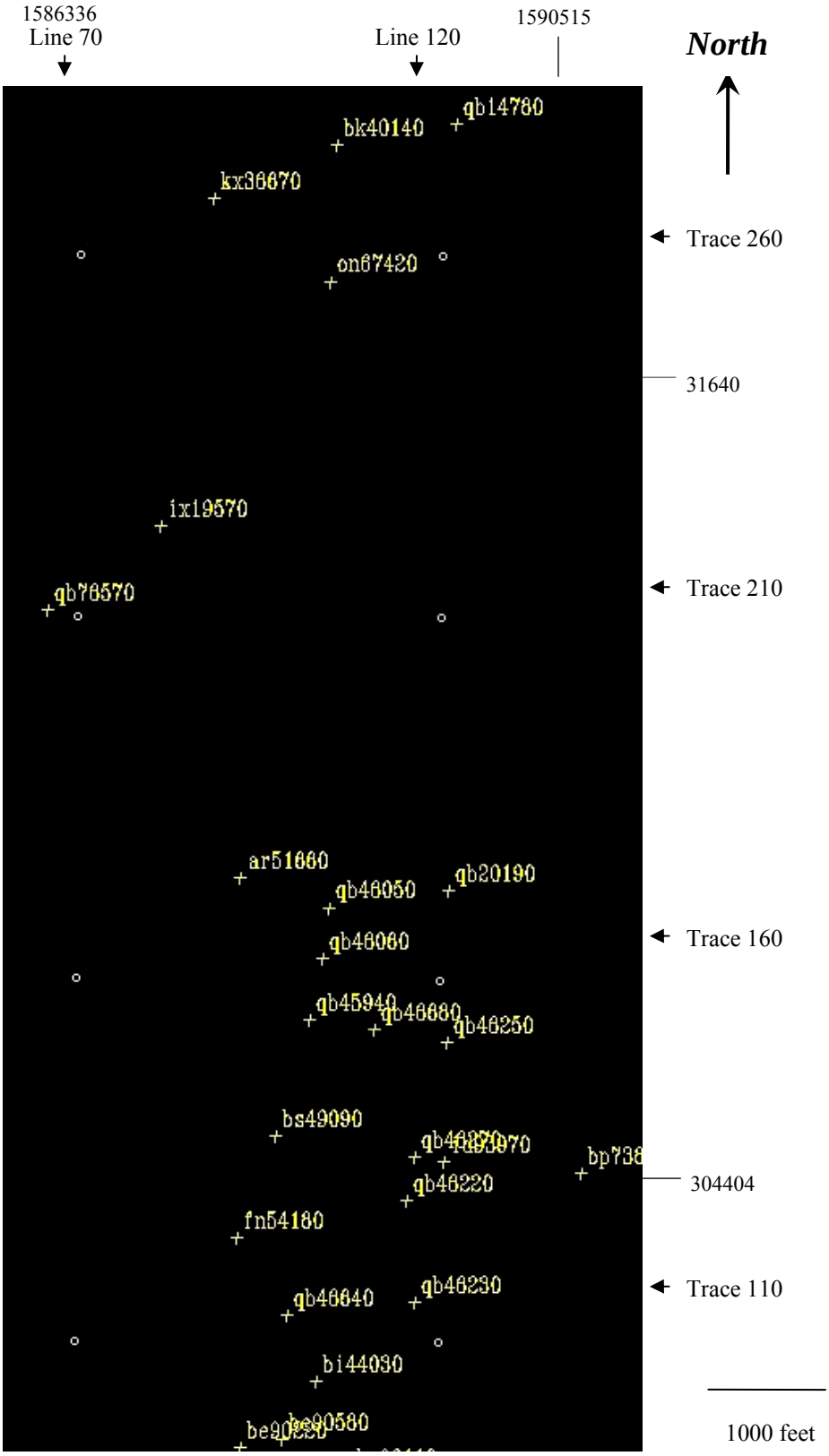

Figure 18. Well Locations showing trace and line grid points.

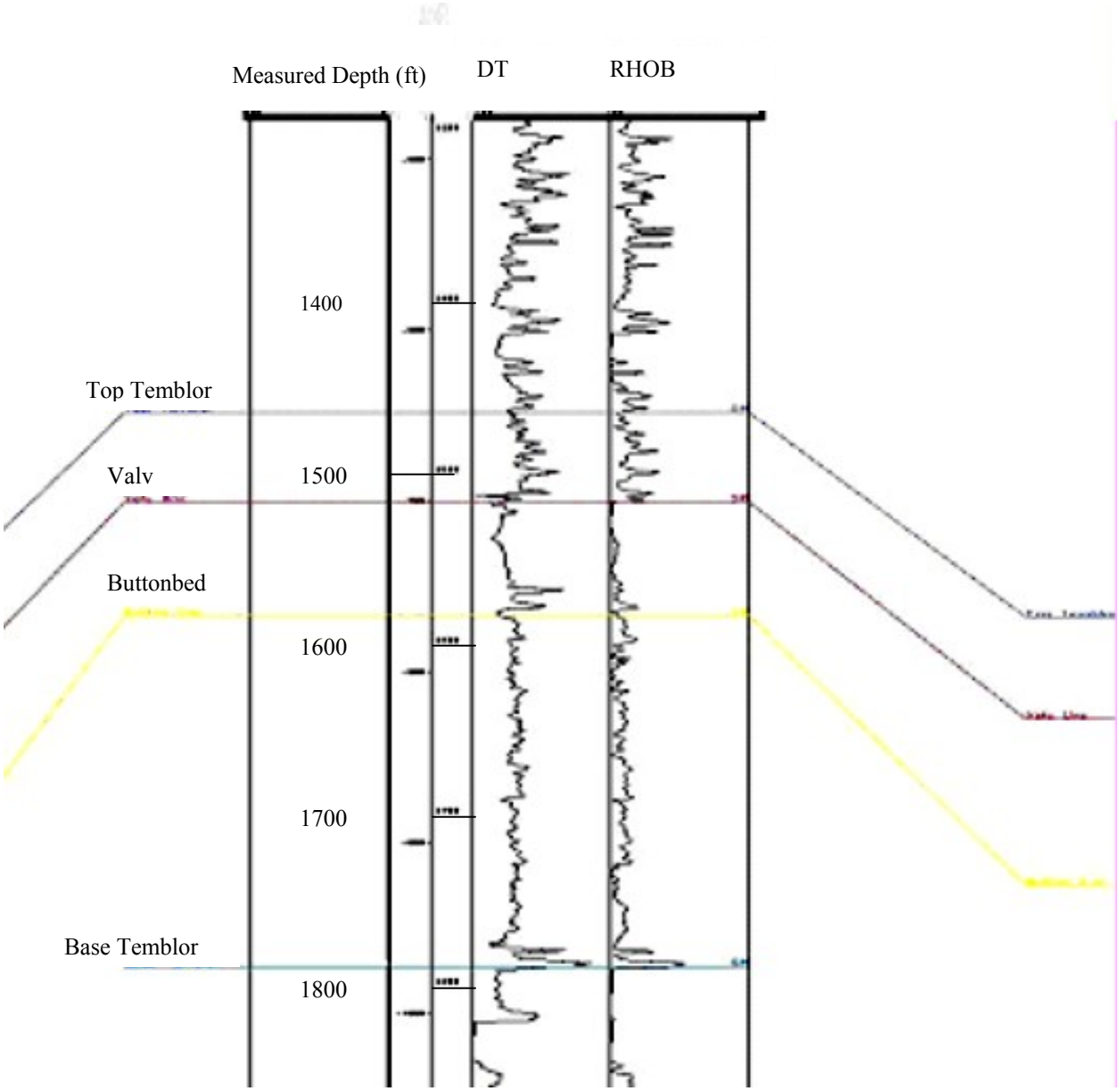

Figure 19. Wireline log characteristics of a Coalinga well.

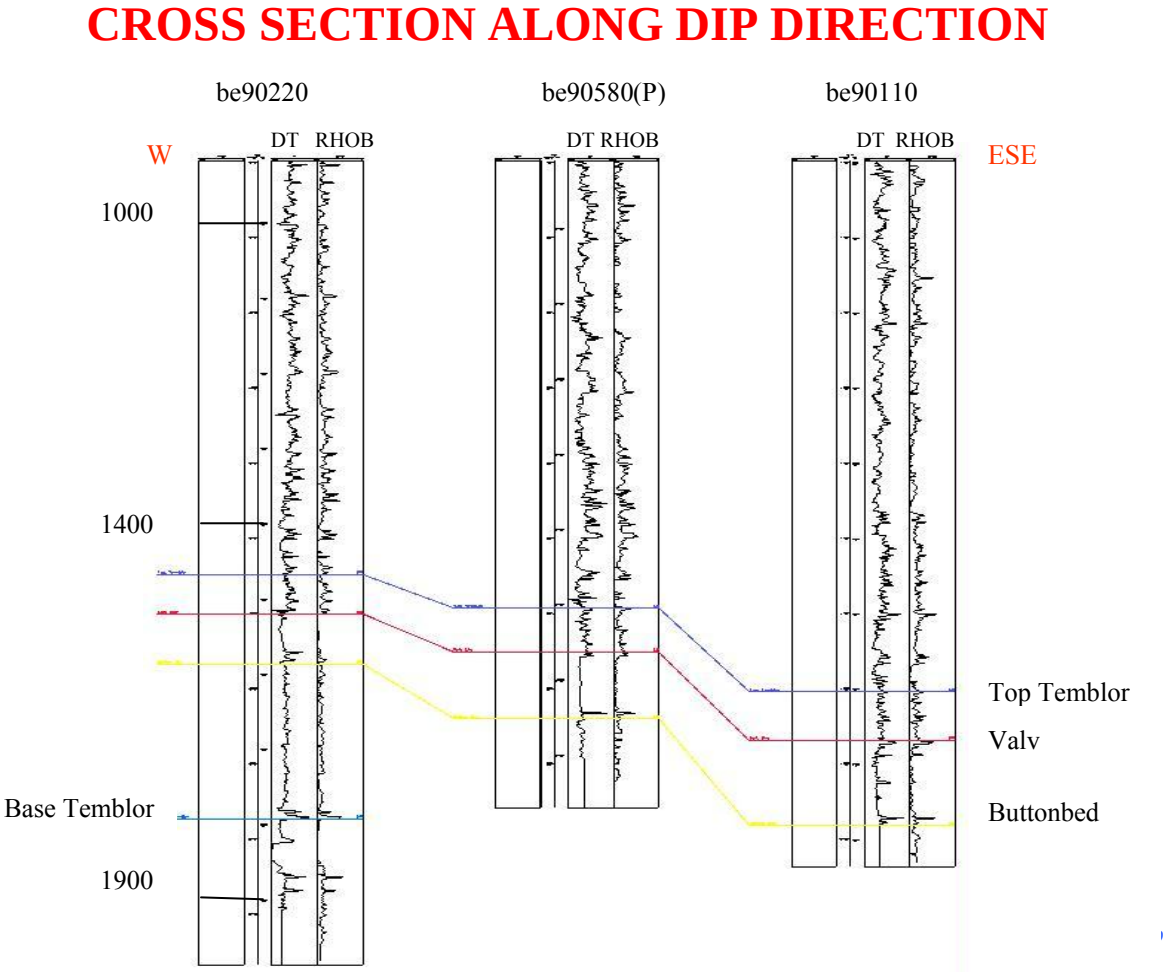

Figure 20. Wireline log correlation along dip direction of Coalinga Field. Well be90580 is projected

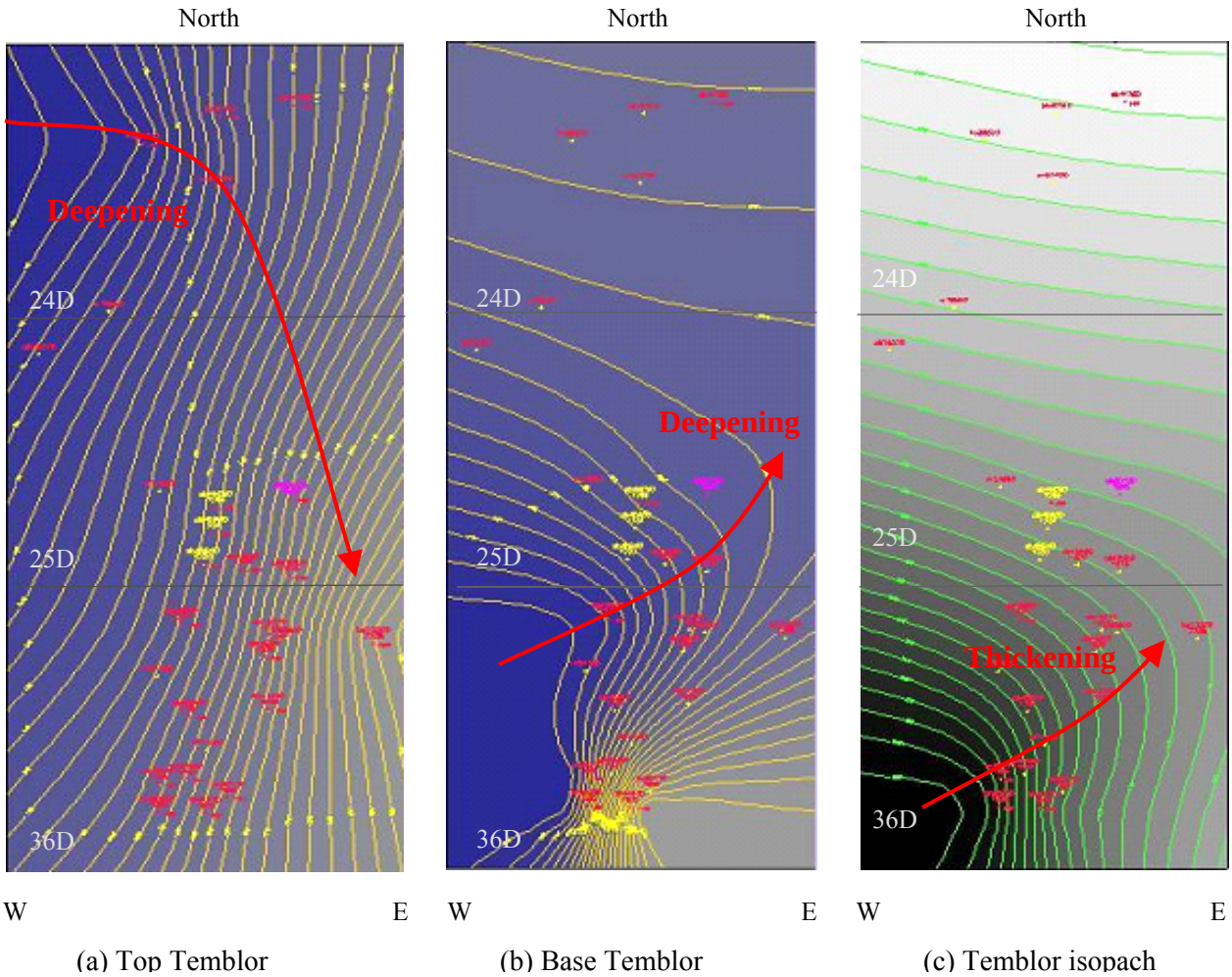

Figure 21. Structure and isopach (wireline depth) maps of the Temblor Formation. Structure map on the Top of Temblor (a) shows NNE-SSW strike and E-SE dip. The highest elevation is towards the NW corner. Structure map on the Base Temblor (b) shows higher elevation towards SW, thickening towards NE, lack of sufficient well data does not give a clear picture towards SE. The isopach map of the Temblor (c) shows decrease in thickness towards SW suggesting higher elevation for The Temblor in the SW part of the study area.

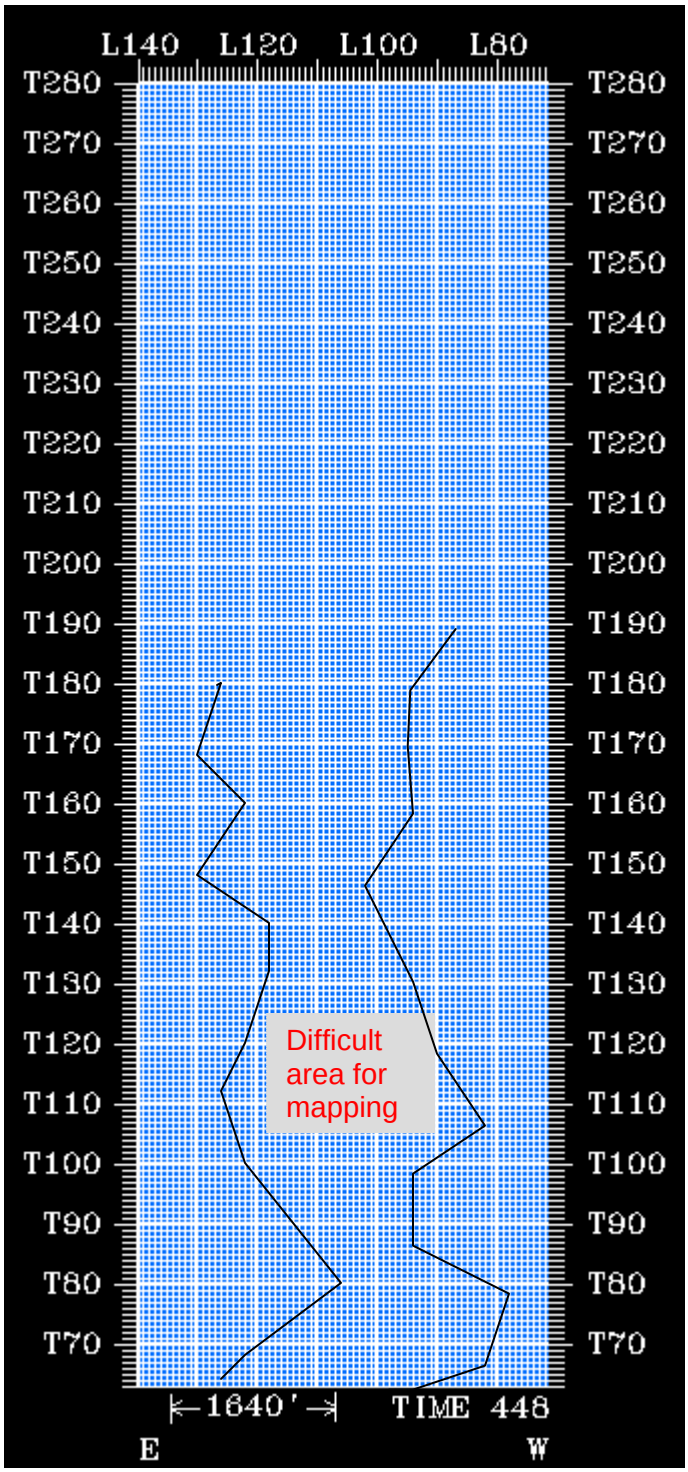

Figure 22. Seismic lines (L) and traces (T) profile showing difficult area for mapping the reflectors in the study area. The view is from subsurface to the surface.

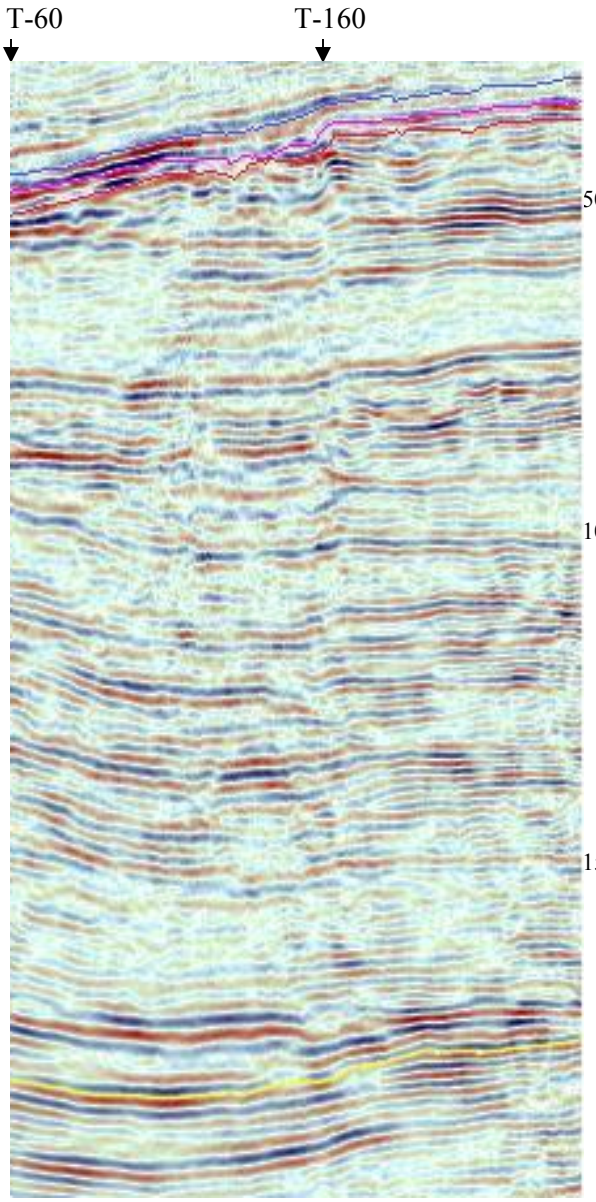

Figure 23a. Original line (L-90)

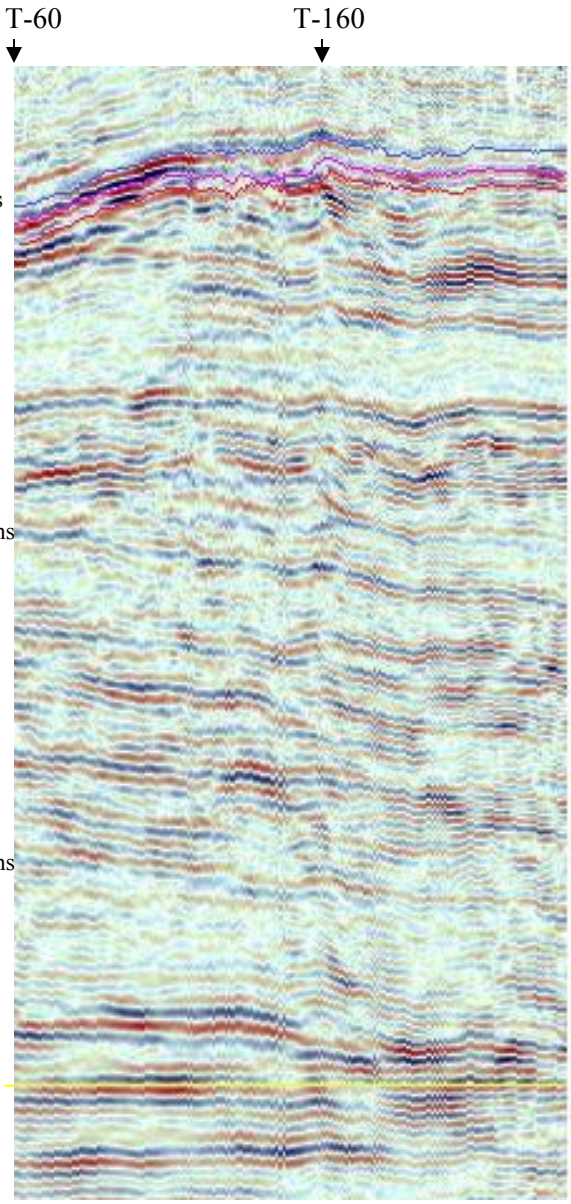

Figure 23b. Flattened L-90 (corrected), reflector flattened at the yellow horizon.
(after Mahapatra et al., 2003b)

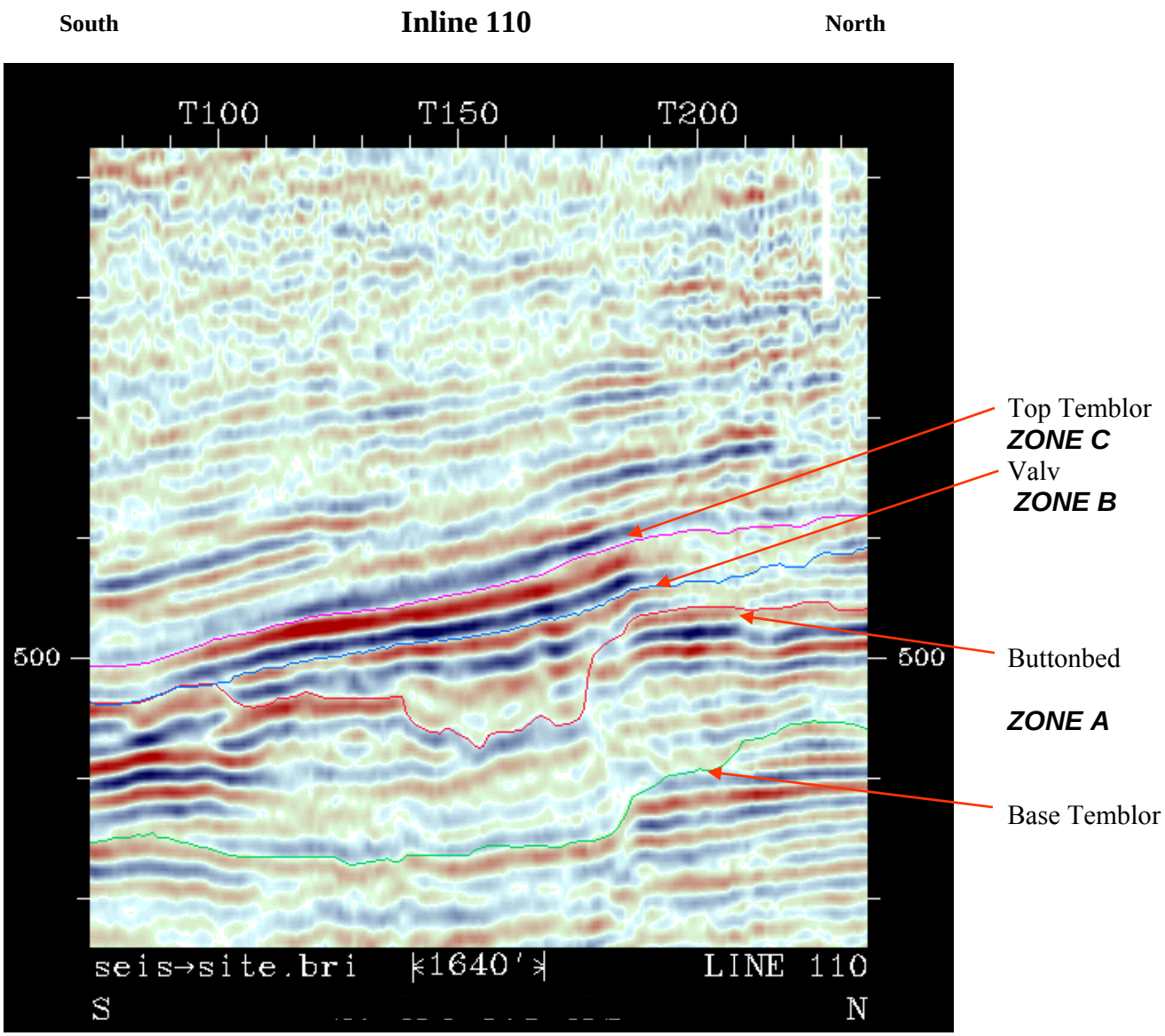

Figure 24. Unconformities and reservoir zones within the Temblor sequences (time in ms).

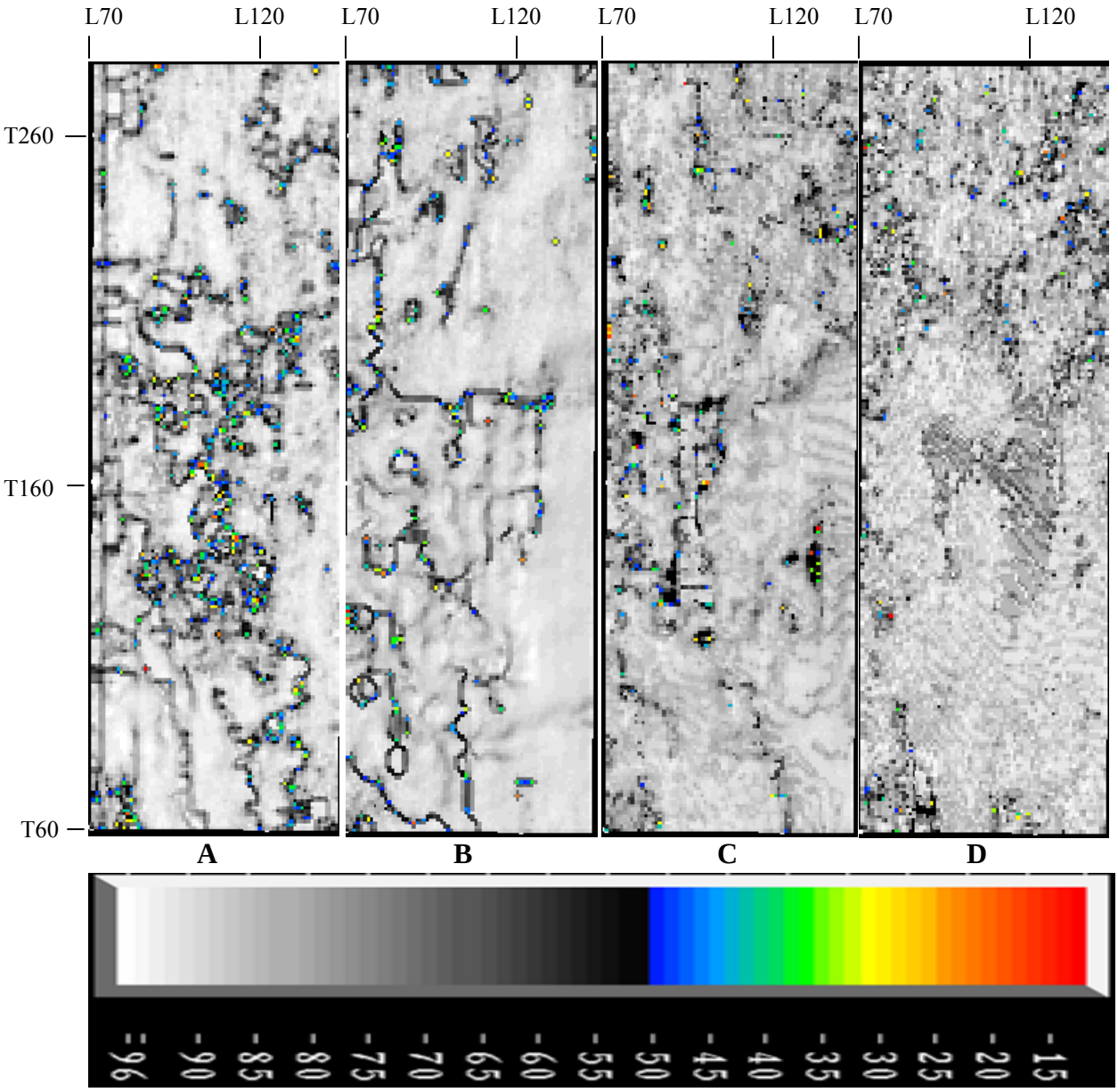

Figure 25. Confidence maps of tying reflector continuities in the Temblor Formation based on combined weightage of time shift (30%), amplitude value (40%), and wavelet width (30%). The degree of reliability percentage of tying the reflector shows the discontinuities. The confidence map of the on the Base Temblor (A) shows poor reflector continuities indicative of a pattern resembling channel-like discontinuity feature. Map on the Buttonbed (B) may be due to the paleotopography. Map on the Valv (C) shows discontinuities towards the west suggesting geological discontinuities. Map on the Top Temblor (D) indicates a minor difficulty towards the northern part of the area due to the presence of weak reflectors, caused for example by a lesser change in velocity contrast as demonstrated on the apparent polarity attribute volume (Figures 47 and 48).

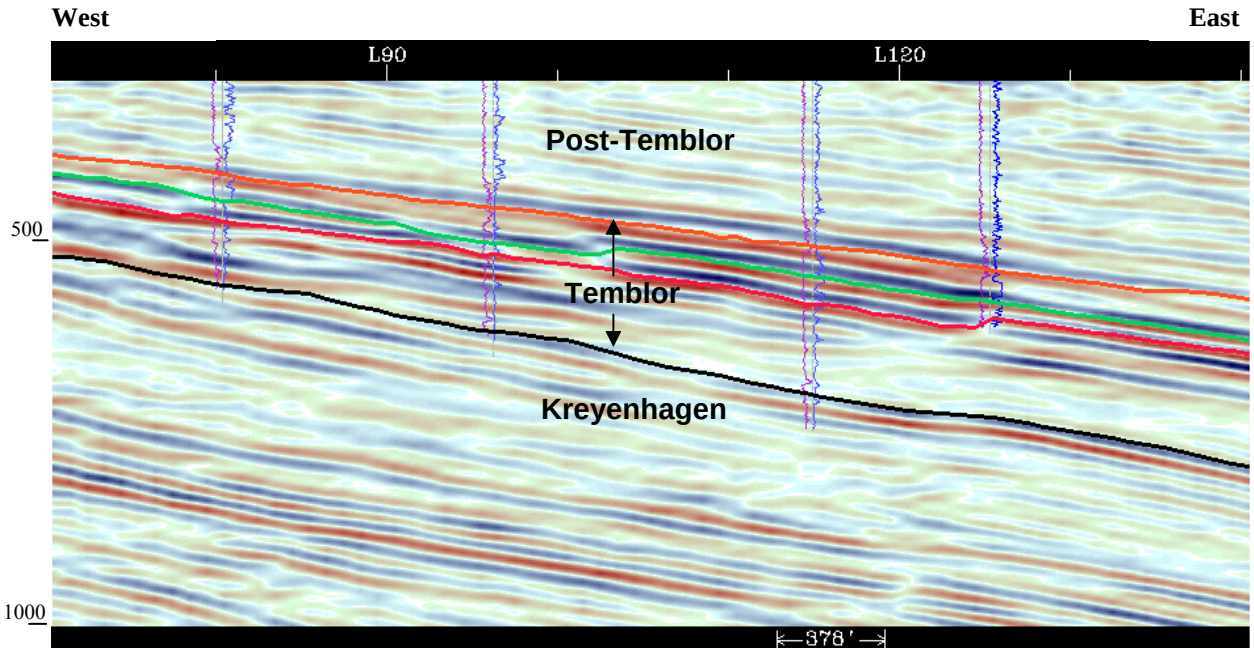

Figure 26a. Seismogeological section across the study area (Trace-170). GR (purple) and DRES (blue) values increase from left to right. Wireline logs are offset by 450 feet. Time in ms

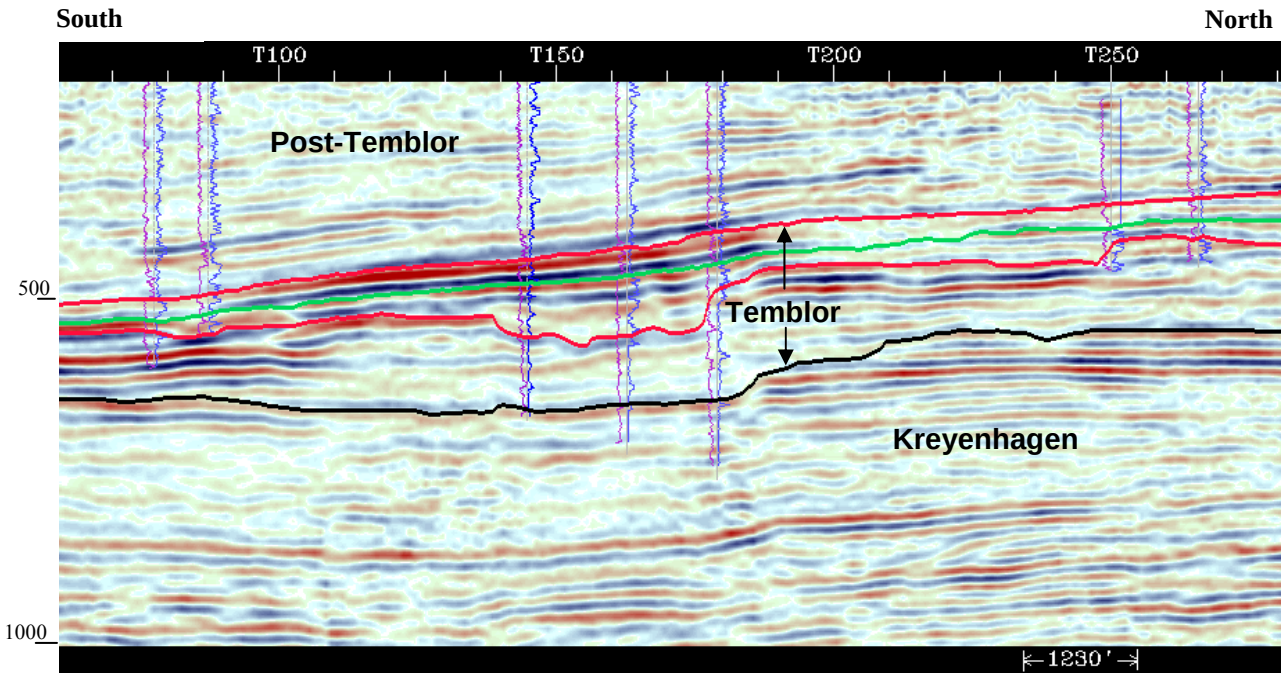

Figure 26b. Seismogeological section along the study area (Line-110). GR (purple) and DRES (blue) values increase from left to right. Wireline logs are offset by 150 feet. Time in ms

Trace 255

West **East**

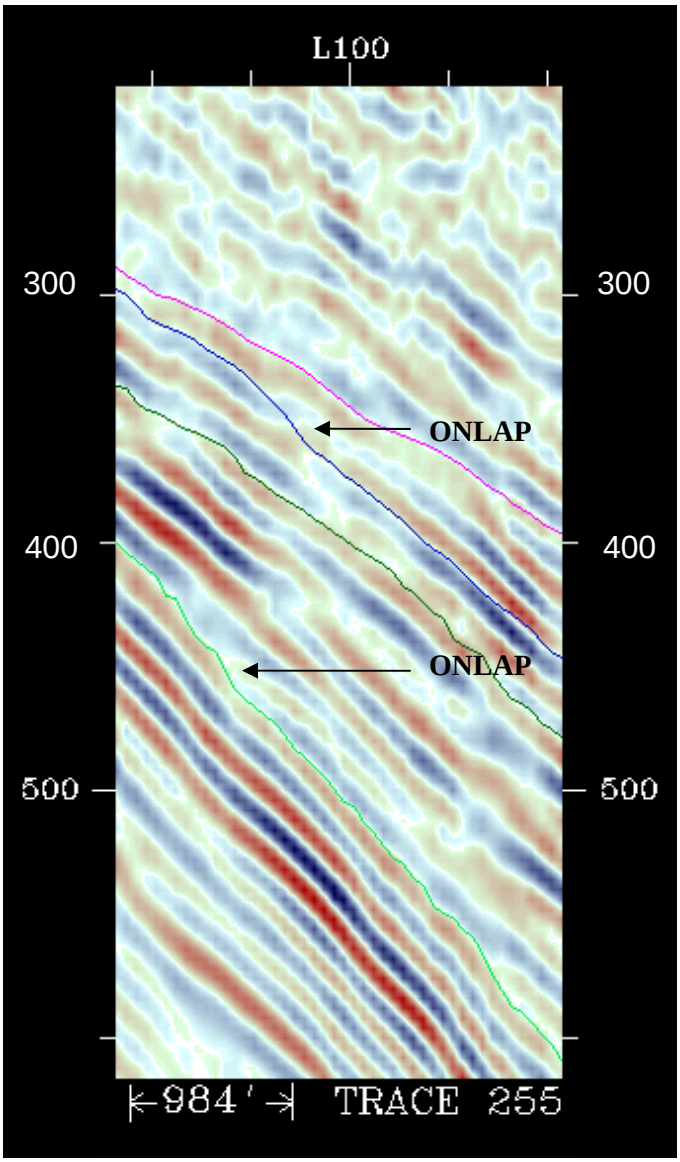

Figure 27. Shows onlap of reflectors. The light green, dark green, blue, and red colors represent the Base Temblor, Buttonbed, Valv, and Top Temblor unconformities respectively (time in ms).

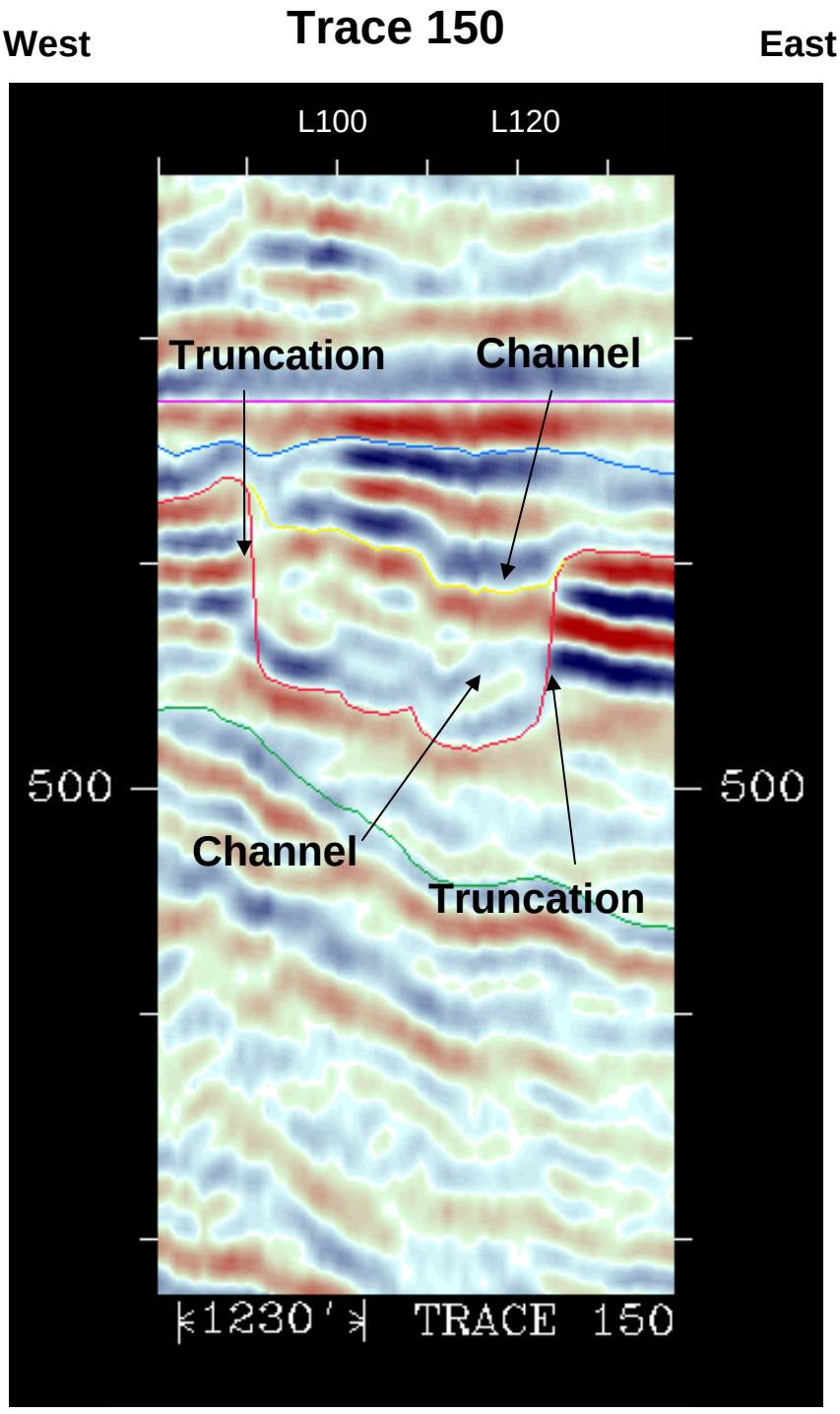

Figure 28. Trace section flattened at the Top of Temblor showing reflector truncations and channel shape in between the Buttonbed (red) and Valv (blue) unconformities. An isochron map of the channel feature (red to yellow) is presented in the Figure 37.

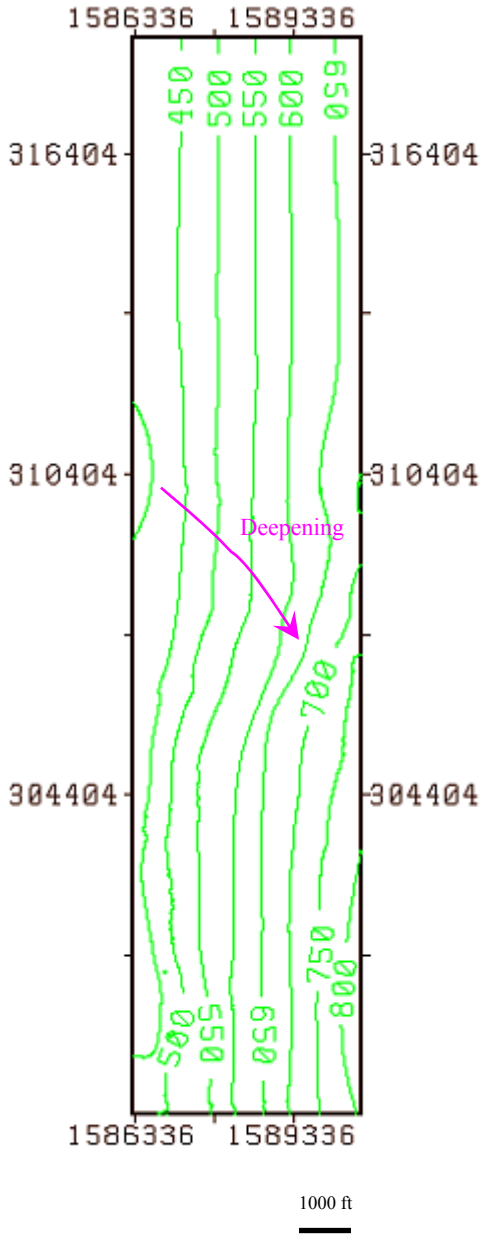

Figure 29. Structure contour map on top of the Base Temblor unconformity showing gradual deepening of the Unconformity towards E-SE. The Base Temblor is shallowest in the middle western part of the study area (contour interval 50 ms).

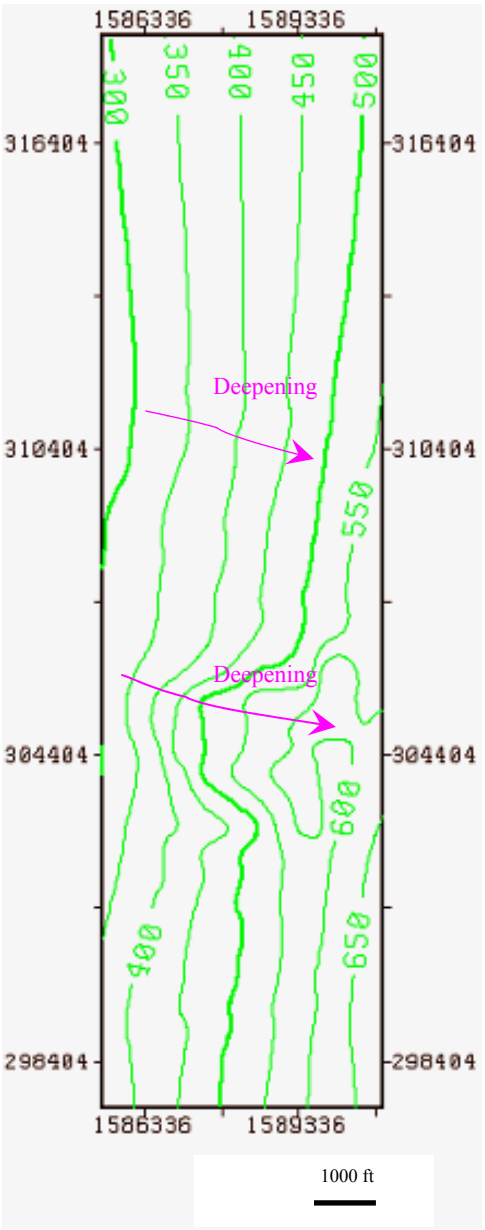

Figure 30. Structure contour map on top of the Buttonbed unconformity showing deepening trends towards east (contour interval 50 ms).

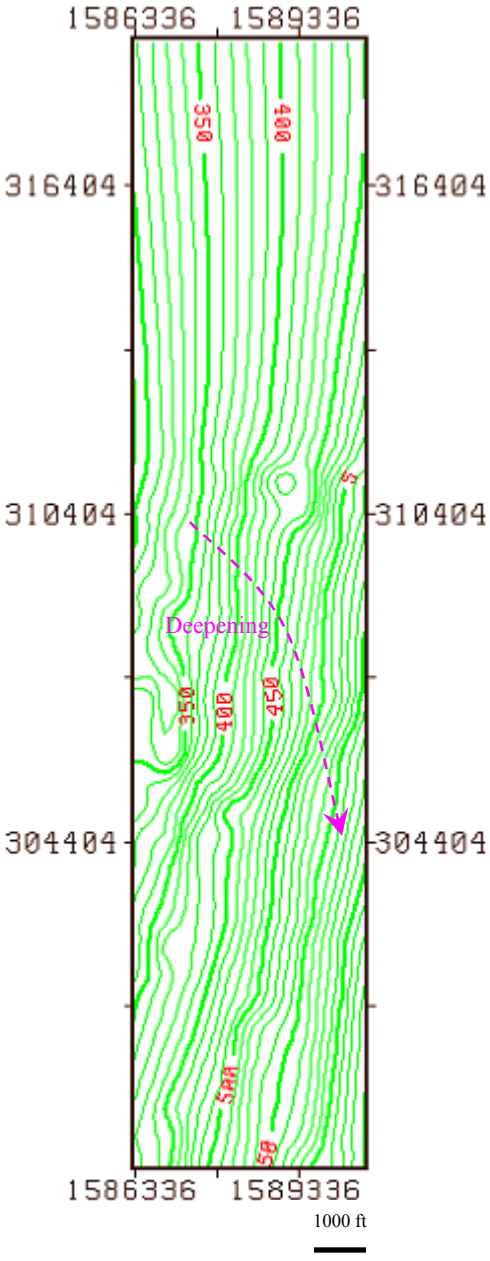

Figure 31. Structure contour map on top of the Valv unconformity showing generic deepening towards SE (contour interval 10 ms). The Valv is shallower towards the western part of the study area.

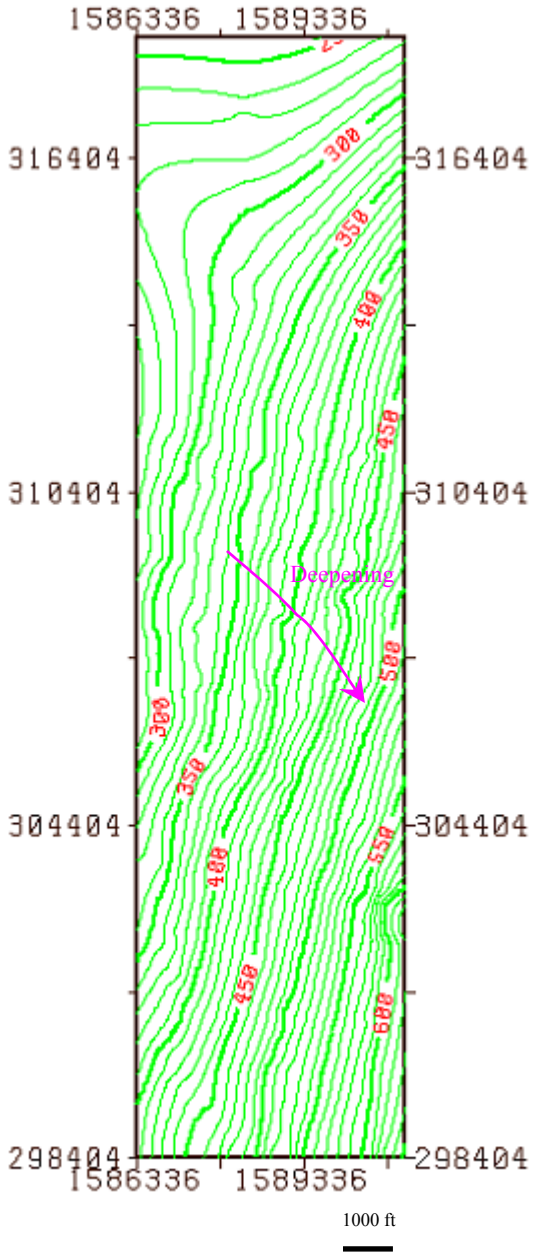

Figure 32. Structure contour map on top of the Top Temblor unconformity showing deepening trend towards SE (contour interval 10 ms). The surface is shallowest in the NW.

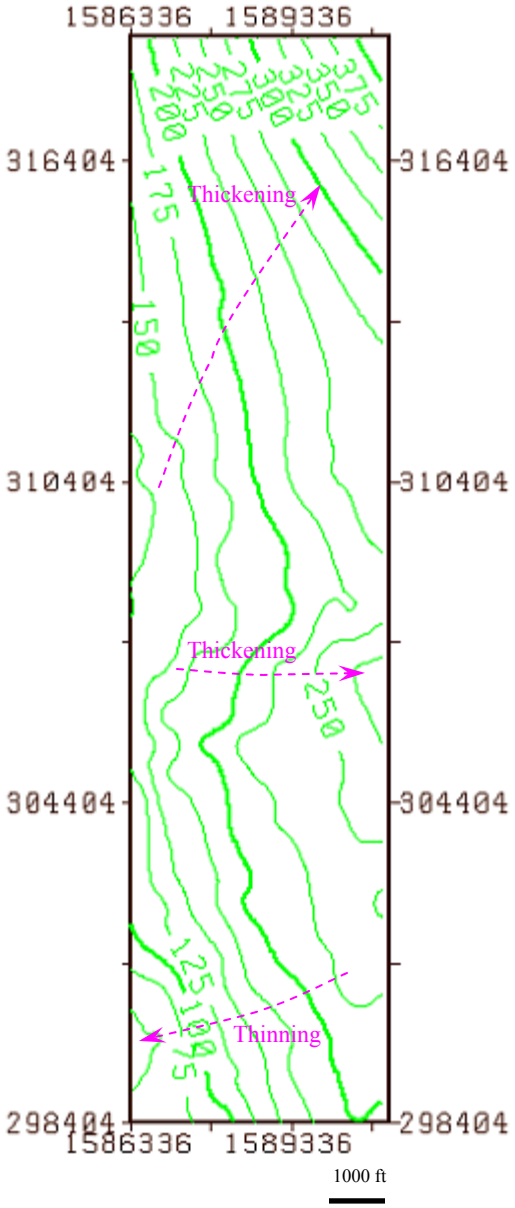

Figure 33. Isochron map between the Base Temblor and the Top Temblor unconformities showing the TWT thickness of the Temblor Formation (contour interval 25 ms).
The Temblor is thickest towards the NE corner and thinnest in the SW corner. An increasing trend of thickness (lobe) is also observed in the middle eastern part of the study area.

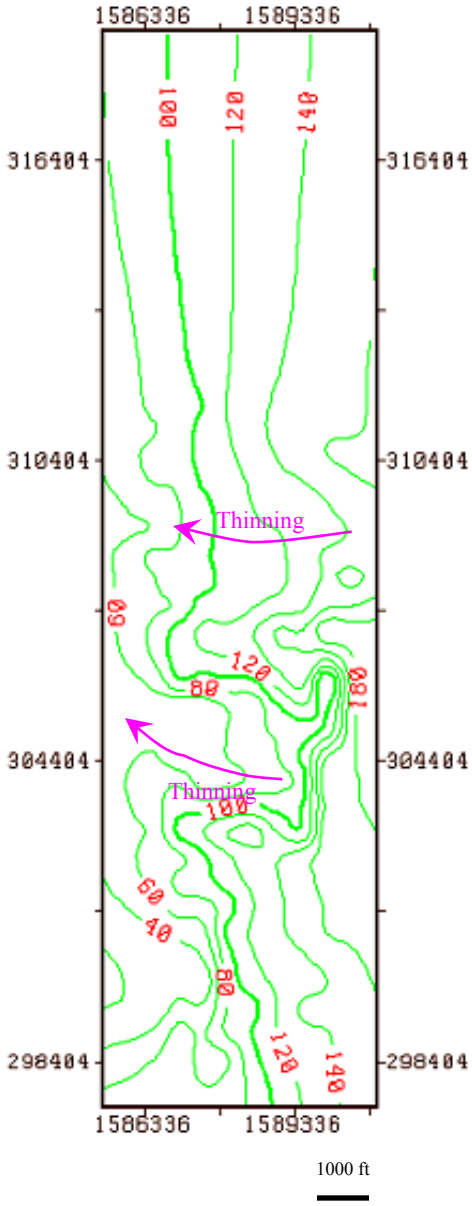

Figure 34. Isochron map between the Base Temblor and Buttonbed unconformities (contour interval 20 ms). The isochron gradually thickens towards the east. Two relatively less steeper thinning trends (wider spaced contours) are observed in the central part of the area of study.

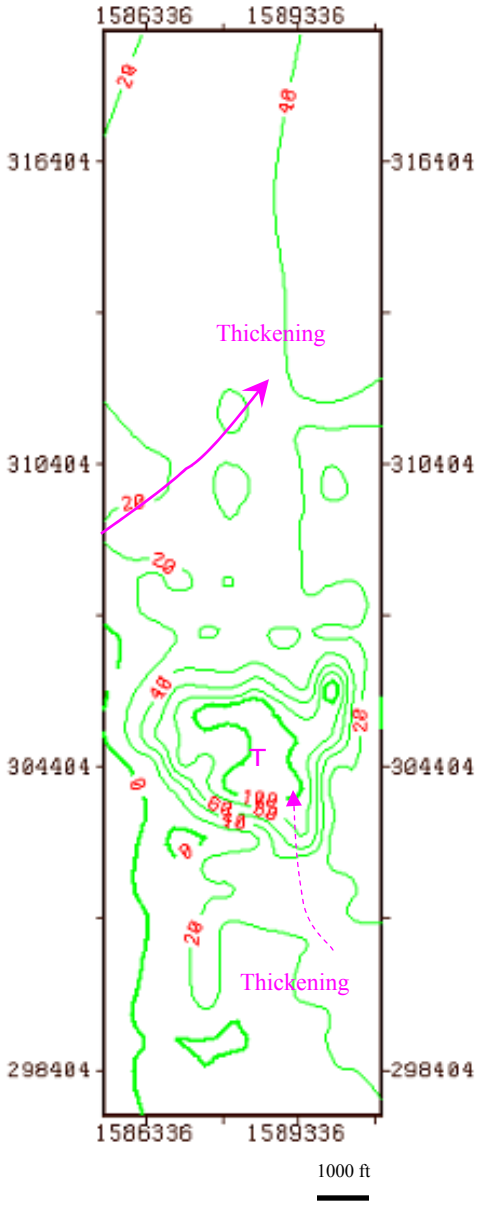

Figure 35. Isochron map between the Buttonbed and the Valv unconformities (contour interval 20 ms). The isochorns thicken towards the NE in the northern part of the study area. In the middle of the southern part, the thickest isochrons are observed (T).

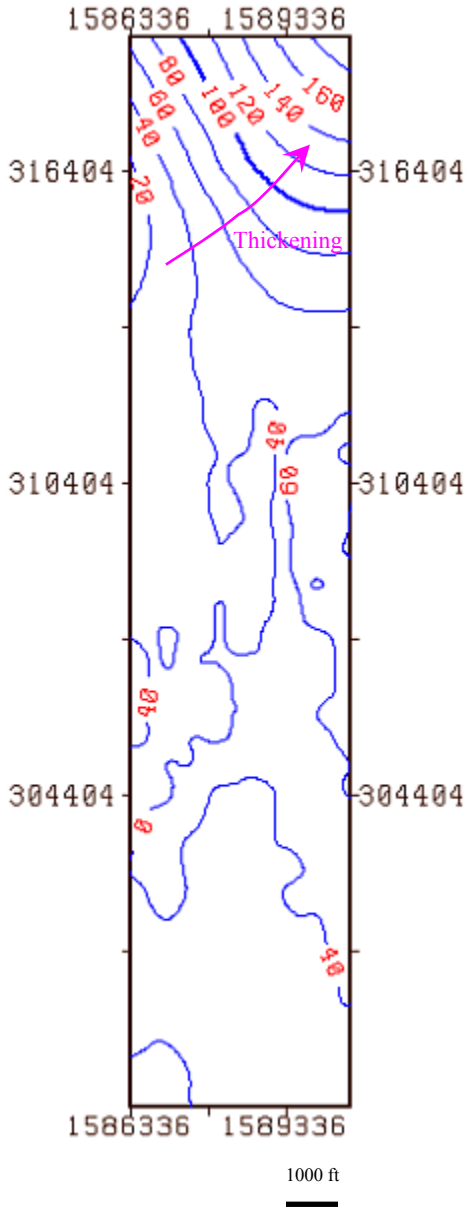

Figure 36. Isochron map between the Valv and the Top Temblor unconformities showing thickening towards the NE (contour interval 20 ms).

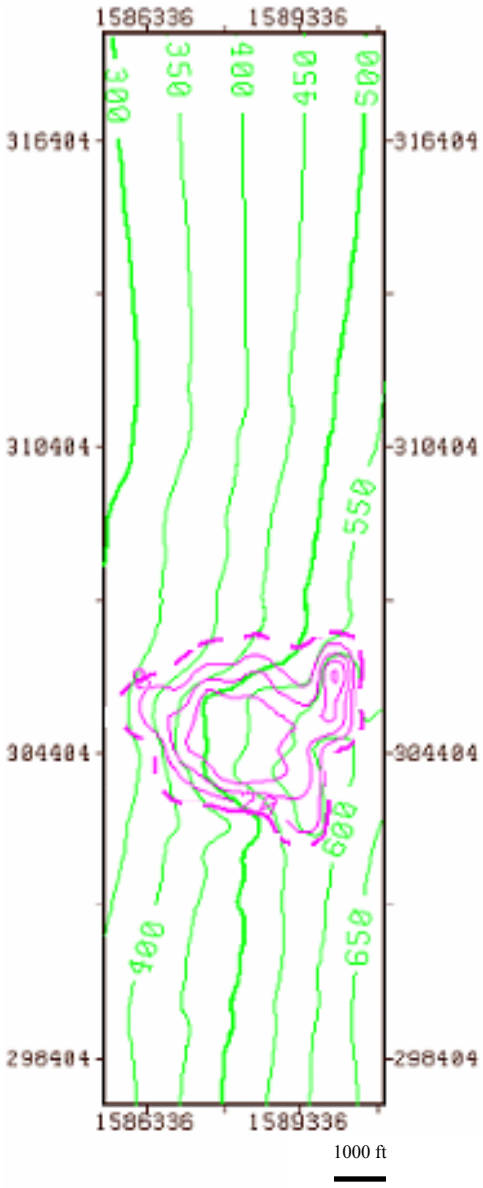

Figure 37. Overlay of isochrons of channel feature of Figures 24 and 28 (pink, contour interval 20 ms) and the structure contour map on the top of the Buttonbed unconformity (green). The zero contour is shown as dashed due to uncertainty in mapping the lateral extent on the low resolution seismic.

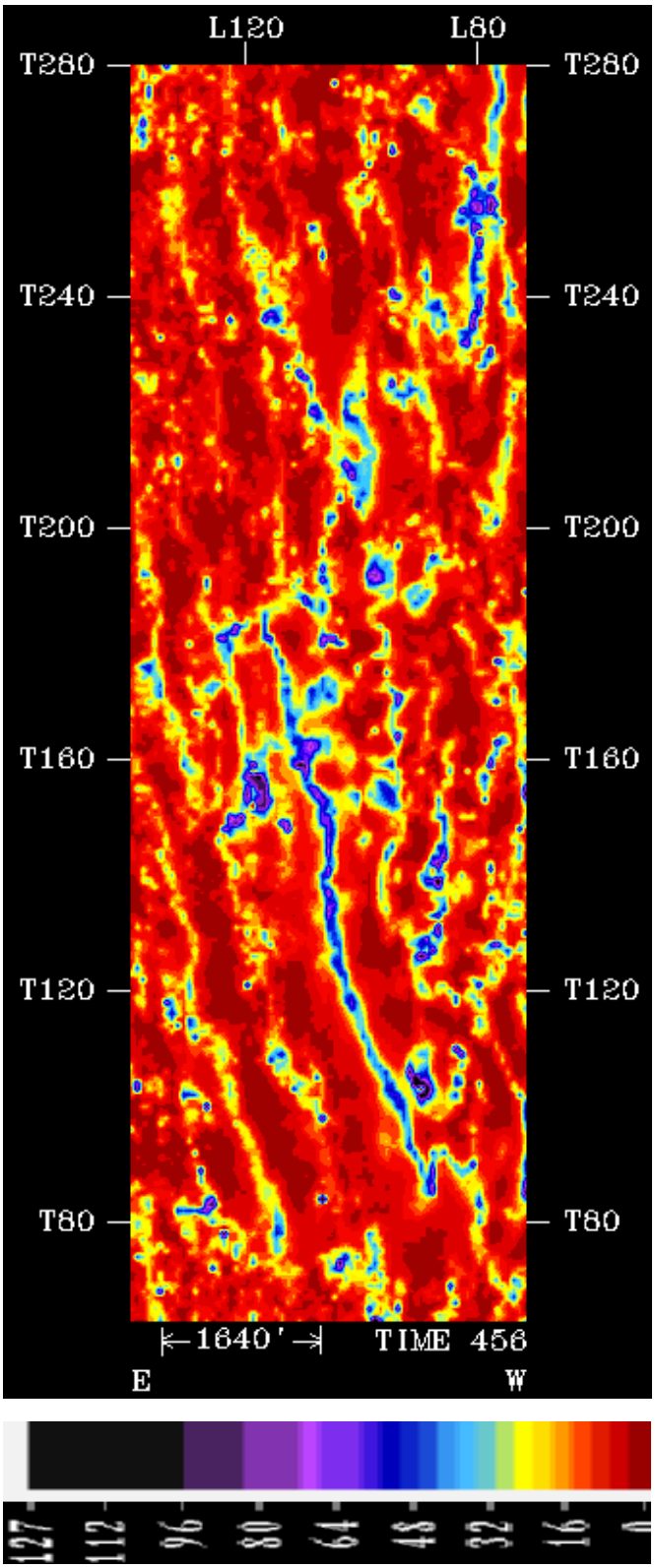

Figure 38. Coherency time slice at 456 ms showing sinuous channel like discontinuities (blue) in the Temblor Formation (looking from subsurface).

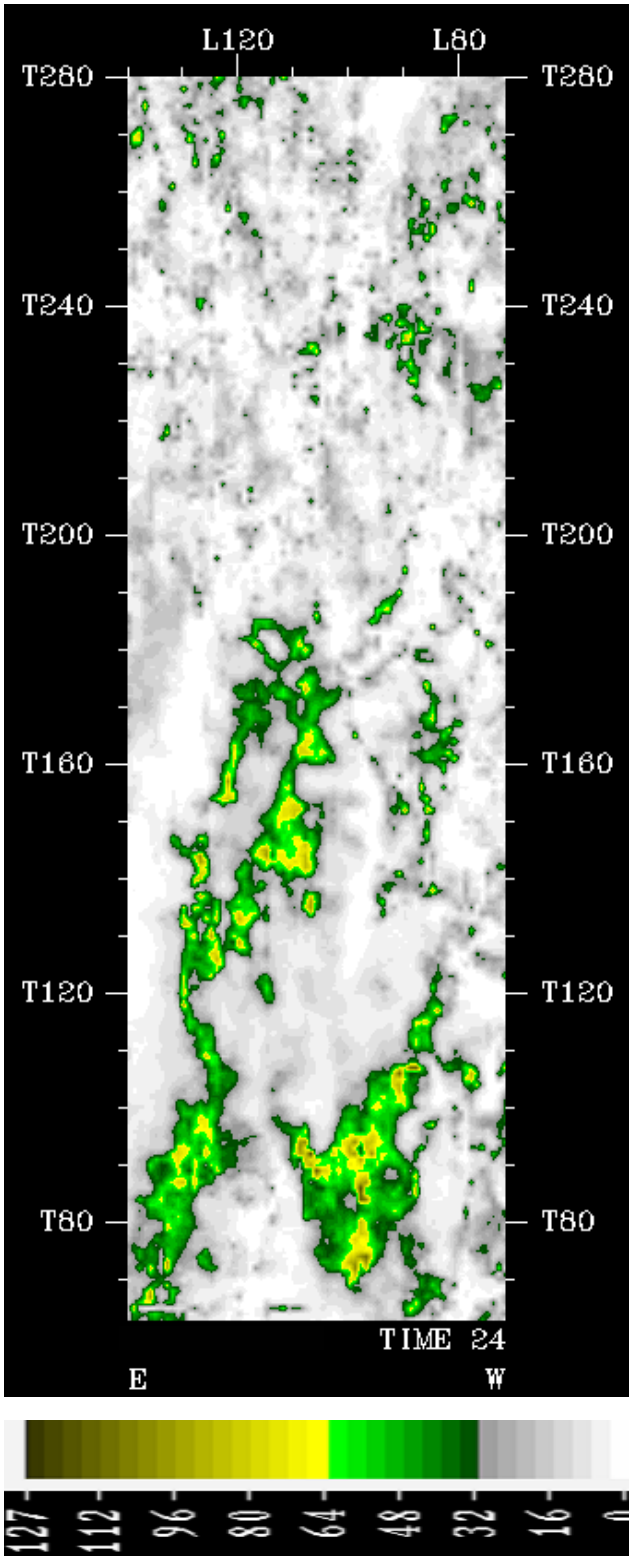

Figure 39. Coherency time slice at 24 ms from a volume flattened at the Top Temblor. Note the sinuous channel like discontinuities (yellow and green) in the lower part of the area (looking from subsurface).

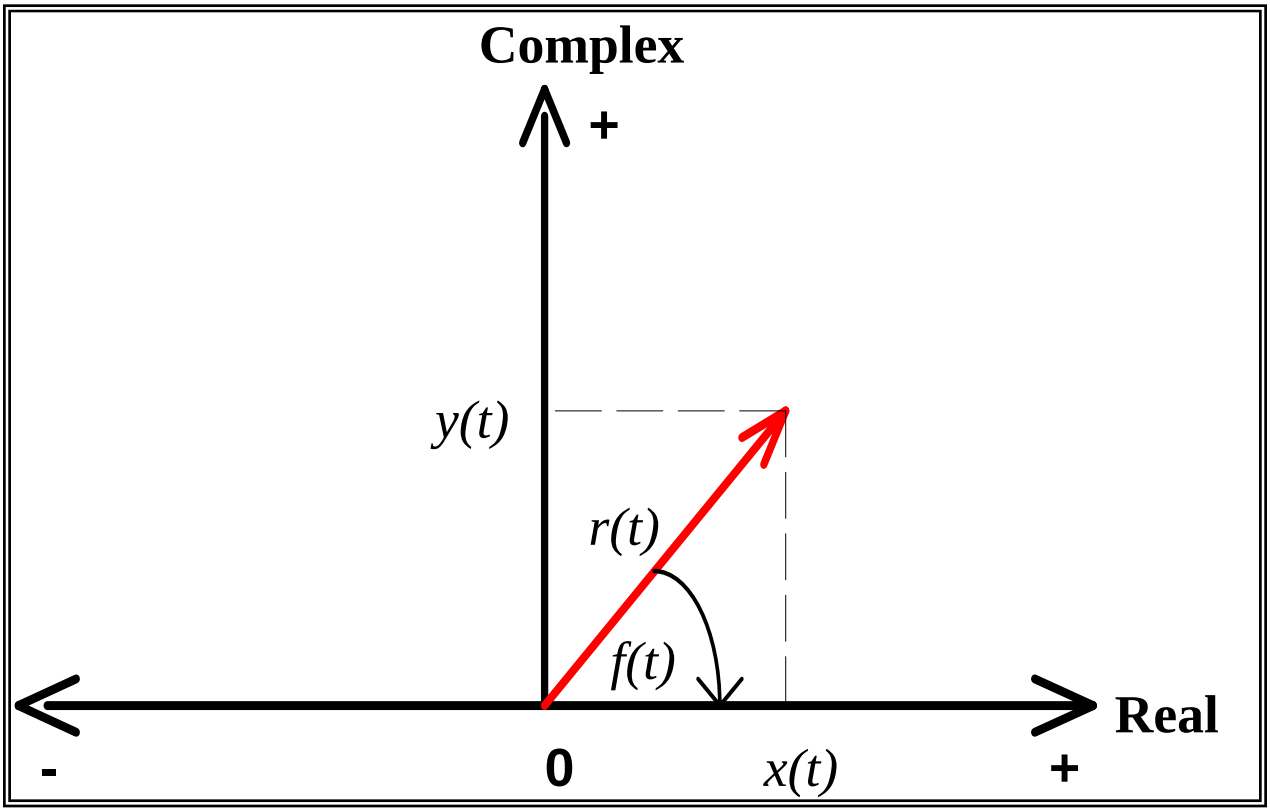

Figure 40. Cartoon showing relationship between instantaneous amplitude and phase in a complex trace

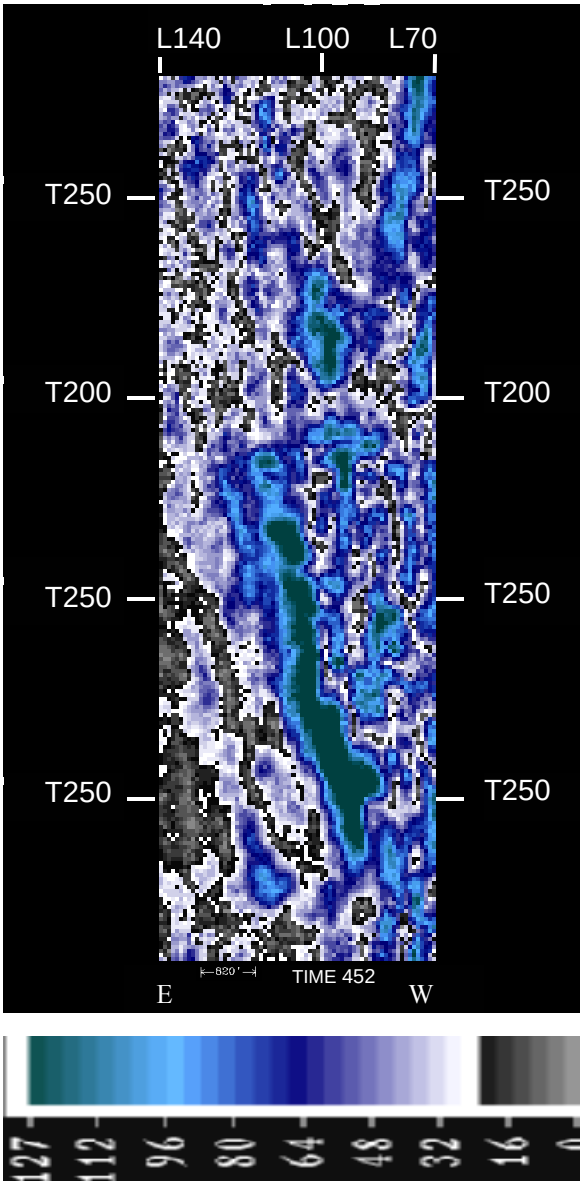

Figure 41. Time slice of instantaneous amplitude at 452 ms in the Temblor Formation. The high amplitudes (dark green) show sinuous feature which shift SE with depth. (looking from subsurface)

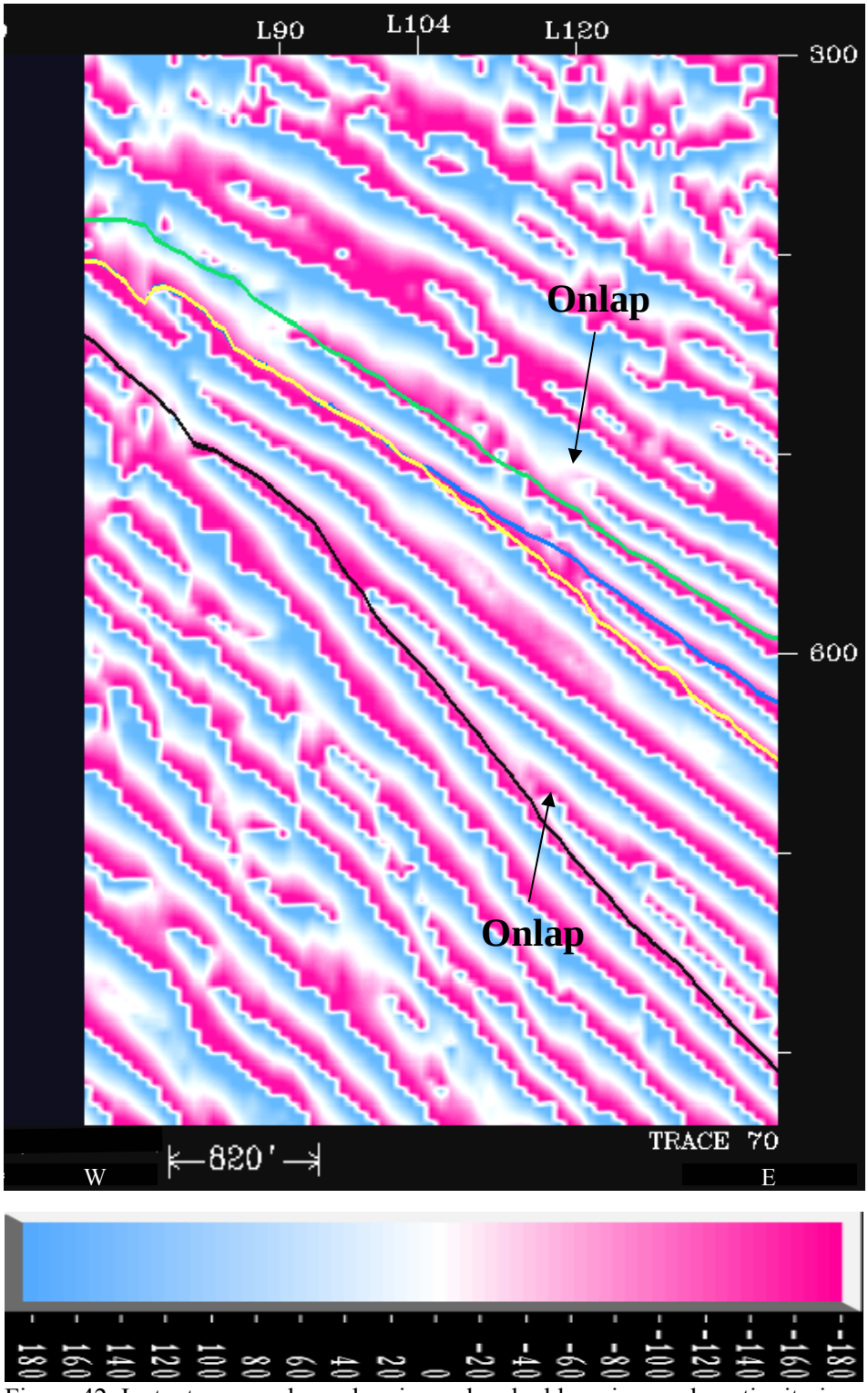

Figure 42. Instantaneous phase showing onlap, bed layering, and continuity in the Temblor Formation. Black (Base Temblor), yellow (Buttonbed), blue (Valv) and green (Top Temblor). Note the merging of the Valv and Buttonbed unconformities (line-104).

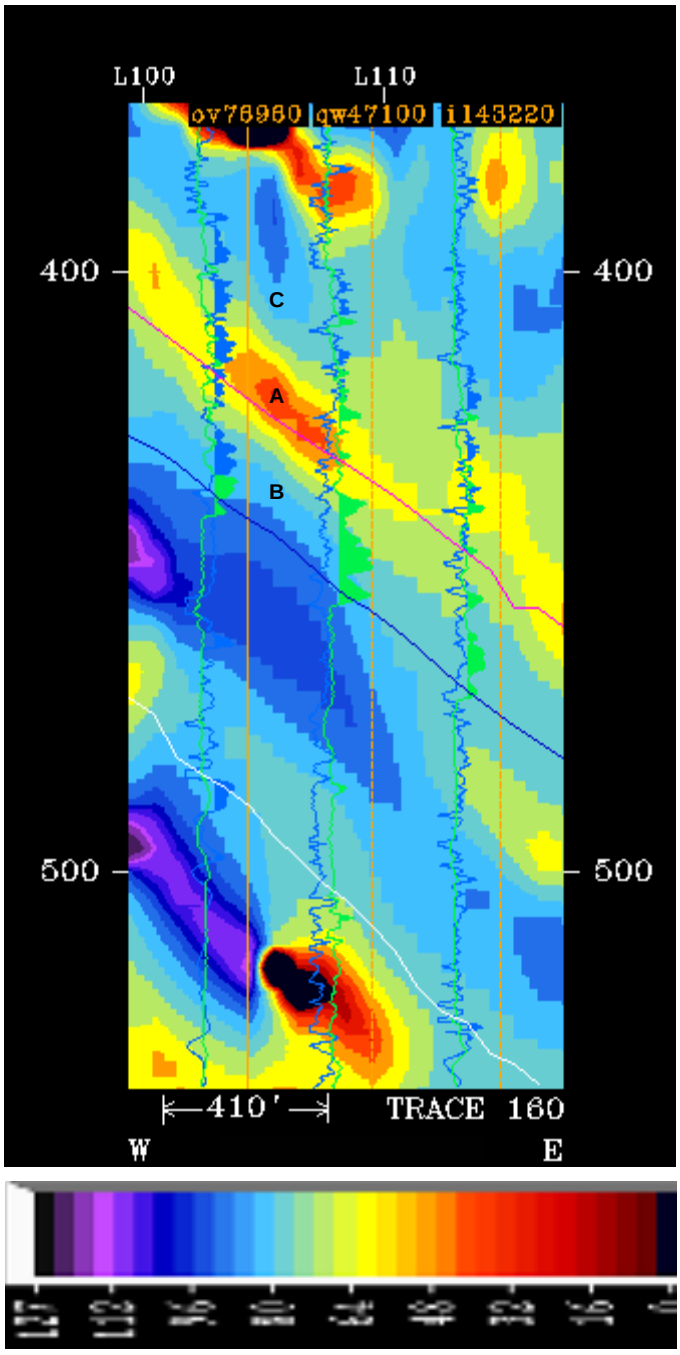

Figure 43. A trace section of instantaneous frequency showing low frequency zone (A) over a high gamma-sand in well qw47100 (B). GR is green and CNL porosity is blue. The low frequency zone may probably due to the effect of steam leakage into the overlying porous horizon (C).

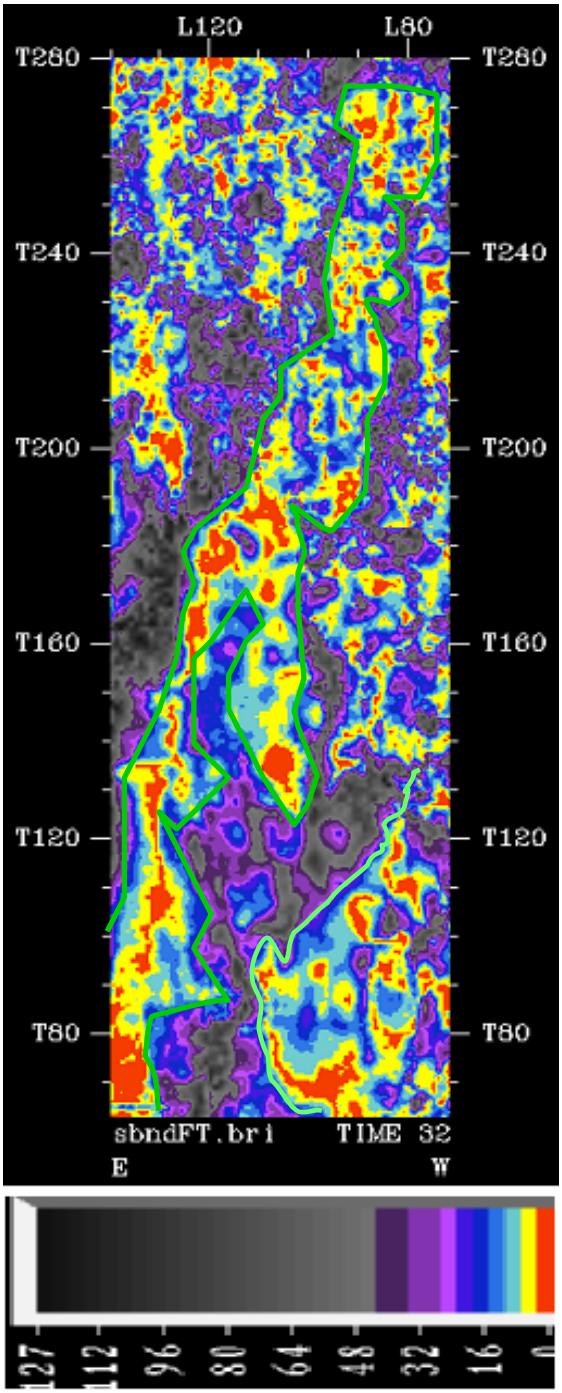

Figure 44. A time slice of instantaneous bandwidth attribute (32 ms below the Top Temblor) from a volume flattened at the Top Temblor shows lithology variation. The zero bandwidth indicates uniform lithology. The slice shows two lobe like features (marked in green) which corresponds to high amplitude sands (looking from subsurface)

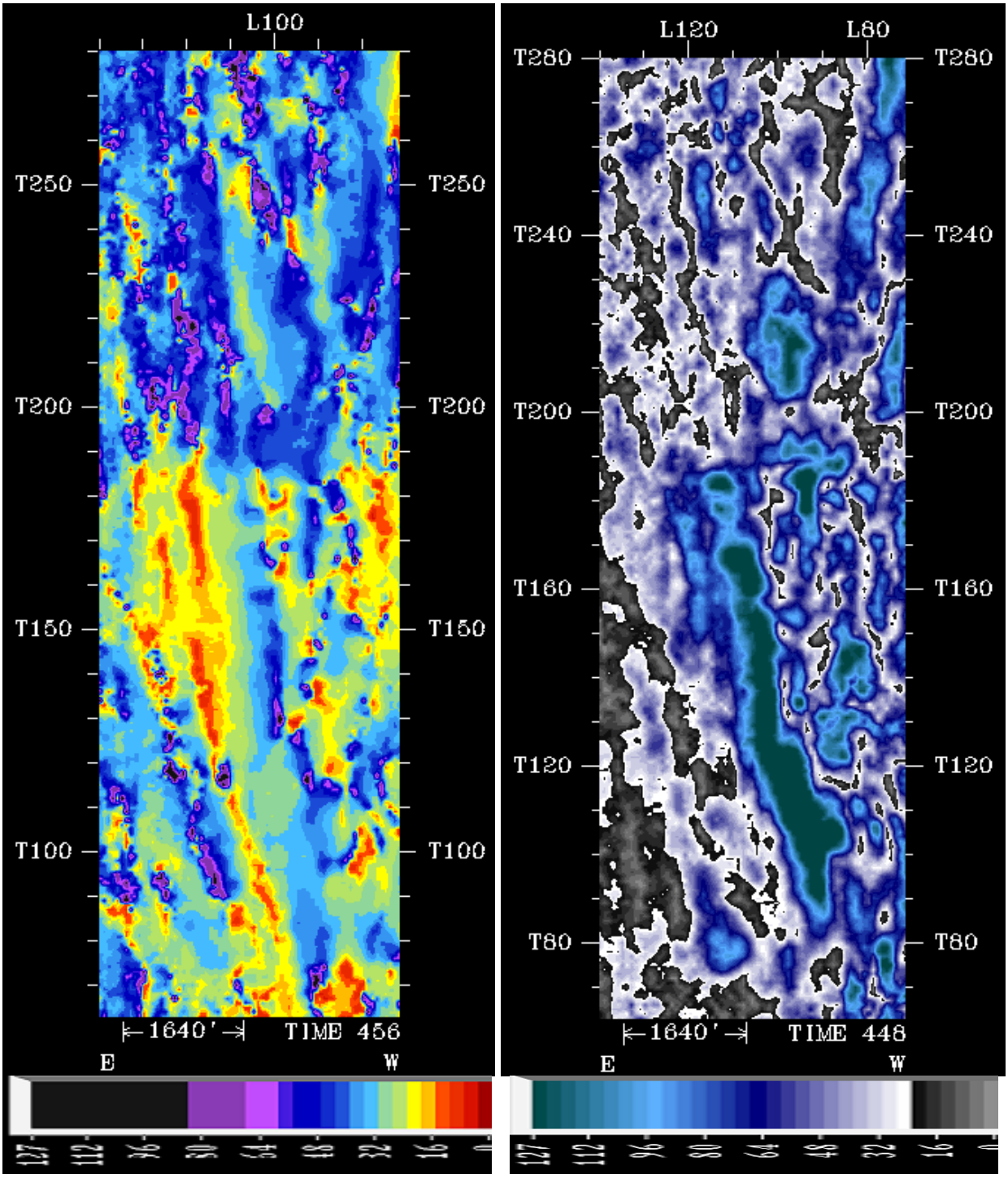

Instantaneous dominance frequency time slice (A)

Instantaneous amplitude time slice (B)

Figure 45. Showing a time slices of instantaneous dominant frequency (A). In right hand side, an instantaneous amplitude slice (B), 8 ms above of the instantaneous dominant frequency is shown for comparison. Low frequency shadows (red) are clearly seen corresponding to the high instantaneous amplitude values. The channel features move towards east (left side) with depth (looking from subsurface).

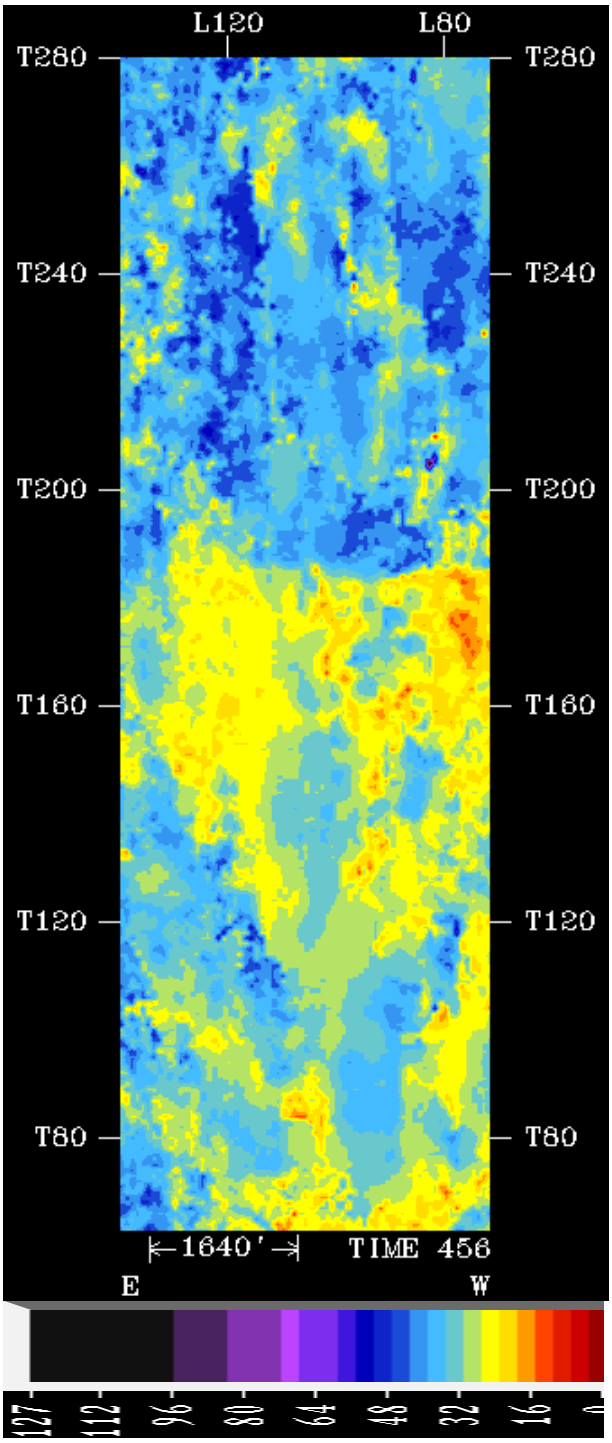

Response Frequency (A)

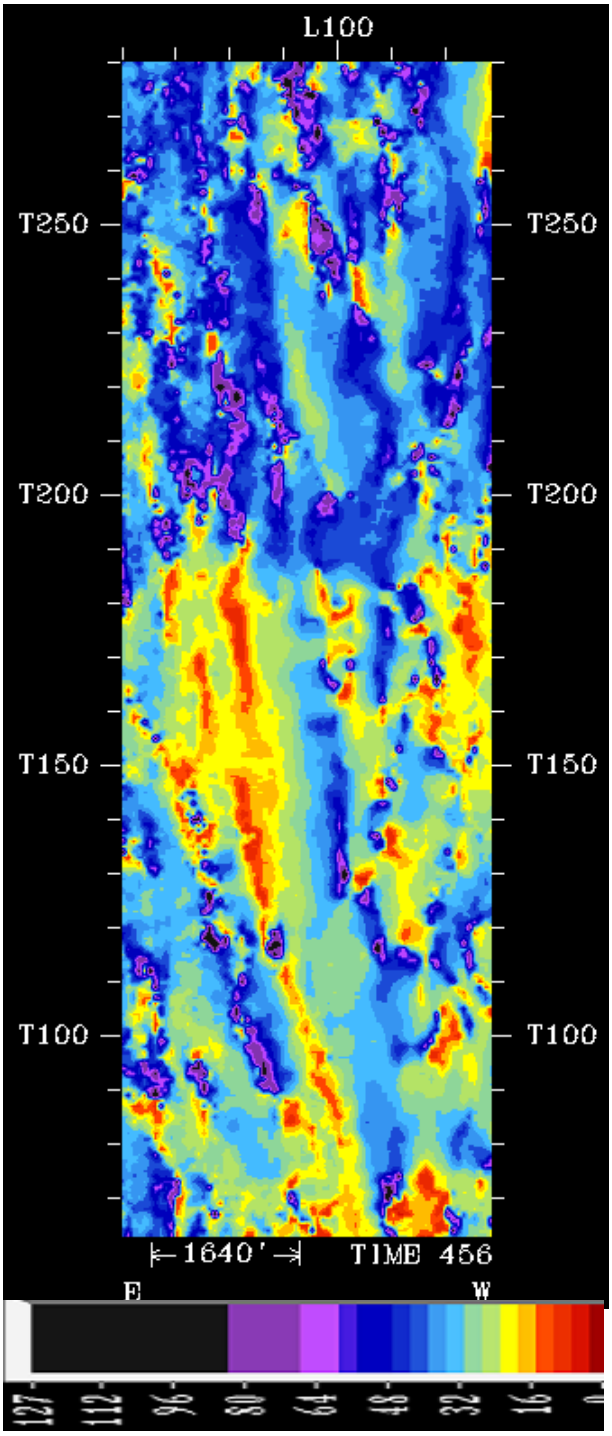

Instantaneous dominant Frequency (B)

Figure 46. Shows a time slice of response frequency (A). For comparison, a time slice of instantaneous dominant frequency (B) is shown. The lower frequencies of B (yellow) are broadly delineated in A (looking from subsurface).

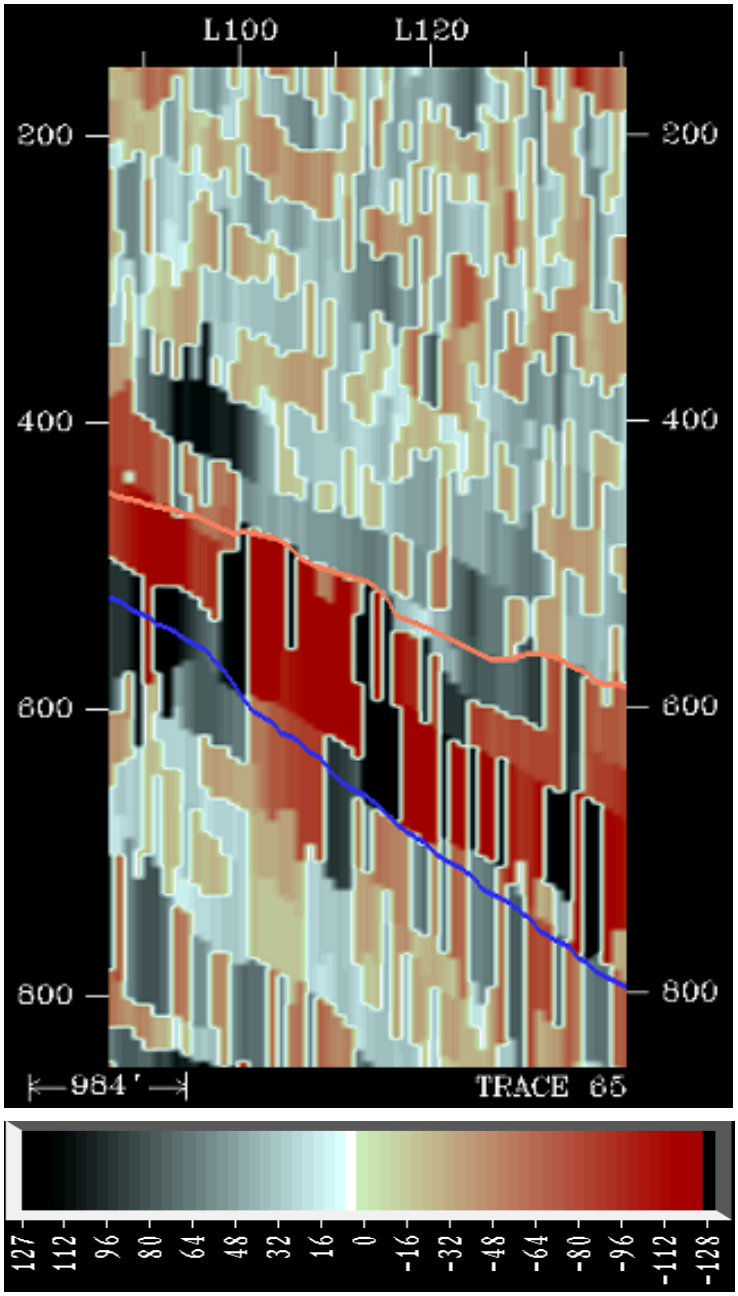

Figure 47. An apparent polarity strike section showing high polarity contrast in the Temblor Formation compared to that of both the underlying and overlying formation. The blue and orange boundaries are the Base Temblor and the Top Temblor.

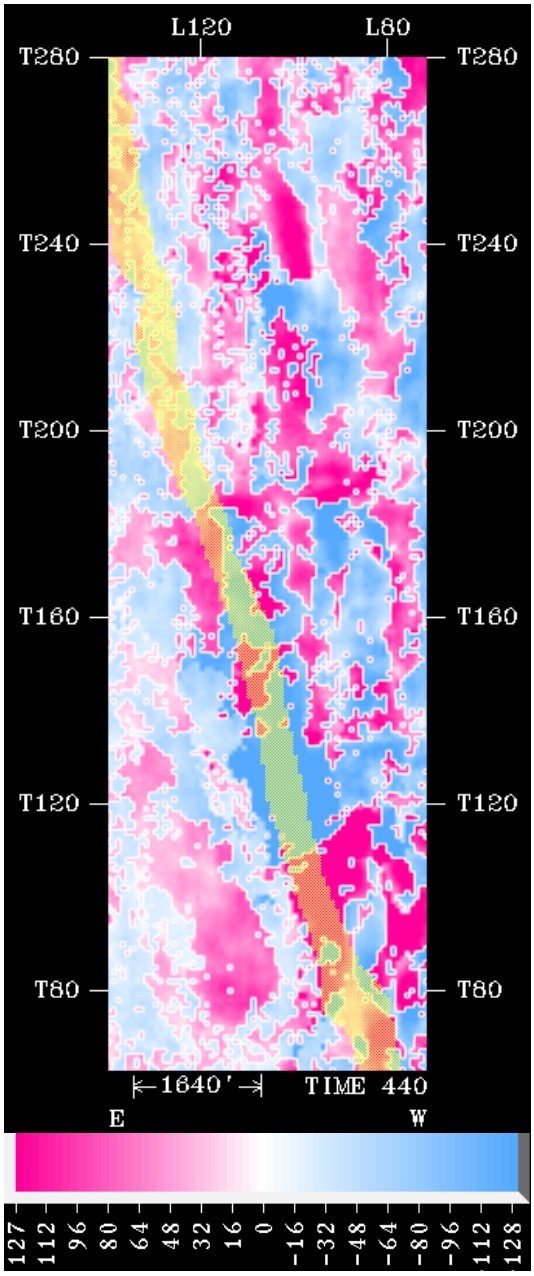

Figure 48. Time slice at 440 ms showing apparent polarity attribute contrast between the Temblor and Post Temblor Formations. The yellow zone across the slice represents the Top Temblor unconformity (looking upward from subsurface).

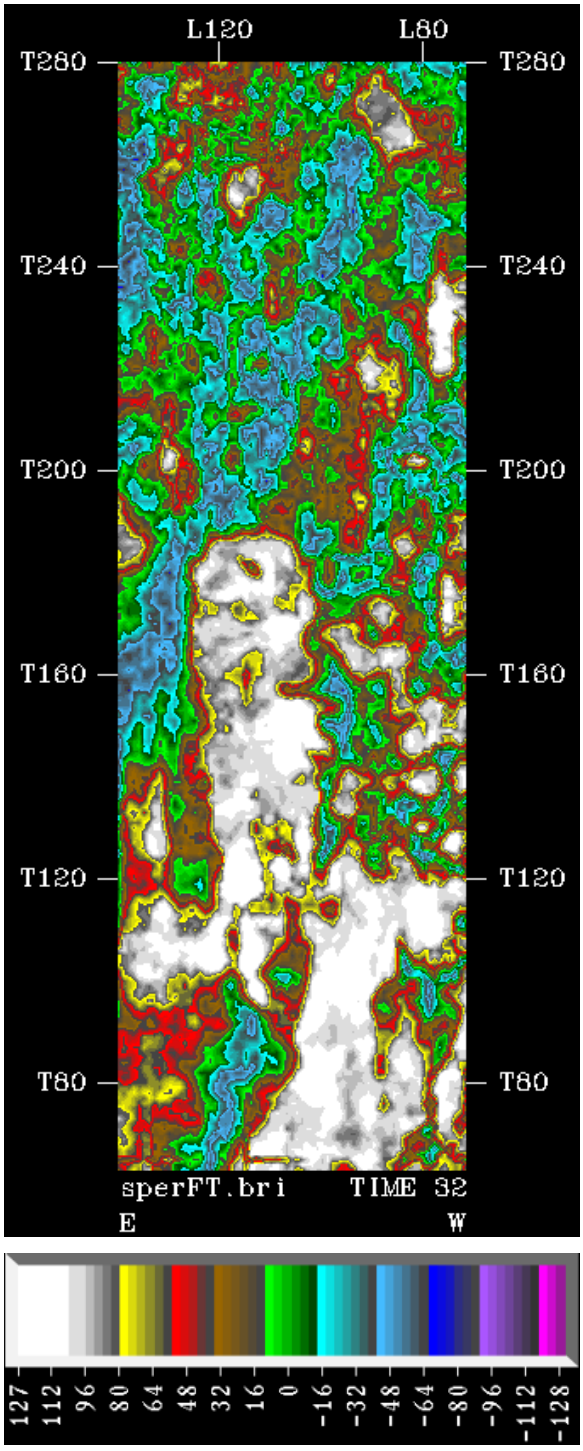

Figure 49. Shows time slice of perigram attribute at 32 ms of a volume flattened at the Top Temblor. High amplitudes (white) sinuous channel like features are observed which shift SE with depth (looking from subsurface).

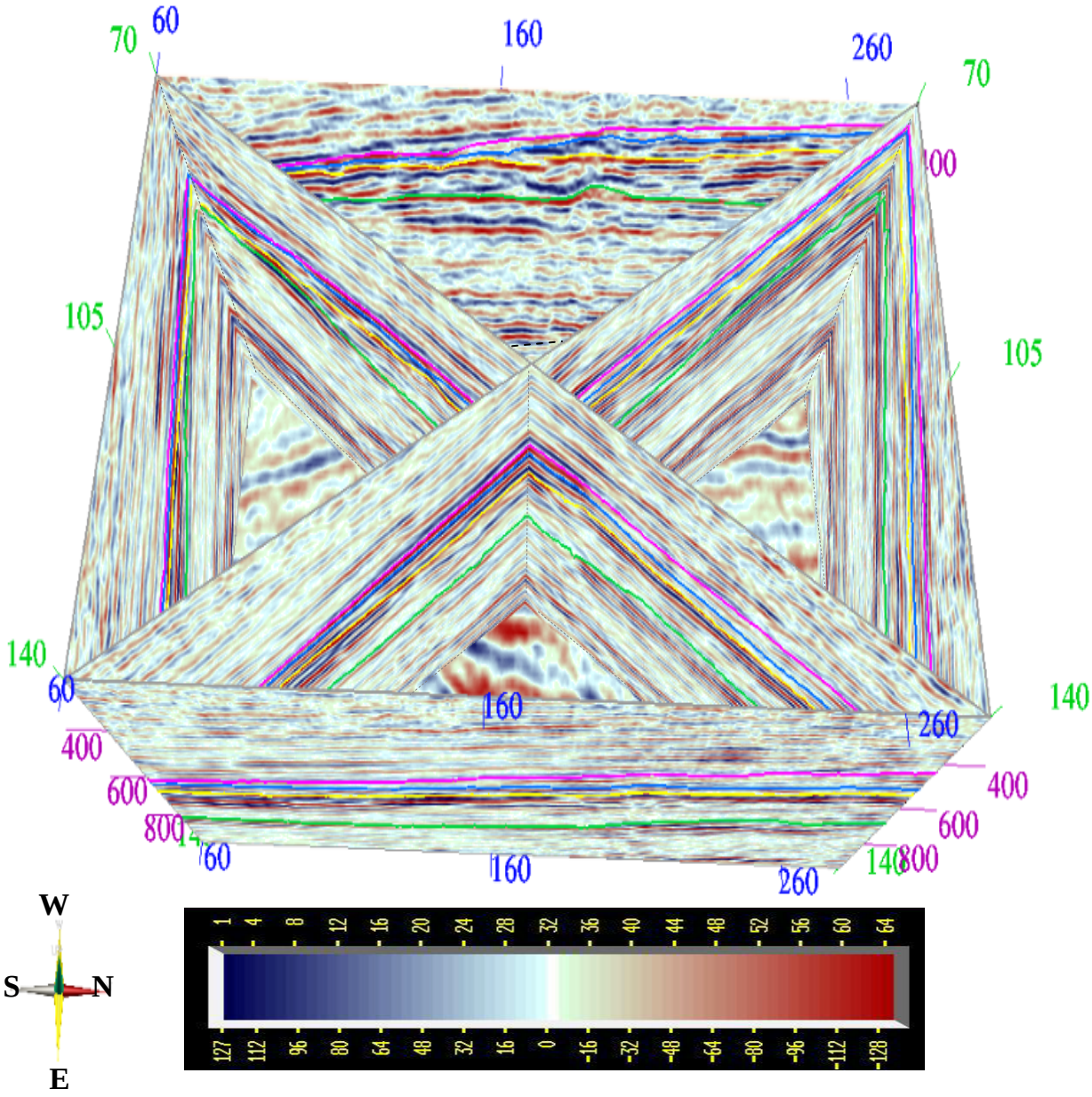

Figure 50. Seismic architectural display of Temblor Formation in colors showing the Base Temblor (green), Buttonbed (yellow), Valv (blue), and Top Temblor (pink) unconformities. The Temblor is shallowest to the NW and deepest towards the SE corner. Gradually the Temblor is at deeper level in the southern part than the northern part.

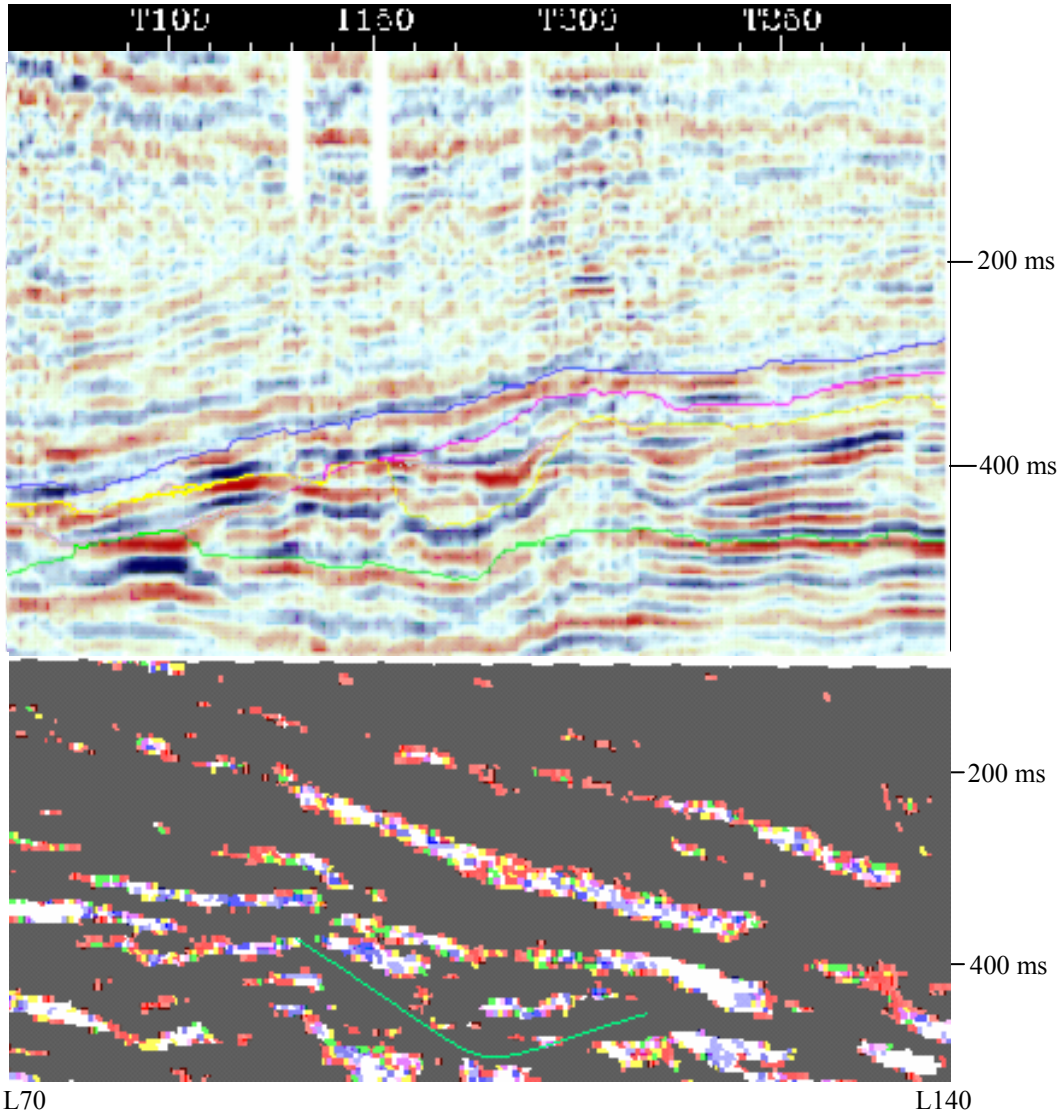

Figure 51. Channel features seen in inline 81. The bottom picture shows the same feature in voxel bodies in crossline 171. The presence of channel feature both in inline and crossline directions indicate its lateral and vertical extension over the study area.

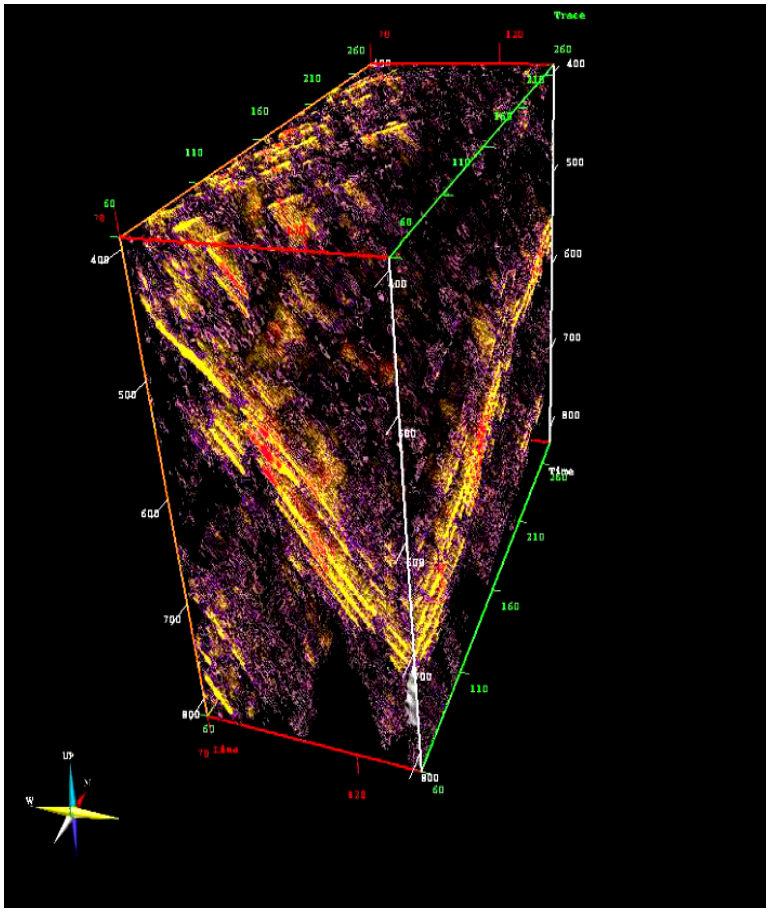

Figure 52. Cube of instantaneous amplitude showing stratification pattern underneath the study area (looking NNW). The strong amplitudes demarcate the Temblor Formation.

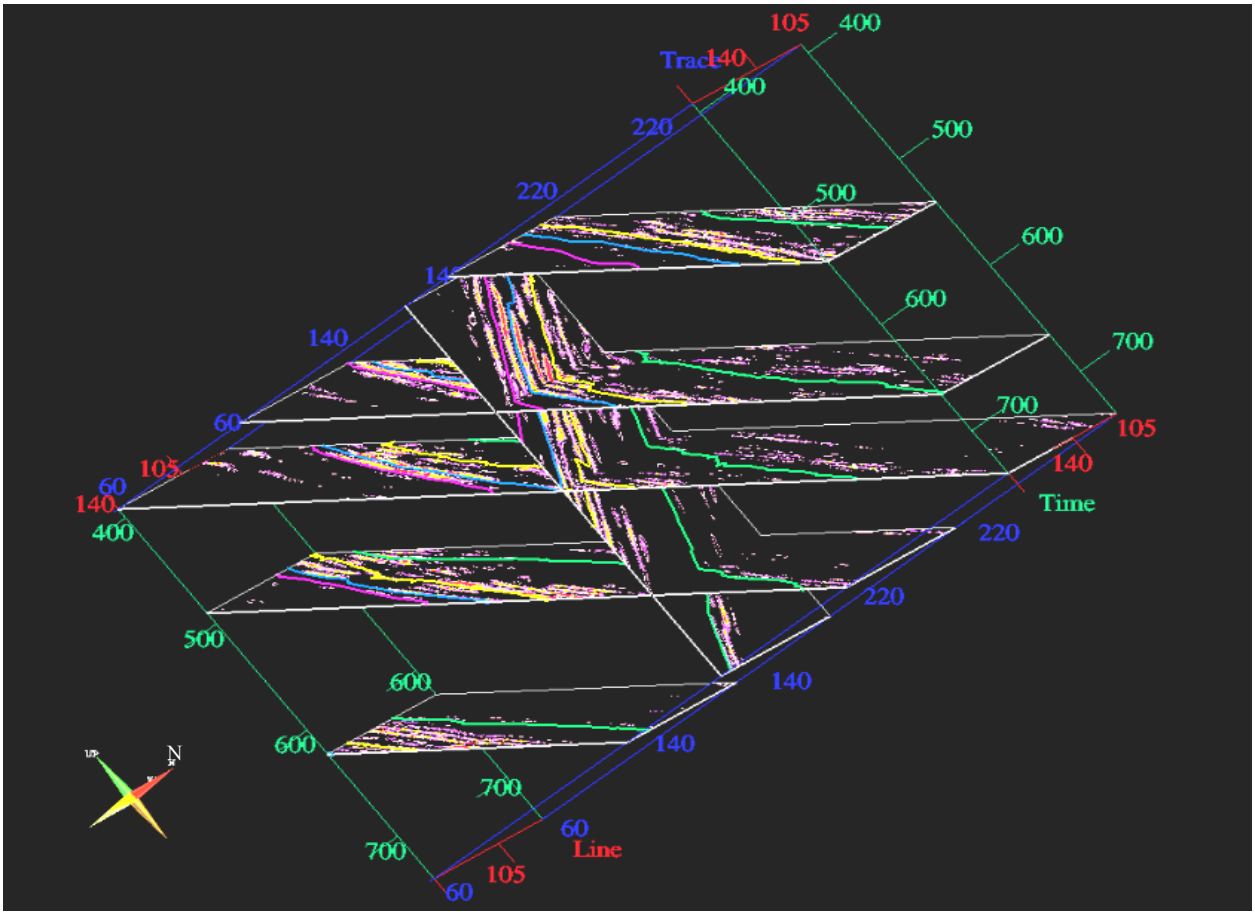

Figure 53. Time and oblique slices of instantaneous amplitude showing bed disposition along with Base Temblor (green), Buttonbed (yellow), Valv (blue), and Top Temblor unconformities in the Temblor reservoir (looking at NW).

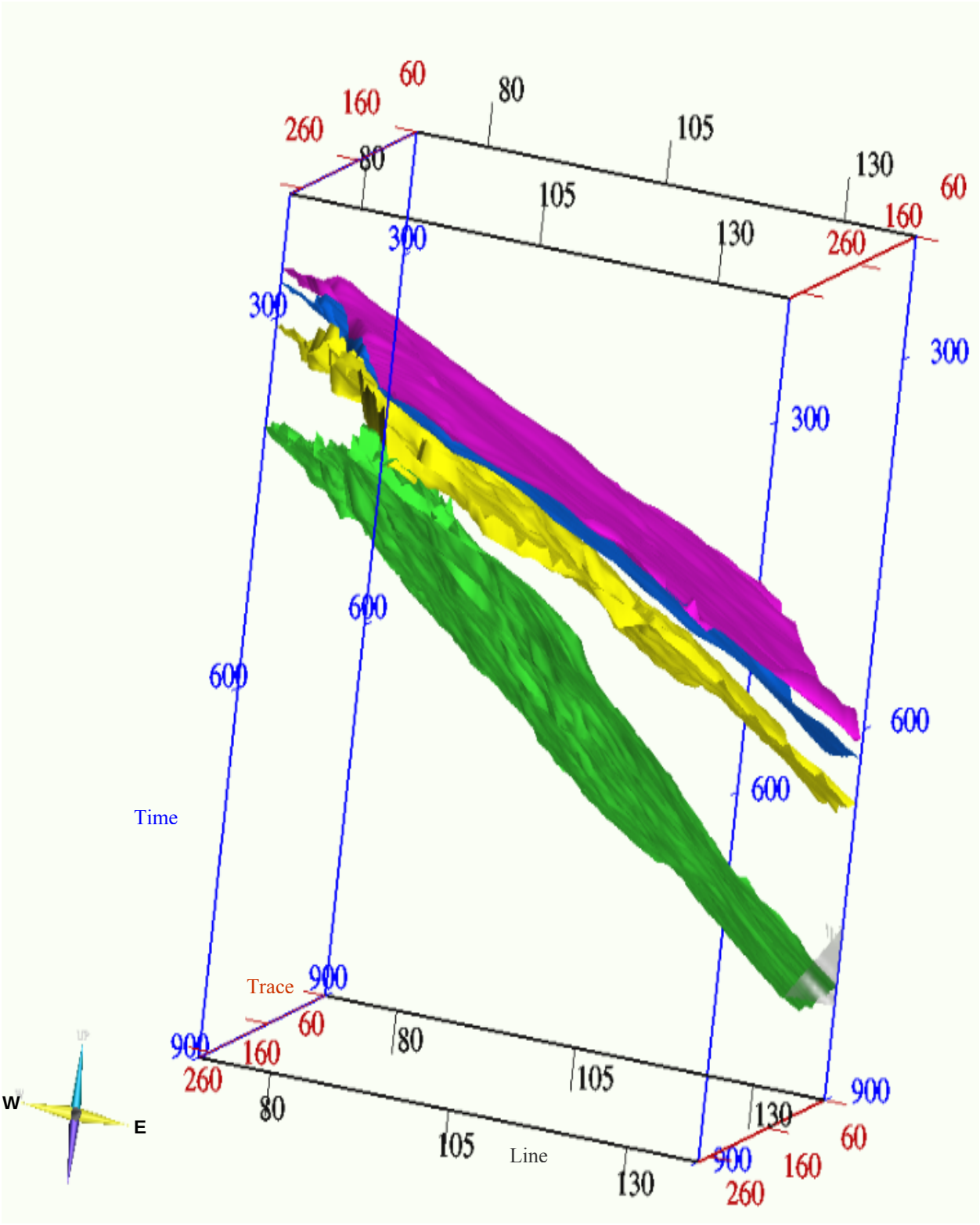

Figure 54. Shows the bounding surfaces of the Base Temblor (green), Buttonbed (yellow), Valv (blue), and Top Temblor (pink) in the Temblor Formation.

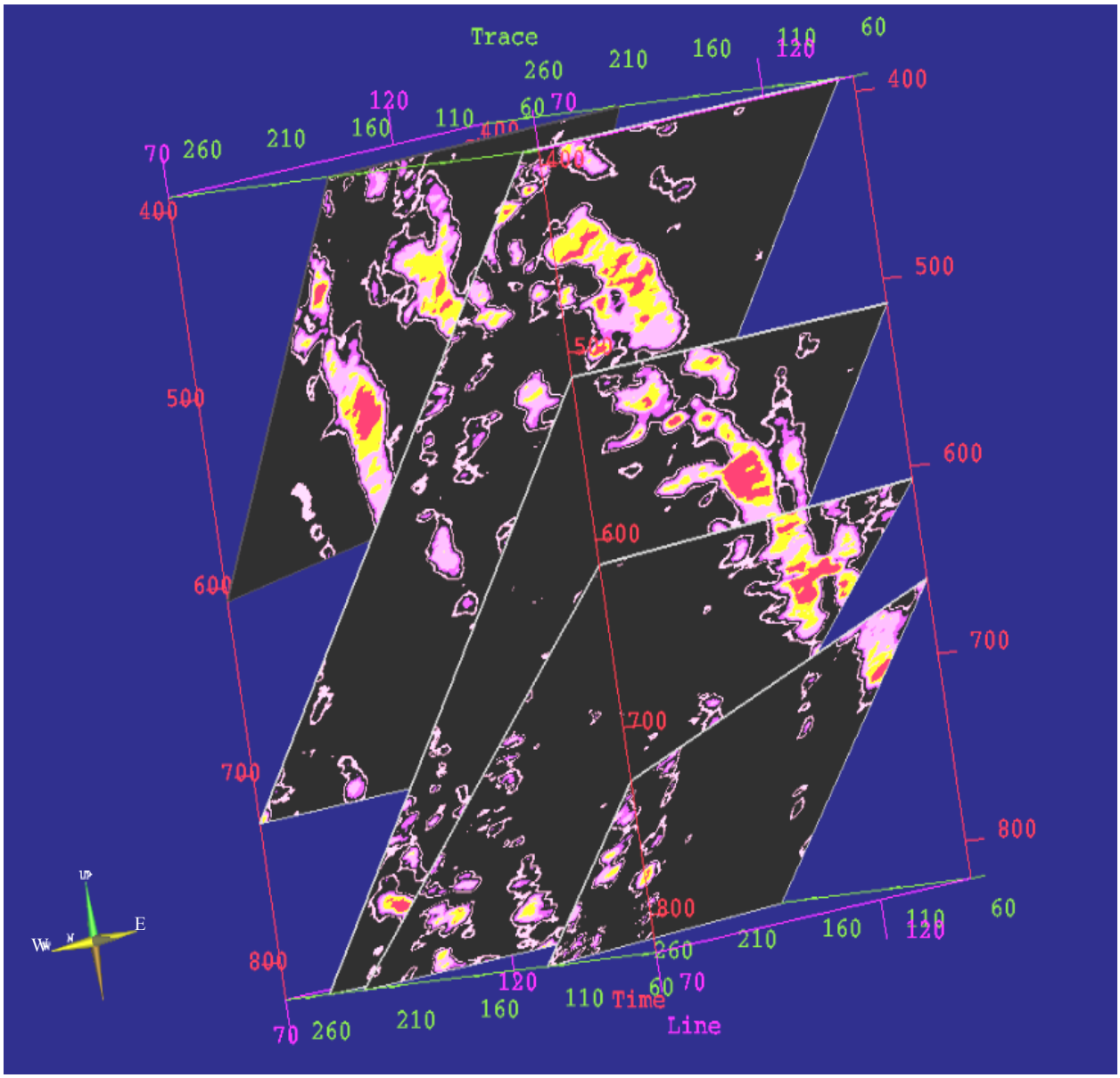

Figure 55. Oblique slices of instantaneous amplitude attribute. Note channel (yellow) course shifting towards ESE-SE. A second channel is shifting towards SSE (left, upper part). The high amplitudes (red) are probably hydrocarbon and/or steam.

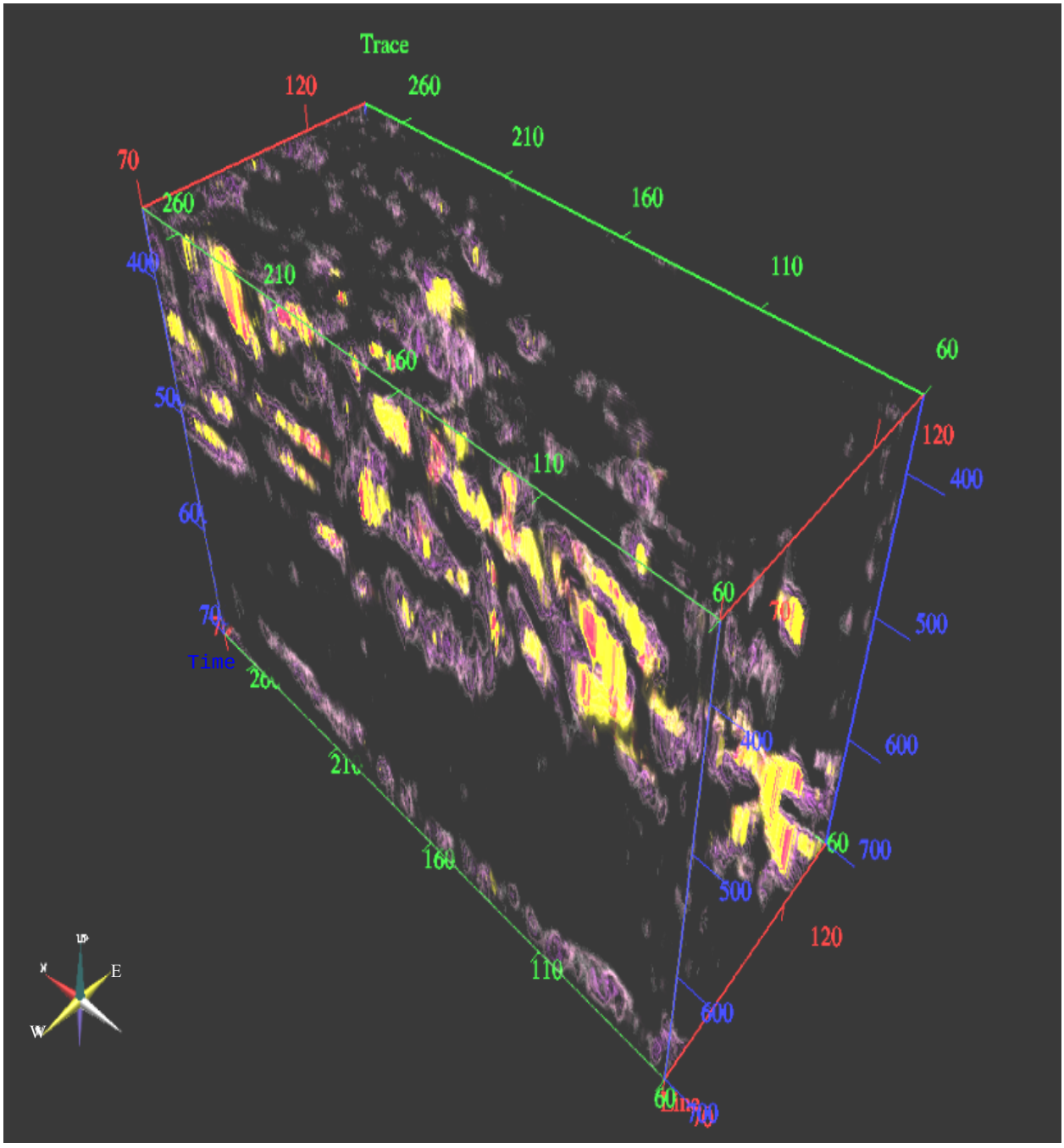

Figure 56. Cube of instantaneous amplitude attribute showing channel bodies (yellow) distribution in the Temblor reservoir. The high amplitudes (red) are probably hydrocarbon and/or steam.

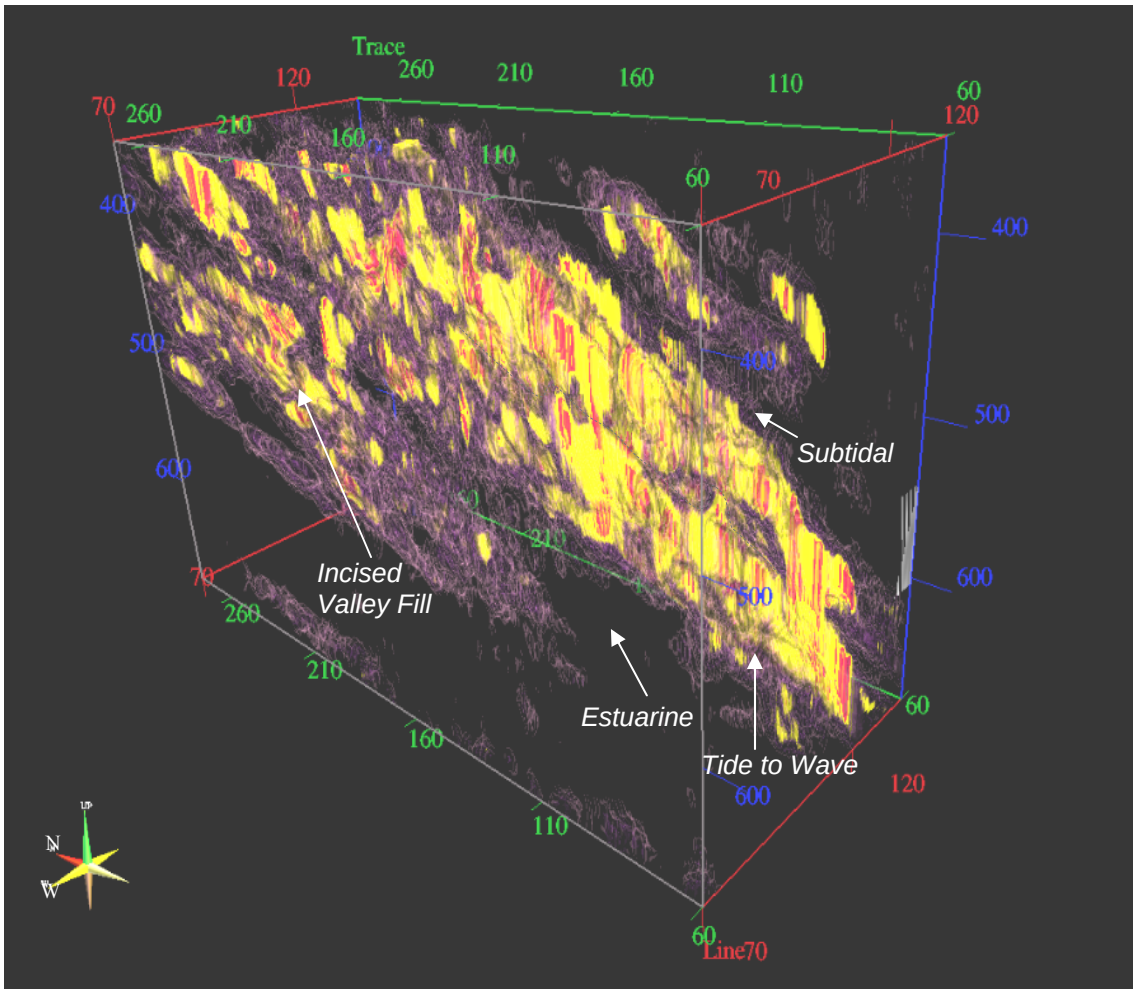

Figure 57. Instantaneous amplitude (reflection strength) attribute cube showing lithofacies distribution in various depositional settings. The high amplitudess (yellow) are likely sands as evidenced by the presence of the higher amplitudes (red) caused by probably hydrocarbon and/or steam. Note the absence of any prominent porous reservoir rocks between 550-650 ms (towards SW).

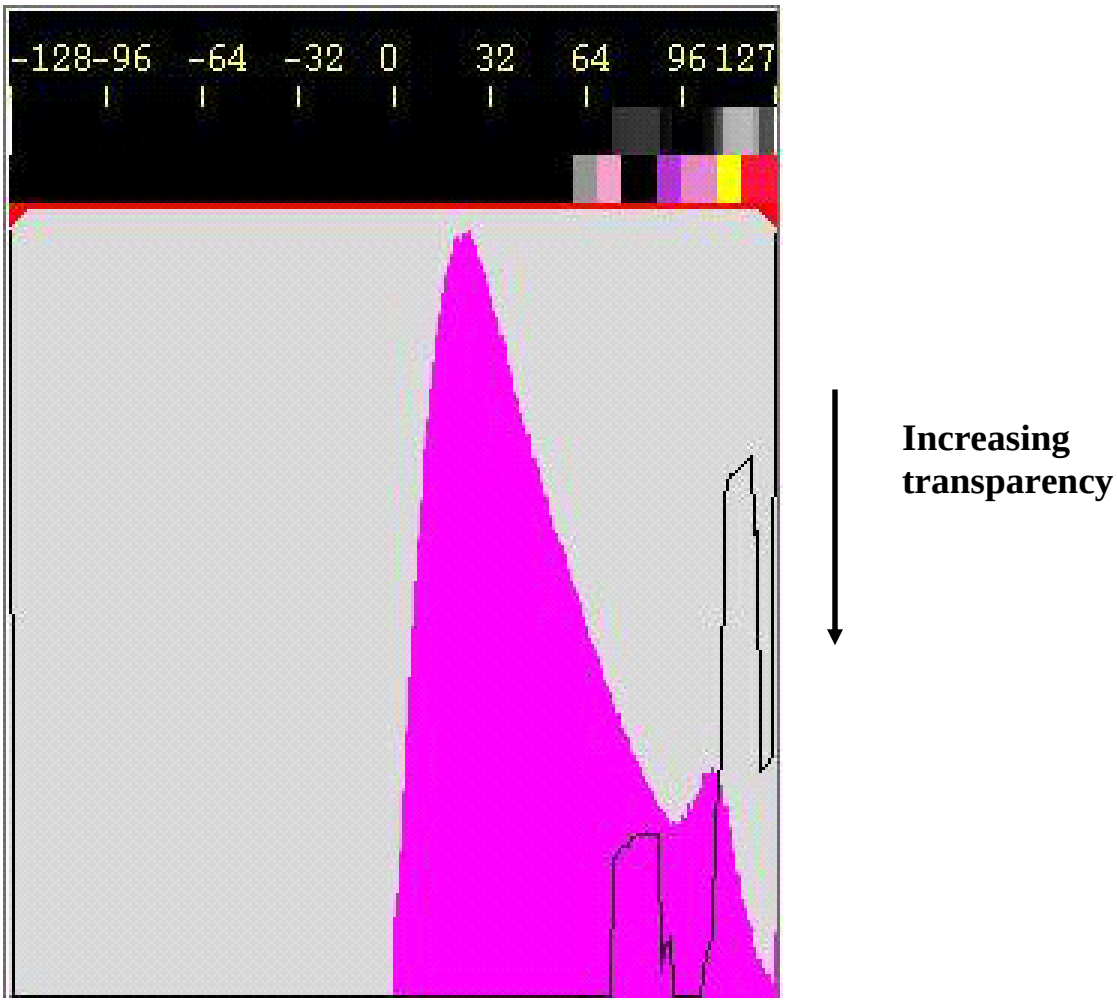

Figure 58. Opacity editor showing the histogram of the chosen instantaneous amplitudes (pink) and transparency level (curve in black inside the histogram) for different amplitude values (top of the figure) for obtaining the Figure 57).

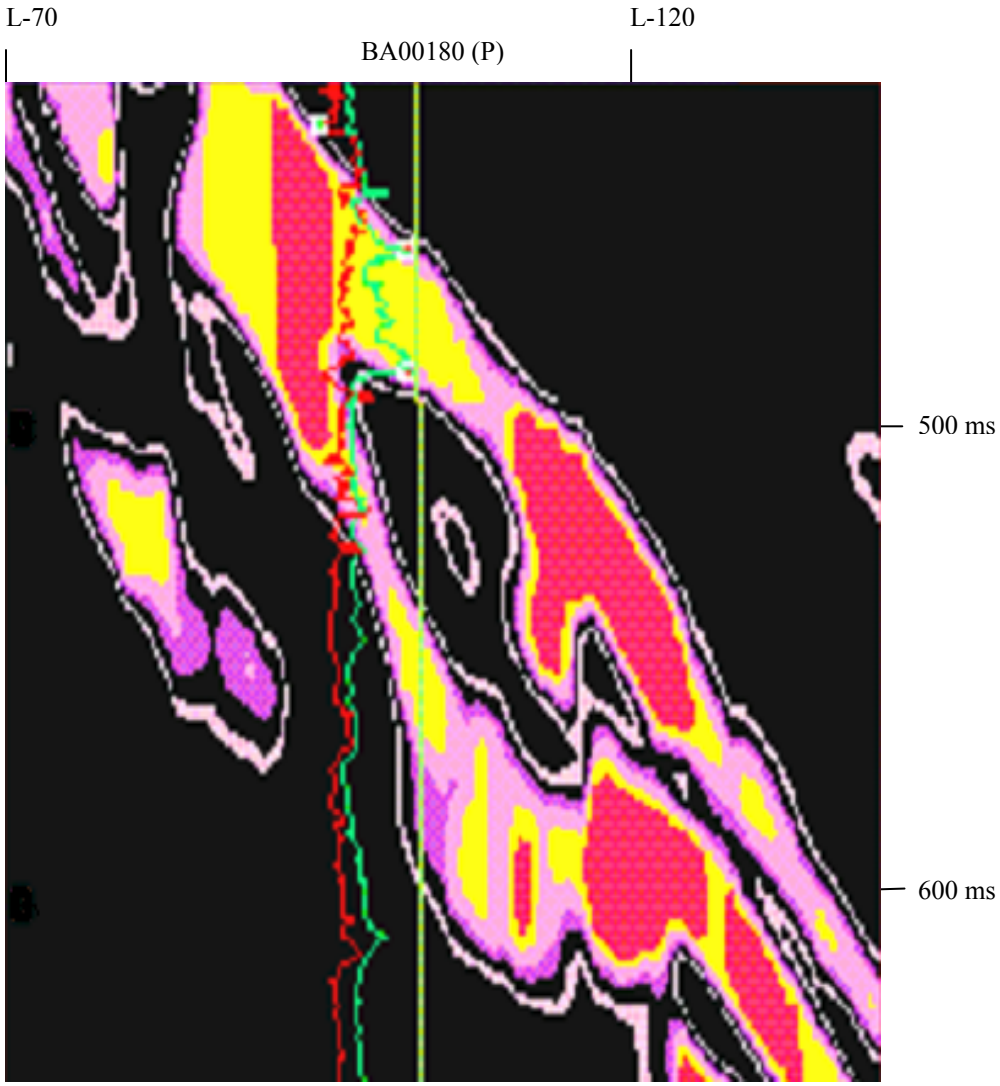

Figure 59. A vertical slice (T-104) taken from the instantaneous amplitude cube (generated for the Figure 55) shows wireline log GR (green) and CNL (red) values against the high instantaneous amplitude bodies (yellow). The log values increases from left to right. The well is offset by 500 feet. The high amplitudes collocate with a high gamma sand as interpreted in Figure 61.

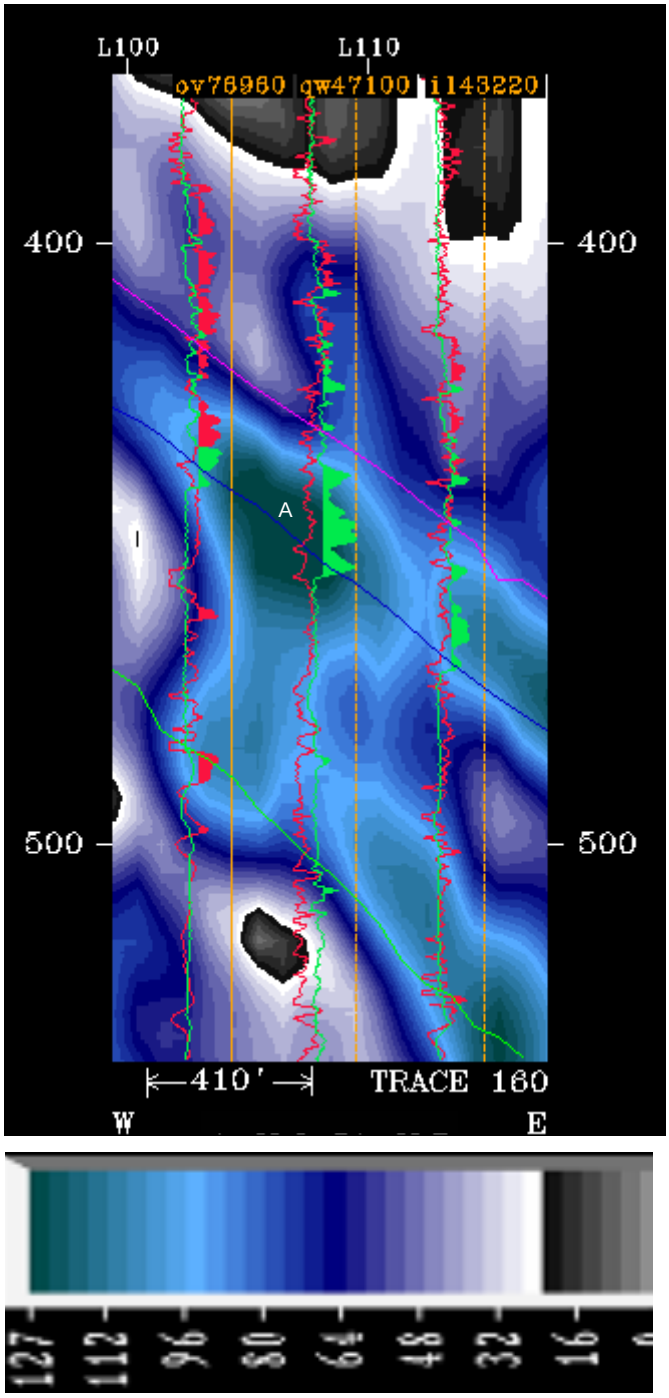

Figure 60. Trace section of instantaneous amplitude showing GR (green) and CNL porosity (red) wireline logs. The log values increase from left to right. Porous, upward coarsening stacked high-gamma sands (A) collocates the high amplitudes (as observed in Figure 61). The wells are projected (>180 feet). Time is in ms.

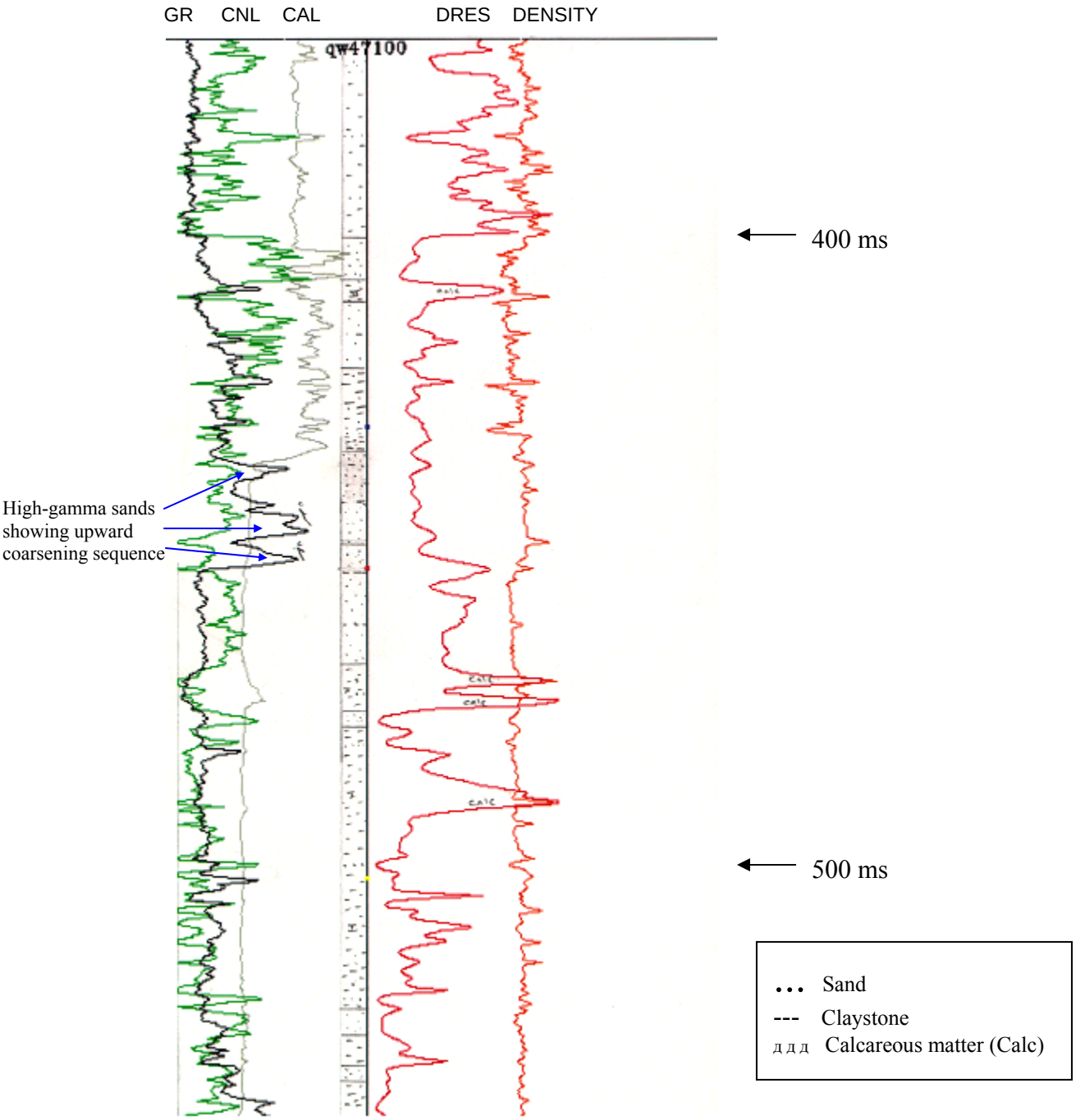

Figure 61. Showing wire line logs and interpreted lithology of well qw47100. The log Parameter values increase from left to right. Three upward coarsening stacked high-gamma sand sequences are observed.

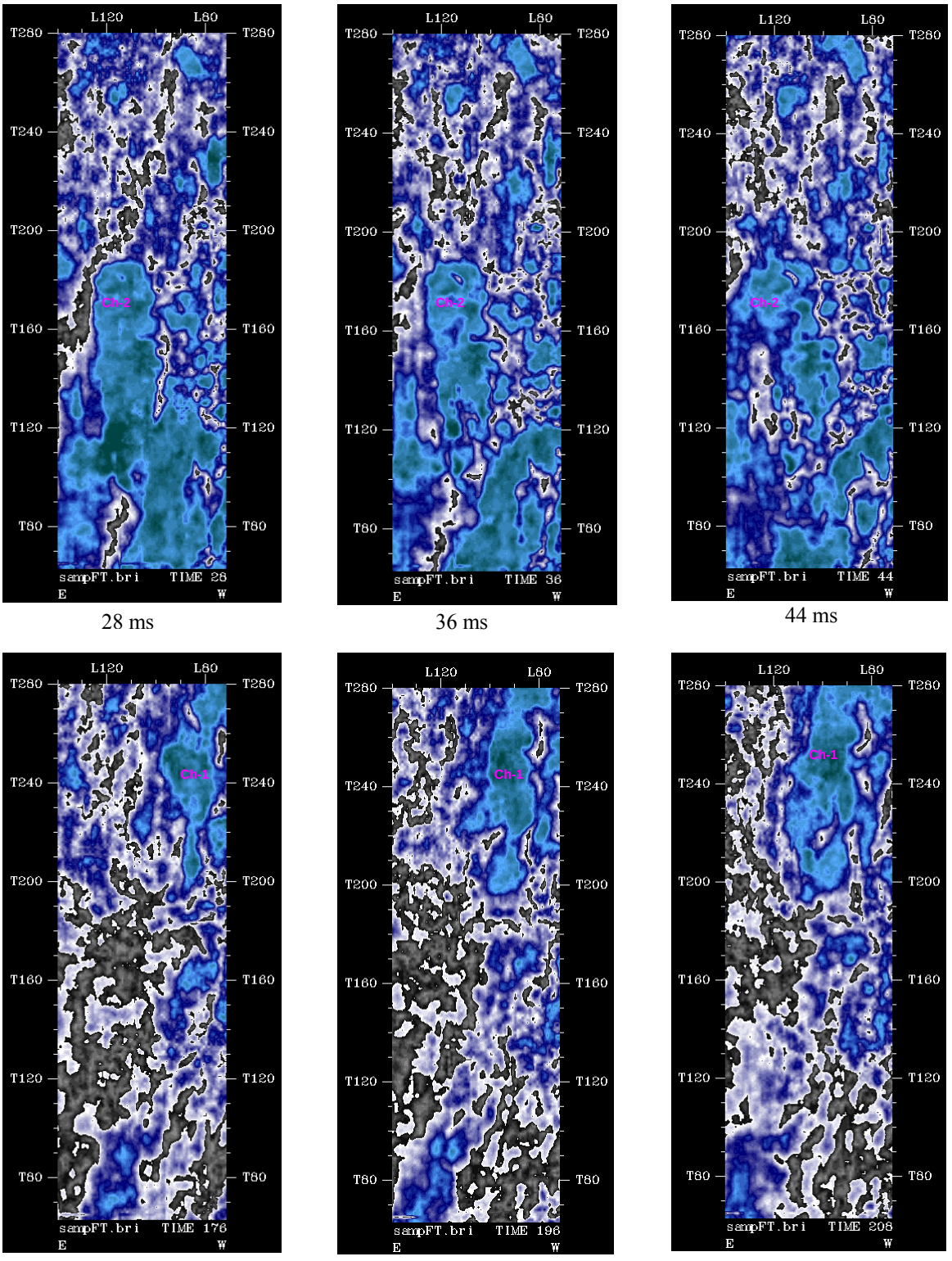

28 ms 36 ms 44 ms

176 ms 196 ms 208 ms

Figure 62. Time slices of instantaneous amplitude volume flattened at the Top Temblor (looking from subsurface). Two channel like sinuous features are observed as observed in other flattened and regular attributes.

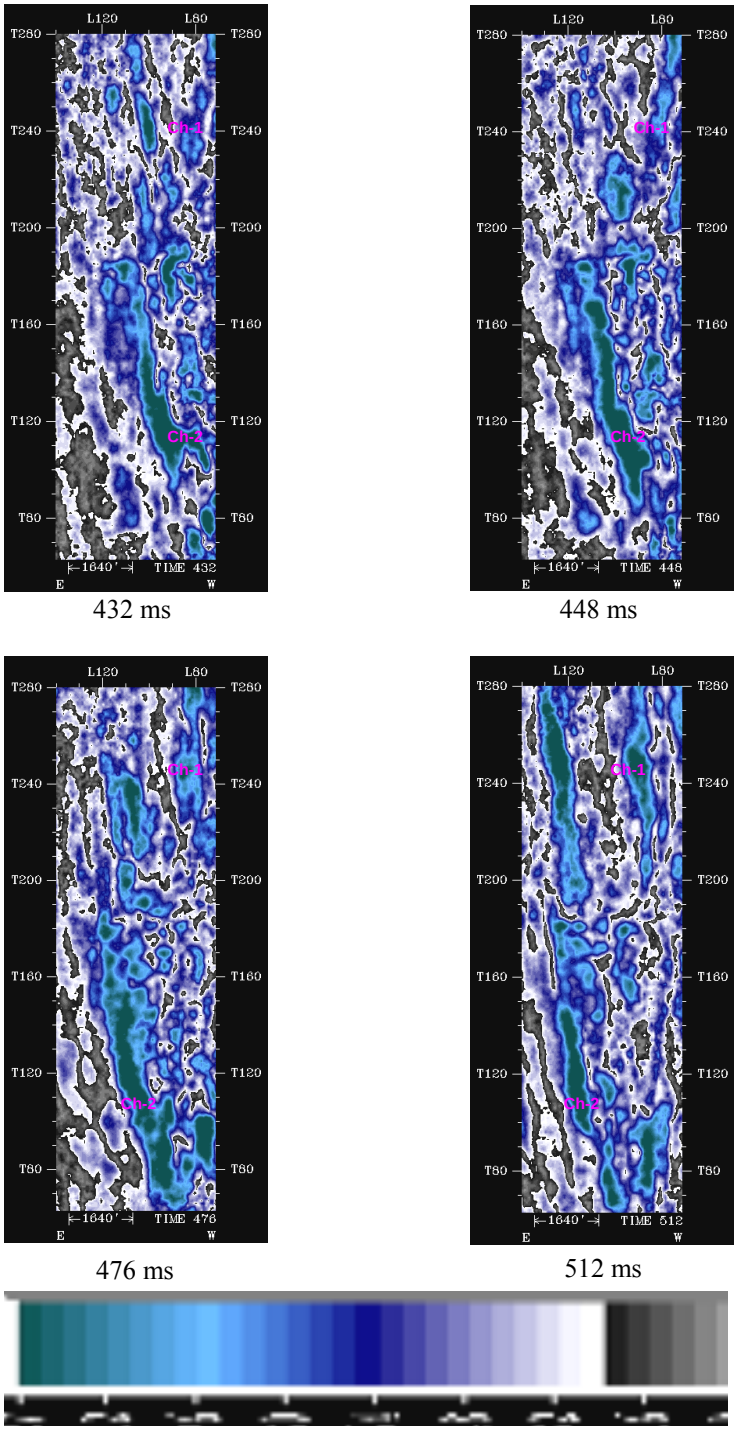

432 ms

448 ms

476 ms

512 ms

Figure 63. Time slices of instantaneous amplitude showing channel like sinuous features (looking from subsurface). The channel feature shifts eastward with depth. The left channel (Ch-2) is shallower and follows the Top Temblor in the southern part. The deeper one (Ch-1) on the right side follows the Base Temblor unconformity and discontinuous in the central part.

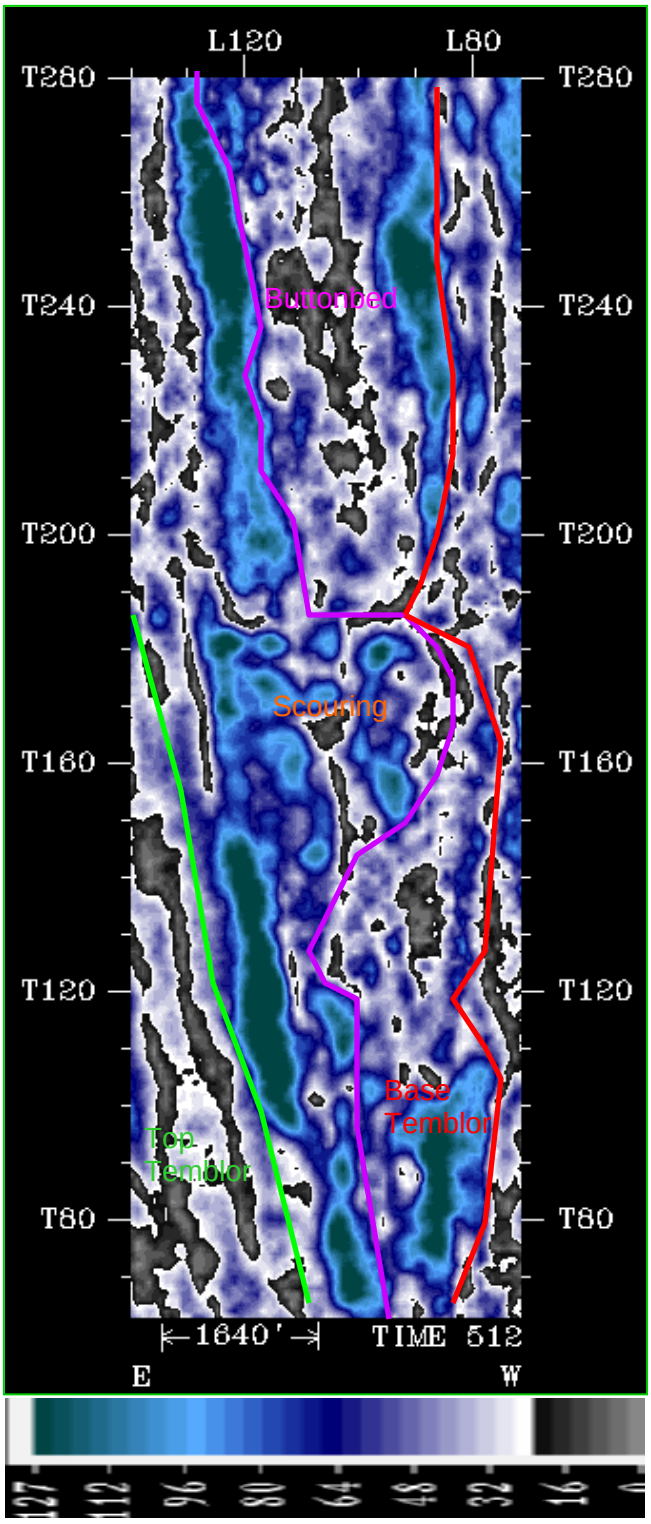

Figure 64. Time slice of instantaneous amplitude at 512 ms showing high amplitude (dark green) distribution and unconformities. Channel scouring feature is observed in the central part of the study area (looking from subsurface).

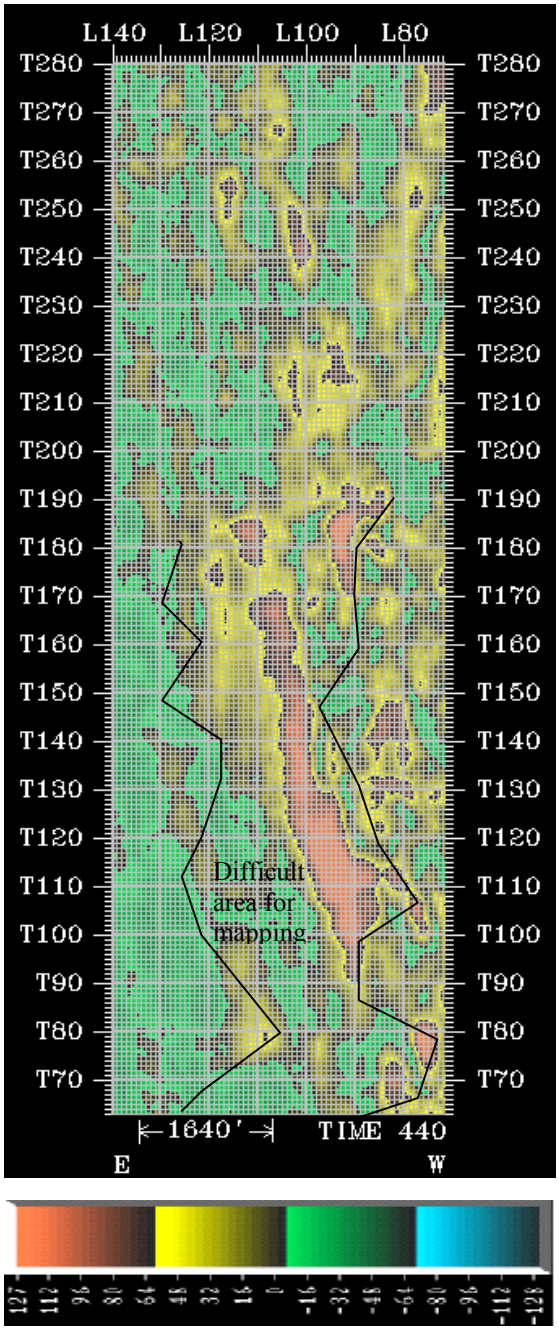

Figure 65. Overlay of seismic lines (L), traces (T), and a perigram time slice below the Top Temblor of the study area. The difficult area for mapping the reflectors in the southern part and for tying the reflectors between the northern and southern part may be due to the static and/or steam effect associated with the underlying high amplitudes (brown) sand bodies (looking from subsurface).

Tables

Facies tract	Thickness (m)	Lithology	Grain size	Sorting	Physical features	Biological features
Incised valley	0–50	Basal conglomerate fining upward to sandstone, siltstone, and claystone	Very fine to very coarse sand; minor pebbles, cobbles, silt, and clay	Very poor to good	Stacked upward-fining intervals; trough and planar cross-bedding; mud intraclasts	Macrofossils rare; rare to common vertical burrows (*Skolithos* and *Ophiomorpha*) in siltstone and claystone
Estuarine	15–21	Interlaminated to interbedded sandstone, siltstone, and claystone	Very fine to medium sand; minor pebbles, silt, and clay	Moderate	Bi-directional cross-bedding; ripple cross lamination; clay drapes and sand-mud couplets on foresets; mud intraclasts; rare glauconite	*Ostrea* (oyster) fragments; common diatoms and foraminifers in siltstone; minor *Teichichnus* and common *Glossifungites* in claystone; minor wood and lignite
Tide- to wave-dominated shoreline	27–50	Cross-bedded sandstone, bioturbated sandstone, and claystone; minor siltstone, fossiliferous sandstone, and limestone	Very fine to coarse sand with minor pebbles, silt, and clay	Poor to moderate	Planar and trough cross-bedding; bi-directional cross-bedding; clay drapes and sand–mud couplets on foresets; mud intraclasts; minor shell-lag beds; rare glauconite	Minor to common shells of *Turritella*, *Cancellaria*, *Vaquerosella merriami* (sand dollar), *Aequipecten*, *Dosinia*, *Balanus gregarius* (barnacle); horizontal and vertical burrows of *Teichichnus*, *Macaronichnus*, *Diplocraterion*, *Ophiomorpha*
Diatomite	2.7–9.3	Variable proportions of claystone, siltstone, and sandstone; commonly cemented by carbonate	Predominantly fine sand, silt, and clay	Good	Thin to massive bedding	Variable content of diatoms, radiolarians, and foraminifers; rare *Quinqueloculina* sp. (foraminifer); common *Teichichnus* and *Terribellina* burrows in claystone
Subtidal	0–40	Massive bioturbated sandstone; thin intervals of siltstone and claystone	Fine to coarse sand, silt, and clay with dispersed granules and pebbles	Poor to moderate	Faint low-angle and planar cross-bedding; mottled bedding	Rare shell debris, including gastropods, sand dollars, and *Pecten*; minor *Skolithos* burrows

Table 1. Characteristics of facies tracts in the Temblor Formation.

(after Bridges and Castle, 2003)

Water-saturated SST at 30 MPa:
Vp=3.14 km/s, Vs=1.66 km/s
Ø=.36, density=2.23 gm/cm^3,

Fluid Substitution with respect to water-saturated SST at 5 MPa

	Vp (Km/s)	Density (gm/cm^3)
Sand+Water	2.52	2.08
Sand+Oil	1.955	2.03
Sand+Gas	1.428	1.71
Sand+Steam	1.426	1.72
Clay	3.41	2.6

Bottom Layer ↓ / Top Layer →	Sand + Water	Sand + Oil	Sand + Gas	Sand + Steam	Clay
Sand+Water	0	0.14	0.36	0.36	-0.26
Sand+Oil	-0.14	0	0.24	0.24	-0.38
Sand+Gas	-0.36	-0.24	0	0	-0.57
Sand+Steam	-0.36	-0.24	0	0	-0.57
Clay	0.26	0.38	0.57	0.57	0

Comments:

1. The maximum Vp, Vs, Ø, and density values for poorly unconsolidated water-saturated sandstones at 30 MPa effective pressure (top left corner of the table) were considered (Mavko, et al., 1998, page no. 302).

2. The density, bulk modulus, and shear modulus for the frameworks silicates (quartz) considered were from Carmichael (1989) as cited by Mavko, et al. (1998), page no. 307. For clay, the values were for "Gulf clays" Tosaya (Mavko, et al., 1998, page no. 307).

3. The bulk modulus, density, and Vp value for water, oil, gas, and steam were calculated for the actual reservoir pressure and temperature conditions (5 MPa, 30^0 C) following the algorithms given by Mavko, et al. (1998), page nos. 215-218. For steam, reservoir temperature of 110^0 C was considered. The densities of gas, oil, and brine water at surface temperature (15.6^0 C) and atmospheric pressure were taken as 0.56, 0.934 (20^0 API), 1.07 respectively. In case of steam, a surface density of 0.95805 (at ~100^0 C) was considered.

4. The Vp for the oil-, gas-, and steam-saturated unconsolidated sandstones were computed by Gassmann's fluid substitution (Mavko, et al., 1998; Gassmann, 1951) considering the derived parameters of water-saturated unconsolidated sandstones as the initial values.

Table 2. Reflection coefficients for different siliciclastic lithologies mixtures computed from the theoretical and derived modulus, velocity, and density values. The porosity and gravity values are similar to that of the Temblor reservoir rocks in the Coalinga field (refer to comments in table for computational methodology and data source).

Vita

Sailendra Nath Mahapatra was born in Puri, Orissa, India. He spent his childhood with parents at village: Godipada, PO: Jankia, District: Khurda, Orissa, India where his father has farming lands. He is the eighth child of his parents and is survived by three brothers and five sisters.

He obtained his Master of Science degree in Applied Geology and Master of Technology degree in Mineral Exploration from Indian School of Mines, Dhanbad, India.

Prior to pursuing the present Ph.D. program in Geophysics at Virginia Tech, he worked in the upstream oil industry as a geologist for 20 years.